

TEMPERATURE ANOMALIES IN TRANSITION-METAL-OXIDES AND THEIR CORRELATIONS WITH PHOTOCATALYTIC ACTIVITY

STRUCTURAL, DIELECTRIC AND ELECTRICAL CHARACTERISATION OF
TITANIA SYSTEMS

DISSERTATION

ZUR

ERLANGUNG DES AKADEMISCHEN GRADES

DOCTOR RERUM NATURALIUM (DR.RER.NAT.)

DER MATHEMATISCH-NATURWISSENSCHAFTLICHEN FAKULTÄT

DER UNIVERSITÄT ROSTOCK

VORGELEGT VON:

MARTIN HANTUSCH GEB. AM 14.04.1990 IN GROSSRÖHRSDORF

AUS BISCHOFSWERDA

ROSTOCK; DECEMBER 15, 2017

https://doi.org/10.18453/rosdok_id00002487

MATHEMATISCH-NATURWISSENSCHAFTLICHE FAKULTÄT

INSTITUT FÜR PHYSIK

1st reviewer: Prof. Dr. Eberhard Burkel, Universität Rostock, Germany

2nd reviewer: Prof. Dr. Valentin Bessergenev, Universidade do Algarve, Portugal

Date of application: December 19, 2017

Date of colloquium: April 06, 2018

dedicated to my beloved brother

Torsten

1982-2015

Abstract

The correlation between the defect structure, the crystalline structure and the charge carrier transfer through titanium dioxide (titania) were evaluated by in-situ X-ray diffraction, in-situ resistivity characterisation, quasi-in-situ X-ray photoelectron spectroscopy and paramagnetic resonance spectroscopy in order to improve the photocatalytic efficiency of a newly invented water purification reactor.

Annealing titanium dioxide in vacuum at temperatures below the phase transition temperature while an external electrical field was applied resulted in the observation of structural, morphological and electrical anomalies. These anomalies occur in thin films, as well as, in powder samples. However, treating titanium dioxide in vacuum leads to a redistribution of lattice defects. The diffusion of these lattice defects from the centre of the lattice to the line defect area forms charge carrier trapping sites and permanent dipoles with a significant dipole strength. The alignment of these dipoles leads to the formation of anisotropic conductive channels.

The activation of a resistive switching mechanism is possible since these conductive channels can be open or closed depending on the external electrical field strength. Hence, a quasi-para-electric material is synthesised.

Furthermore, the redistribution of lattice defects driven by an external electrical field results in a new density distribution and the formation of a new highly textured crystalline phase, the arminiase, which is correlated with the conductive configuration of titanium dioxide.

Contents

1	Motivation	1
2	TiO₂ - Basic principles and problems	5
2.1	Defect physics	5
2.1.1	Point defects	7
2.1.2	Charge trapping	9
2.1.3	Surface changing processes	10
2.2	Crystal structure	11
2.2.1	Anatase	11
2.2.2	Rutile	12
2.2.3	Phase transition	12
2.3	Photocatalysis	14
2.3.1	Synergetic effect	16
3	Methods	17
3.1	Characterisation	17
3.1.1	X-Ray-Diffraction	17
3.1.2	Surface area and porosity	21
3.1.3	Chemical composition	24
3.1.4	Resistivity	28
3.1.5	Photocatalytic activity	30
3.2	Synthesis and sample preparation	32
3.2.1	Powder samples	32
3.2.2	Thin film samples	34
4	Results	37
4.1	Photocatalytic activity	37
4.2	Surface Area and Porosity	39
4.3	X-ray Photoelectron Spectroscopy	46
4.3.1	Chemical composition	46
4.3.2	Surface defect analysis	47
4.4	EDX - Chemical composition	50

4.5	Resistivity	52
4.5.1	P25 - powder	52
4.5.2	Sol-gel-based-powder	54
4.5.3	Thin films	55
4.5.4	Barrier energy of the charge carrier traps	57
4.6	Defect analysis - EPR	60
4.7	Structural analysis - XRD	64
4.7.1	In-situ-measurements	64
4.7.2	Pseudo titanium dioxide phase - Arminiase	68
5	Discussion	75
5.1	Surface area and the photocatalytic activity	75
5.2	Charge carrier transfer analysis	77
5.3	Quasi-para-electric TiO ₂ and its crystal structure	81
5.4	Defect structure and crystal structure	90
6	Conclusion	93
	Appendix A Resistivity	97
	Appendix B Structure	99
	Appendix C EPR	101
	Bibliography	103
	List of Figures	119
	List of Tables	126

Chapter 1

Motivation

In recent years, the development of applications based on renewable energies and new energy storage applications is of an high importance. The change from fossil energy sources to CO₂-neutral energy sources is propelled by political and economical interests. Furthermore, applications based on renewable energies provide the opportunity to cover basic requirements such as power, heat or clean water in underdeveloped areas [1–6].

Nevertheless, there are many possibilities to improve the state of the art applications, especially, with respect to their (cost) efficiencies. This causes a need of fundamental research on new materials which should have enhanced efficiencies, low production costs and easy availabilities. One possibility is to use transition-metal-oxides, e.g. nickel oxide, iron oxides or titanium dioxide. For example, nickel oxide is commercially used as solid state membrane in new fuel cells [7, 8] despite the process of the charge carrier transfer through the material is not understood in detail, yet. This means that fundamental research could provide a significant enhancement for important future applications of mobility.

Additionally, transition-metal-oxides in perovskite structure, e.g. calcium titanite, strontium titanite or calcium manganite are crucial materials for future photovoltaic or even medical applications [9–13]. These materials are studied with respect to their electrical and dielectric properties, especially, when they are highly defective. The influence of structural defects can cause a dielectric behaviour which is not typical for these materials. For example, defective calcium titanite shows quasi-piezoelectric behaviour [14]. These cases show the wide range of usage possibilities of transition metal oxides.

In this work, the focus will be on titanium dioxide. This transition-metal-oxide is known for its high photocatalytic activity which allows the use of titanium dioxide in water cleaning processes, as well as, for hydrogen production [15–19]. There are many scientific publications about titanium dioxide and the enhancement of its photocatalytic efficiency which is based on three parameters: the band gap energy of titanium

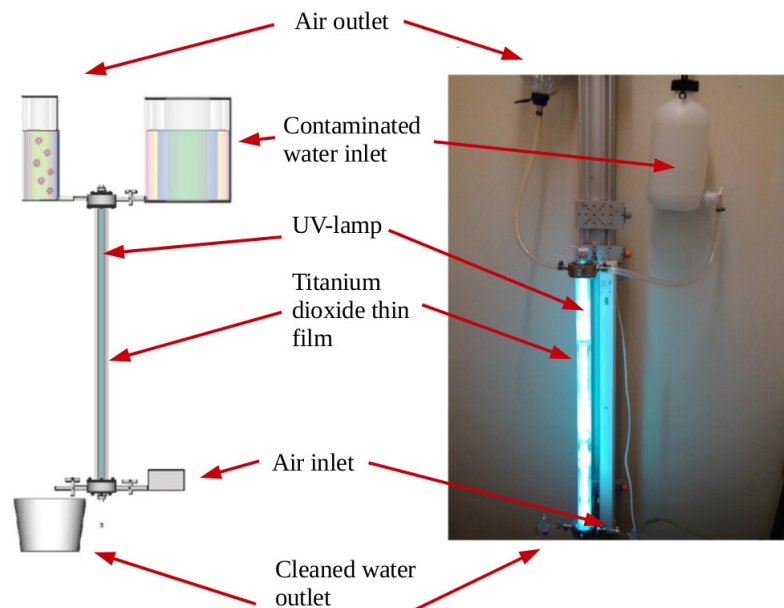


Figure 1.1: Schematic draw (left) and photograph(right) of the photocatalytic reactor for water purification [17].

dioxide, the surface area of the material and the charge carrier separation inside the material. Defect chemistry, as well as, defect physics is used to manipulate these parameters. Nevertheless, the commercial titanium dioxide Degussa P25 powder is still one of the most efficient photocatalysts despite it includes a relatively high amount of a photocatalytic non-active phase. This case shows, that, although, the influencing parameters are widely studied separately as well as their synergy [20–24], for example by a detailed surface science approach in understanding heterogeneous photocatalysis [25], the direct relation of these parameters and the enhancement of the efficiency is still not well established. Probably, this is caused by the complexity of the whole photocatalytic process. The aim of this work is the analysis of the influencing parameters on the photocatalytic activity of different titanium dioxide systems with respect to a newly designed water purification application.

During this work, a new photocatalytic reactor for water purification from pharmaceutical drugs and agricultural pesticides is designed and patented in collaboration with the work group 'Ciencias dos materiais' at the Universado do Algarve in Faro [17]. The installation is shown in figure 1.1. This reactor features a stationary photocatalytic active thin film prepared by chemical vapour deposition which provides the possibility of long term use. Additionally, the purification process is controllable through the air flow system giving the opportunity to reduce the pesticides in water nearly completely. However, an overall improvement of the photocatalytic activity of the water purification reactor is still of an high interest. Whereas, the surface area of the titanium dioxide thin film is hard to extend due to the design and the preparation of the re-

actor system. Additionally, the installed UV-light source has enough energy to create electron-hole-pairs inside the titanium dioxide thin film so that a decrease of the band gap energy by heterogeneous doping is not necessary. Hence, to improve the water purification reactor an improvement of the charge carrier separation inside the active thin film is crucial to avoid the electron-hole-recombination and increase the efficiency of the setup.

The purpose of this work is to study the charge carrier transfer characteristics inside titanium dioxide and their correlation with changes in its defect structure, as well as, with changes in its crystal structure. Therefore, titanium dioxide thin films, similar to the photocatalytic active thin film inside the water purification reactor, as well as, self synthesised powders and Degussa P25 powder samples are prepared, manipulated and analysed. The treatment of the samples is done in different atmospheres at temperatures lower than 600 °C to avoid the phase transition from the more active titanium dioxide (anatase) to the less active titanium dioxide (rutile) [26–28]. The central idea is to perform in-situ experiments in this mild temperature range because of the complexity of the photocatalytic process. To characterise the charge carrier transfer inside the titanium dioxide samples separately, new in-situ resistivity measurements are performed [29]. Additionally, the setup is also used to prepare new titanium dioxide samples with the possibility to synthesis the samples with the assistance of an external electrical field.

Furthermore, in-situ X-ray diffraction measurements are performed at the DESY, Hamburg where the structure and the resistivity are analysed simultaneously. This should lead to a better understanding of the correlation of structural changes and mild temperature anomalies of the different samples. Moreover, well established methods are used to study the chemical composition, e.g. energy dispersive X-ray measurements(EDX) and X-ray photo-electron spectroscopy(XPS), the defect structure, e.g. paramagnetic resonance spectroscopy (EPR) and XPS and the morphology, e.g. nitrogen adsorption, of the samples.

Chapter 2

TiO₂ - Basic principles and problems

Titanium dioxide, titania, is a transition metal oxide semiconductor which is widely used in current applications. Especially, its high photocatalytic activity is for interests in water cleaning industries, as well as, in many research facilities [26–28, 30]. But also in new memory technologies, the usage rate of titania is rather high, since it is considered that high defective titanium dioxide is a feasible material for new Metal-insulator-Metal nano-devices in future resistive memory cells (RRAM) [31, 32].

In the first application, the efficiency is characterised by the synergetic effect of surface properties, charge carrier excitations and charge carrier transfers. The last ones are also crucial for the resistive memory applications.

Because of this, the properties of titanium dioxide, its phases, the basic principles of photocatalysis and resistive switching as well as the influence of defects will be explained in the following chapter.

2.1 DEFECT PHYSICS

Independent of its occurrence, its phase and its modification (powder, thin film or bulk), titania is a non-stoichiometric compound which can be described as [33–39]:



with an homogeneous p-type doping x and an homogeneous n-type doping y .

This means that titania always include natural defects which have to be carefully defined. Figure 2.1.1 shows a schematic draw of possible lattice defects. They are distinguished as:

- Ti_i^{3+} : interstitial titanium cation characterised by a high mobility
-

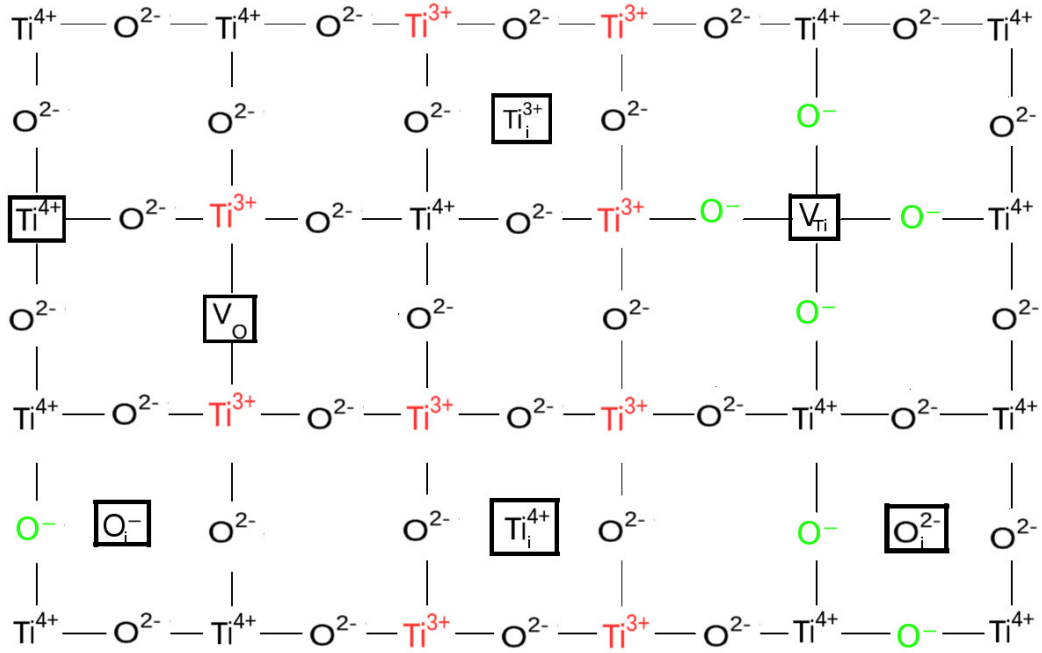


Figure 2.1.1: Schematic draw of a titanium dioxide 2D-lattice with the different types of defects [29, 33].

- Ti^{3+} : lattice titanium with a reduced oxidation state of 3+ because of an unpaired electron. This can be caused by heterogeneous doping with a cation, by homogeneous doping by titanium interstitials, by line defects or by oxygen vacancies V_O . All cases are leading to a different amount of lattice defects. A Ti^{3+} lattice defect can be seen as a quasi-free-electron.
- V_O : Oxygen lattice vacancy which will result in a reduced titanium state Ti^{3+} .
- O_i^{2-} : interstitial oxygen anion in analogy to Ti_i^{3+}
- O^- : lattice oxygen defect with an oxidised oxidation state of 1-. This can be caused by heterogeneous doping with a foreigner anion, by homogeneous doping by oxygen interstitials or by a titanium lattice vacancy. Analogous to the Ti^{3+} , the O^- can be seen as an quasi-free-hole.
- V_{Ti} : Titanium lattice vacancy which will result in oxygen with higher oxidation state O^- .

In this work, homogeneous doping is of high interest, especially the n-type doping. Therefore, Ti^{3+} and oxygen vacancies need to be carefully studied. These defects can be secondarily characterised by their localisations inside the crystal lattice. Either Ti_L^{3+} and $V_{O,L}$ can be well localised on defined lattice positions or Ti_D^{3+} and $V_{O,D}$ are de-localised and the possibility is nearly equal for all lattice positions to occupy such a quasi-free-electron [40].

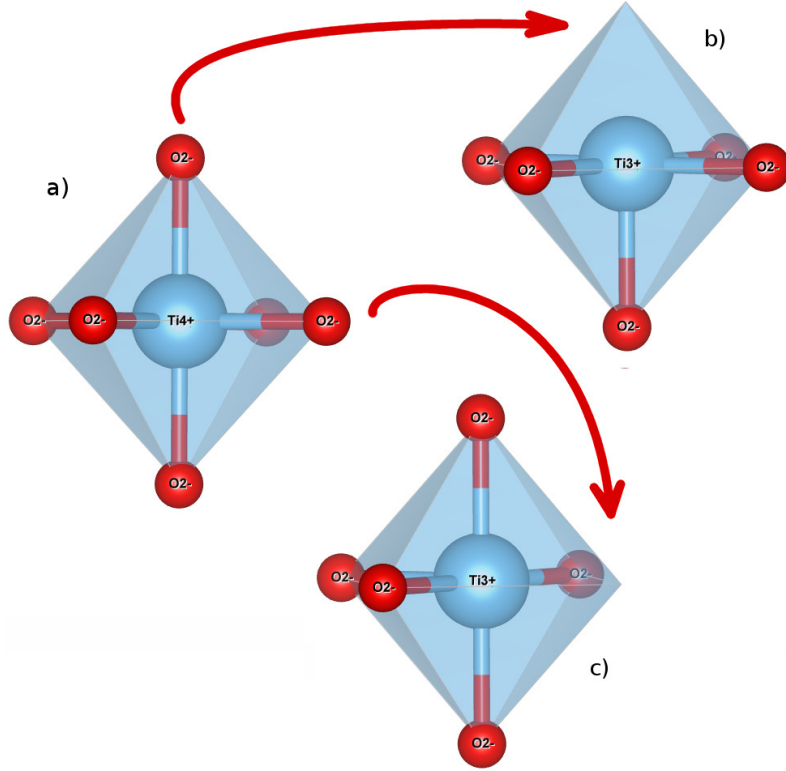


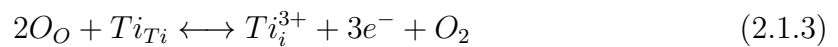
Figure 2.1.2: Perfect titania octahedron(a), octahedron with a top defect(b), octahedron with a plane defect(c), plotted by [41], modified from [42].

2.1.1 POINT DEFECTS

Independent of the phase (anatase, rutile, brookite), a titania crystal structure is always constructed out of TiO_6 octahedrons, like it is shown in figure 2.1.2a) [26]. The crystal structures differ of how this octahedrons are connected inside the unit cell.

An oxygen defect, Ti^{3+} or V_O , can be created either on the top of the octahedron or in the central plane. A perfect TiO_6 octahedron has no resulting dipole moment in contrast to defective ones. The position of the vacancy determine the resulting dipole moment of the octahedron.

Generally, these lattice defects can be formed by calcination in an oxygen-poor atmosphere at elevated temperatures. Using the standard Kröger-Vink notation for defects in transition metal oxides [43], this process can be described by the following equilibria [35, 40]:



with lattice oxygen O_O , lattice titanium Ti_{Ti} , lattice oxygen vacancies V_O and titanium interstitials Ti_i^{3+} .

The transformation of each equilibrium constant of these reactions $K_{V_O, Ti^{3+}}$ leads to

the concentration of lattice defects inside the titanium dioxide systems [35, 40]:

$$[V_O] = K_{V_O} n^{-2} p(O_2)^{-\frac{1}{2}} \quad (2.1.4)$$

$$[Ti_i^{3+}] = K_{Ti^{3+}} n^{-3} p(O_2)^{-1} \quad (2.1.5)$$

with the surrounding oxygen pressure $p(O_2)$ and the concentration of electrons n .

Additionally, the kinetic constants of these reactions are also depending on the temperature:

$$K_j \sim e^{-\frac{E_j}{k_B T}} \quad (2.1.6)$$

with the formation energy of each defect E_j where $j = V_O, Ti^{3+}$. The theoretical calculated formation energies and the diffusion energies for the lattice oxygen vacancies for various titanium dioxide phases can be found in table 2.1.1 [44].

The literature data shows that the anatase phase prefers to form bulk vacancies while in the rutile configuration the formation of surface vacancies is more probable. Moreover, it is more likely to create oxygen vacancies in the top-to-top axis of the TiO_6 -octahedrons than oxygen vacancies inside the plane independently of the crystal phase. Nevertheless, the formation energies are relatively high compared to the oxygen vacancy diffusion energies. This diffusion energies vary from 1.10 eV to 2.65 eV. Furthermore, the diffusion energy of a lattice oxygen vacancy from a bulk state to the bridging oxygen state which connects the surface with the bulk is given with $E_{V_0,d} = 0.3 \text{ eV}$ [44]. Therefore, the diffusion of lattice defects can be an important parameter in mild temperature range.

Table 2.1.1: Lattice oxygen vacancies formation energies calculated by DFT-method from [44].

Formation Energy, eV	Surface		Bulk	
	Top-Top	Plane	Top-Top	Plane
Anatase (101)	4.25	5.40	3.65	4.03
Anatase (001)	4.72	5.52	4.34	5.08
Rutile (110)	4.01	4.56	4.83	5.23

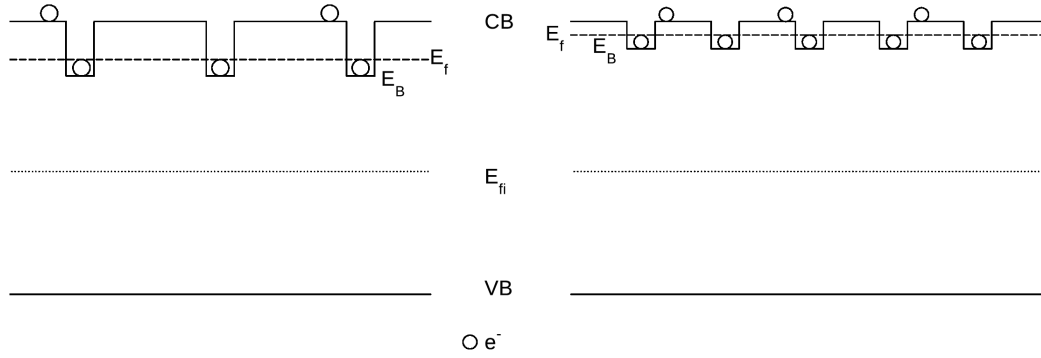


Figure 2.1.3: Schematic representation of the band structure of a semiconductor with lattice defects resulting in a conduction band with charge carrier traps, from [29]. It shows the difference between a low defective n-type semiconductor(left) and a high defective n-type semiconductor(right).

2.1.2 CHARGE TRAPPING

As mentioned in the last section, lattice defects of a semiconductor can be seen as dopants. Figure 2.1.3 shows a schematic of the band structure of such a self-doped semiconductor with [29, 45, 46]:

- E_C : energy of the conduction band
- E_V : energy of the valence band
- E_G : gap energy, $E_C - E_V$
- E_{fi} : intrinsic Fermi-energy
- E_f : Fermi energy
- E_b : barrier energy, defined by the energy level of the charge carrier trap

The trapping current can be expressed as the conductivity σ of a semiconductor in dependency of the temperature T [29, 45]:

$$\sigma \sim T^{-\frac{1}{2}} e^{\frac{E_b}{k_B T}} \quad (2.1.7)$$

with the energy barrier E_b and the Boltzmann constant k_B .

Resistivity measurements over the temperature for the semiconductor can be used to determine the barrier energies of the traps due to this correlation. For linear sections the following equations are valid for low doped material according to [45, 47]:

$$\frac{d(\log(R))}{d(\frac{1}{kT})} = \frac{1}{2} E_G - E_f \quad LN \leq Q_t \quad (2.1.8)$$

$$\frac{d(\log(R))}{d(\frac{1}{kT})} = E_b \quad LN \geq Q_t \quad (2.1.9)$$

with grain size L , defect concentration N and the traps per grain boundary Q_t . Strongly reduced titanium dioxide will result in a Fermi-energy closer to the conduction band which implicates a lower energy barrier compared to moderately reduced titania. This means, a strong decrease of resistivity at higher temperatures represents the trapping current of a low doped semiconductor and a small decrease in resistivity represents the trapping current of a highly doped semiconductor.

2.1.3 SURFACE CHANGING PROCESSES

Heat treatment of titanium dioxide samples does not only change the defect structure of the samples it also changes the morphology significantly even in mild temperature range. The manipulation of the morphology influences the surface area as well as the pore structure of a sample. During the calcination of titanium dioxide powders and titanium dioxide thin films below the phase transitions temperature four different surface changing processes may occur.

Firstly, a strong pore formation during the reduction of absorbed organic materials and water [48–50]. Depending on the oxygen content of the surrounding atmosphere new pores are formed by burning or evaporating these absorbed contents, respectively. For heat treatment in vacuum evaporation is favourable and will proceed during the calcination up to 180 °C. It will result in the formation of non-uniform micro- and meso-pores probably in ink-bottle or cylindrical shape. The overall surface area will increase [29, 51].

Secondly, aggregation took place in the temperature range from 180 °C to 500 °C [50]. In this case, particles are formed based on van-der-Waals-interaction between the material. It is characteristic for titanium dioxide powders and leads to a increase of specific surface area due to an enhanced micro-pore formation [50, 51]. The aggregation process is favourable for powders heat treated in oxygen rich atmosphere.

Thirdly, agglomeration took place in the temperature range from 180 °C to 500 °C [50, 52]. In contrary to the aggregation, grains are formed based on chemical bonds, such as ionic bonds or covalent bonds. Grains are characteristic for bulk samples or thin films but could also be observed in powders [50–52]. Since the grain formation is connected with closing micro-pores it will lead to a significant decrease of surface area. Furthermore, the pore size distribution of agglomerated samples shows a dominant meso-pore regime of uniform-shape. Titanium dioxide is known for a strong agglomeration during heat treatment in reducing atmosphere with a maximum of meso-pores of uniform shape at 430 °C [48, 49].

Fourthly, the morphology of the samples is significantly changed by crystallite growth

and phase transition. Both processes affected the pore size distribution, aggregation and agglomeration of the samples. It could cause a minimization of pores and decrease the surface area, but it could also cause a minimization of agglomeration decrease the interface area and increase the surface area of the samples [49, 51]. Nevertheless, the crystallite growth, $G(t,T)$, can be estimated with the normal crystallite growth model [53–55]:

$$G^2 - G_0^2 = 8\delta^2\gamma_0\mu(T) \quad (2.1.10)$$

with the initial crystallite size G_0 , the average atomic jumping distance δ , the interfacial energy γ and the grain boundary mobility $\mu(T)$.

For titanium dioxide equation 2.1.10 predicts a significantly increase of the crystallite for temperatures higher than 500 °C [55, 56]. Furthermore, the phase transition temperature from anatase-to-rutile of around 600 °C is also relatively high [26]. This means, differences in surface area and pore size distribution of different titanium dioxide samples should be connected with well defined processes which are dominant at the calcination temperature of each sample.

2.2 CRYSTAL STRUCTURE

Titanium dioxide is able to crystallise in different crystal structures. The most common crystal structures are anatase and rutile, shown in figure 2.2.1, but also brookite or reduced titania phases in monoclinic structure are known [26, 48, 57, 58].

Nevertheless, every titania structure in the literature is based on TiO_6 -octahedrons with covalent Ti-O-bonds. The top-top-axis of the basis octahedron in the unit cell is defined as the O-Ti-O bond with the maximum length which is important for the lattice position of possible defects. The unit cells with the basic octahedron are represented in figure 2.2.1.

2.2.1 ANATASE

Anatase is described as the most photocatalytic active but thermodynamically metastable phase of titanium dioxide. It is possible to synthesise pure anatase in form of nanoparticles with different bottom-up-methods, e.g. the sol-gel-method, because of its lower free surface energy compared to rutile. This means stable anatase nanoparticles can be produced under normal pressure up to the crystallisation temperature of 450 °C [59–62].

Anatase is a wide gap semiconductor with a band gap energy of 3.2 eV and is the major phase inside the Evonik Degussa P25 powder, the reference powder for every experiment in this work, with about 83% weight fraction [63].

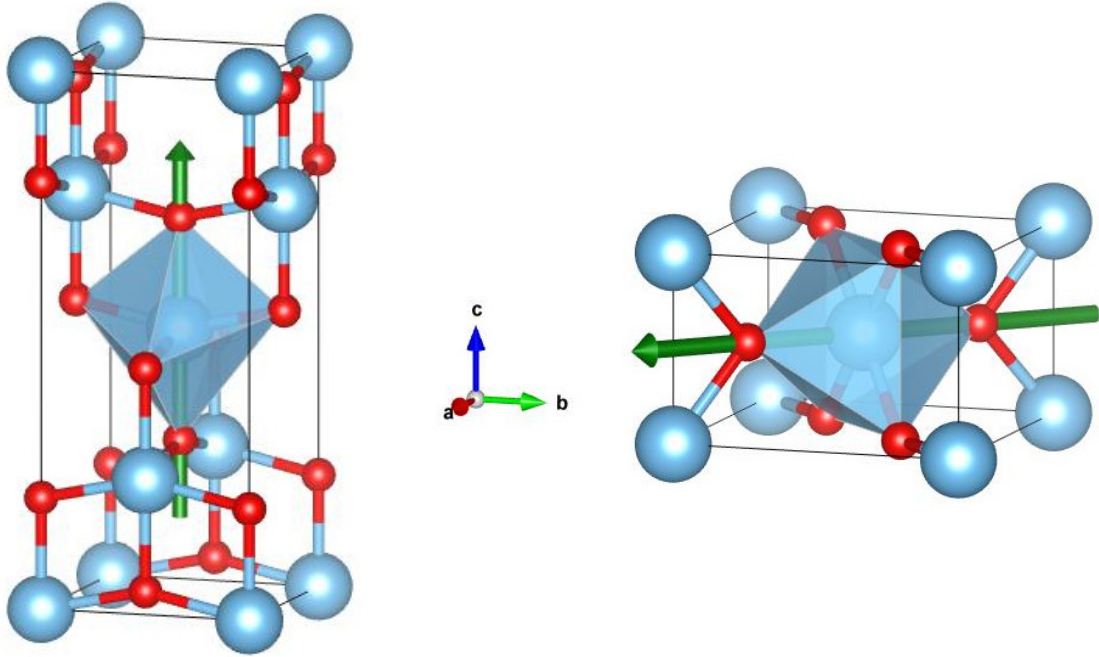


Figure 2.2.1: Ideal crystallite unit cells of anatase (left) and rutile (right) plotted by [41]. The blue bullets are representing Ti^{4+} atoms and the red bullets are representing O^{2-} atoms. The green vector represents the top-to-top axis of the basic TiO_6 -octahedron. The figure is modified from [42].

2.2.2 RUTILE

The thermodynamically stable phase of titanium dioxide is the rutile phase. Anatase, as well as brookite, a third titanium dioxide crystal structure, will be transferred to rutile after reaching the phase transition temperature. This transition is irreversible which limits rutile to be the only usable phase for high temperature applications [5, 26, 28].

The band gap energy is 3.0 eV, but rutile is not as photocatalytically efficient than anatase [51]. It is considered that the electron-hole-recombination time is shorter than in anatase which limits the efficiency of rutile [5, 26, 30]. This theory is not confirmed, yet. More simple reasons could be the higher surface area of anatase because of the smaller particle size. Therefore the photocatalytic efficiency should be normalised to the surface area [51]. Another reason can be that the energy level of the conduction band of rutile is smaller than the necessary dissociation energy of the aimed chemical process which will avoid a photocatalytic degradation [64, 65].

2.2.3 PHASE TRANSITION

As mentioned before, the anatase to rutile phase transition is irreversible. Important for the phase stability is the Gibbs free energy, a thermodynamic potential defined

as [66]:

$$G = H - T \cdot S + (p + p') \cdot V + \gamma \cdot A + \phi \quad (2.2.1)$$

with the Gibbs free energy G , the enthalpy H , entropy S , temperature T , surrounding atmospheric pressure p , internal pressure of the material p' , volume V , free surface energy γ , surface area A and remaining factor for shape or porosity ϕ .

Every system tries to minimize this Gibbs free energy. So a phase transition from anatase, A, to rutile, R, will be performed when the following equation is fulfilled [62]:

$$\Delta G^{A \rightarrow R}(T, r) = \Delta G^A(T, r) - \Delta G^R(T, r) \stackrel{!}{=} 0 \quad (2.2.2)$$

with the crystallite radius r . It is obvious that there is a critical crystallite size for the phase transition which explains why the transition temperature for the anatase to rutile transformation varies from 550 °C to 700 °C in the literature [67].

In the beginning of the phase transition, covalent bonds of the bridging oxygen between the TiO_6 -octahedrals from the titania structure are broken, then getting re-organized from the anatase to the rutile crystal structure, ending in forming new bridging oxygen covalent bonds. This results in new unit cells, plotted in figure 2.2.1, where octahedrons share only two edges with their neighbour in case of the rutile phase instead of three edges in case of the anatase phase. This leads to a more stable crystal structure [68].

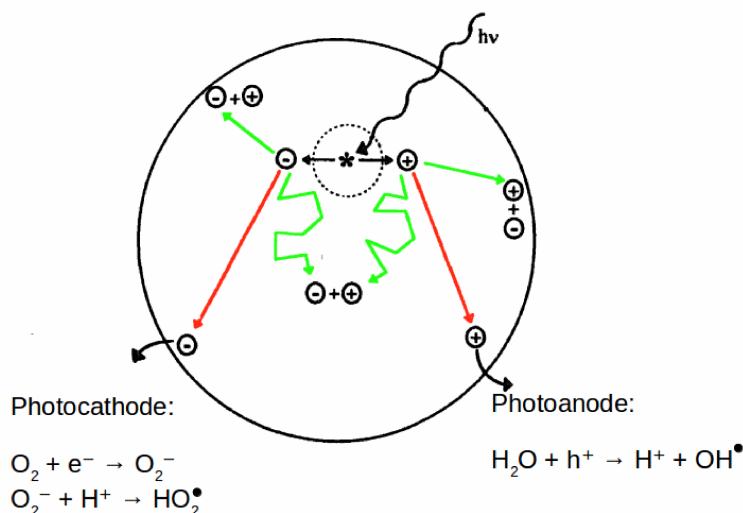


Figure 2.3.1: schematic draw of the charge carrier formation and charge carrier diffusion inside the semiconductor during the photocatalytic process modified from [19], the green paths leads to electron-hole-recombination and avoids any photocatalytic process.

2.3 PHOTOCATALYSIS

A light driven support of a chemical reaction is called photocatalysis. This effect is the basis of important future applications such as water cleaning processes or hydrogen generation by supporting the hydrolysis of water. Titanium dioxide is the most used metal-oxide-semiconductors in photocatalysis because of its high efficiency compared to other oxide-semiconductors [15, 19, 26, 28, 30, 34, 51, 69–71].

Figure 2.3.1 shows a summary of the charge carrier formation and charge carrier diffusion inside a semiconductor material during the photocatalysis. Starting with a photon which excite an electron-hole-pair (e^-h^+ -pair) inside the semiconductor bulk material, this electron-hole-pair needs to be separated and the charge carriers start to diffuse. When these charge carriers are able to diffuse to the surface (green paths) without any bulk or surface recombination (red paths) they can react with adsorbed molecules on the surface of the semiconductor. There is a radical formation following the equation 2.3.1 for the anodic site (donor site) or 2.3.2 and 2.3.3 for the cathodic site (acceptor site) [34, 69, 71]:



The formed radicals can force degradation of organic pollutants in water or support the electrolysis of water in hydrogen and oxygen. For example, the degradation of a

organic pollutant $R - H$ supported indirectly by the donor site [69]:



leads to the formation of new radicals in water R'^\bullet which are important for the further degradation.

In many research projects the influence on the efficiency of this photocatalytic process is of a high interest. There are three major parameters that can be changed to enhance the photocatalytic performance, which will be shortly introduced:

BAND GAP

Many active photocatalysts such as zinc oxide or titanium dioxide have a band gap energy larger than 3.0 eV which is in the UV-range of the solar spectrum. It is obvious, that shifting the band gap energy to a lower value in the visible light range could be an easy way to increase the efficiency. In many studies, this had been done by doping the metal-oxide-semiconductor with metals (e.g. iron [25], silver [25, 72]) or non-metals (e.g. nitrogen [25, 73]). While this will lower the band gap it is not increasing the overall efficiency for titanium dioxide by using solar light [25, 71, 74].

SURFACE

Another idea of improving the photocatalytic process is to increase the pure surface area of the support material. Because a larger surface area will allow to adsorb a higher amount of molecules, water and oxygen which will react with the charge carriers to create the crucial radicals [18, 30, 75, 76].

Good adhesive properties and a high hydrophilicity of the material are also surface properties which will influence the overall efficiency.

CHARGE CARRIER TRANSPORT

The last parameter is the possibility to transfer the charge carriers from the bulk to the surface by avoiding the electron-hole-recombination since this process will lead to a loss of charge carriers that can support the degradation of organic pollutants or the electrolysis of water. In this case, diffusion centres inside the material are necessary to apply an enhanced electron-hole-separation and to form locally separated anodic and cathodic sites [27, 30, 39, 77, 78].

2.3.1 SYNERGETIC EFFECT

There is a synergetic effect between two phases during photocatalysis when the following equation is fulfilled:

$$k_{(\alpha \cdot 1 + \beta \cdot 2)} > \alpha \cdot k_1 + \beta \cdot k_2 \quad (2.3.5)$$

with phases 1 and 2, the weight ratios α and β of the phases and the kinetic constant of the photocatalytic degradation k . This means that the photocatalytic efficiency of the mixture of two phases is larger than the sum of the single phases.

The synergetic effect between anatase and rutile is often part of the discussion why the Evonik Degussa P25 powder has a high photocatalytic efficiency. Studies show that there is no synergetic effect between the two titania phases, because there is no exciton transfer from one phase to the other [63]. This means that the whole photocatalytic process takes place in a single phase for itself.

Although, some special photocatalytic processes, e.g. oxidation of naphthalene, are fulfilling equation 2.3.5 [63,79]. In this case it is considered that molecules are attracted to anatase because of its larger surface area forming radicals with charge carriers of the rutile phase. By performing a similar experiment with pure rutile the surface area is too small to attract the same amount of molecules and decrease the overall kinetic constant of the degradation [79]. It is necessary to distinguish between these two principles of a synergism between the titania phases.

Chapter 3

Methods

The following section focuses on the methods that are used during this thesis to characterise and synthesis the titanium dioxide samples. On one hand, there are well established characterisation techniques which will be shortly introduced. On the other hand, unique own build setups are designed and used, especially, the in-situ resistivity measurements. These setups will be explained in more detail.

3.1 CHARACTERISATION

3.1.1 X-RAY-DIFFRACTION

Structural differences between the analysed samples are determined using X-Ray-diffraction experiments. On one hand, the XRD facility of the 'Faculdade de Ciencias Tecnologia' of the 'Universidade do Algarve' in Faro, Portugal is used to analyse the crystal structure of the heat treated Degussa P25 powder samples. A high-resolution PANalytical x'PertPRO XRD setup is used which works with Cu-K α -radiation, $\lambda = 0.154184 \text{ nm}$ and in $\theta - 2\theta$ -configuration [51].

On the other hand, high energy synchrotron radiation at the P07 beam line at HASYLAB, DESY in Hamburg, Germany, is used to study various titanium dioxide samples. Firstly, titanium dioxide thin films and Degussa P25 pellet samples are analysed at room temperature. The experiments are performed in transmission geometry and the diffraction patterns are collected with an 2D-area detector characteristics of short read-out time. The beam energy is 87 keV which corresponds to a wavelength of $\lambda = 0.01425 \text{ nm}$.

Secondly, in-situ experiments are performed to study the structural dynamics of selected titanium dioxide samples. These experiments performed in vacuum during heating and additionally, with and without an external electrical field applied. The setup is explained in detail in section 3.1.1.

Each XRD-pattern is evaluated by Rietveld refinement procedure either using FullProf

program or using MAUD program [80,81]. This procedure is based on the minimization of the weighted sum of squares and fulfil the equations [82,83]:

$$y = \sum \frac{1}{I_i^{exp}} (I_i^{exp} - I_i^{theo})^2 \quad (3.1.1)$$

with the measured intensity of the XRD experiment I_i^{exp} and the theoretical calculated intensity I_i^{theo} :

$$I_i^{theo} = C \cdot \sum_{k=1}^n \sum_j L_j \cdot |F_j|^2 \cdot S(2\theta_i - 2\theta_j) \cdot P_j \cdot A_i + b_i \quad (3.1.2)$$

This equation includes the background intensity b_i , the absorption coefficient of the sample A_i and for every phase $k = 1..n$ and its correlated peaks j the factors for [59,82]:

- the beam intensity C
- the polarisation of the beam L
- the structure factor of the crystals F
- the profile factor of the reflex, normally a Pseudo-Voigt, S
- the texture factor P

It is obvious that the Rietveld refinement provides detailed information about the phase composition, the crystallite size, the unit cell parameters, the micro-strain and the textural properties of the titanium dioxide samples.

In the last step, the program VESTA [41] is used to visualise the crystal structure of the titanium dioxide samples and calculate the dimensions of titanium dioxide octahedrons by plotting a titanium dioxide unit cell using the theoretical calculated Rietveld parameters from the refinement procedure which includes the unit cell parameters and the atomic position parameters for selected titanium dioxide samples.

The detailed Rietveld refinement procedure and its adaption for VESTA are described in [41, 80, 82].

IN-SITU-EXPERIMENTS

The photocatalytic mechanism is highly complex which means a detailed knowledge of the dynamics during the material manipulation is crucial. It is necessary to study the structural dynamics of the titanium dioxide samples by in-situ measurements to analyse the influence of the heat treatment on the charge carrier transfer ability of titanium dioxide. This means, that the whole treatment process needs to be done during the XRD experiments. Therefore, a unique furnace is designed which offers the

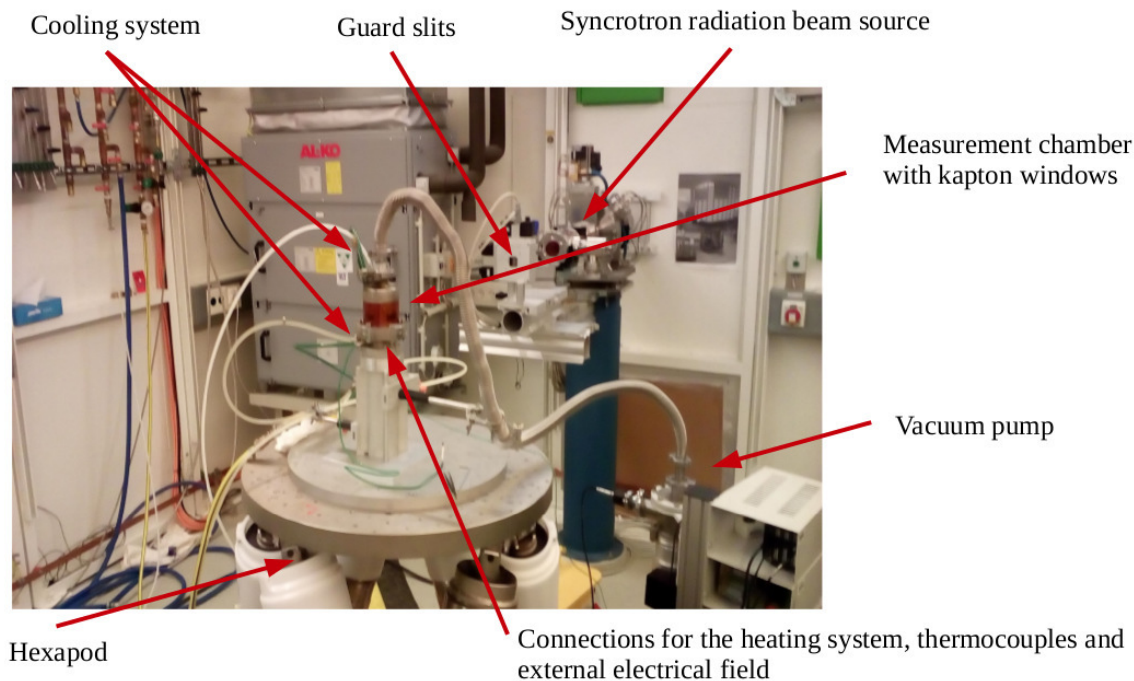


Figure 3.1.1: Photography of the own build furnace for in-situ XRD experiments at the P07 beamline at the HASYLAB of the DESY, Hamburg.

possibility to anneal the samples in an oxygen poor atmosphere with and without an external electrical field. Additionally, this furnace needs to be transportable.

Figure 3.1.1 shows the resulting furnace which was designed during this work with the help of the mechanical workshop of the Institut of Physics of the Universität Rostock, Germany. It is based on a small recipient with three kapton windows to be able to measure the crystal structure in transmission geometry. Two independent water cooling systems are installed in the top part and in the bottom part of the furnace. Through the bottom of the setup, there are six electrical penetrations and two thermocouple penetrations installed which are sealed with epoxy resin.

The heating unit is a copper coil, figure 3.1.2, which includes a heating wire that operates at a current of 4 A. The wire is fixed with two stainless steel rings. It is necessary to use identical rings at the top and at the bottom to ensure that the calcination of the sample, fixed on a sample holder in the central window, is homogenized and without strong temperature gradients.

The sample holder are made from copper which means the titanium dioxide samples needs a dielectric screening. This is realised by using mica foil with a window for screening from the sample holder and by using glass for fixation. The mica foil is a high temperature dielectric material [84].

A photography of the sample holder from the front and from the rear after the alignment of the setup at the P07 beamline is shown in figure 3.1.2. This was the measurement of a Degussa P25 pellet heated in vacuum with an external electrical

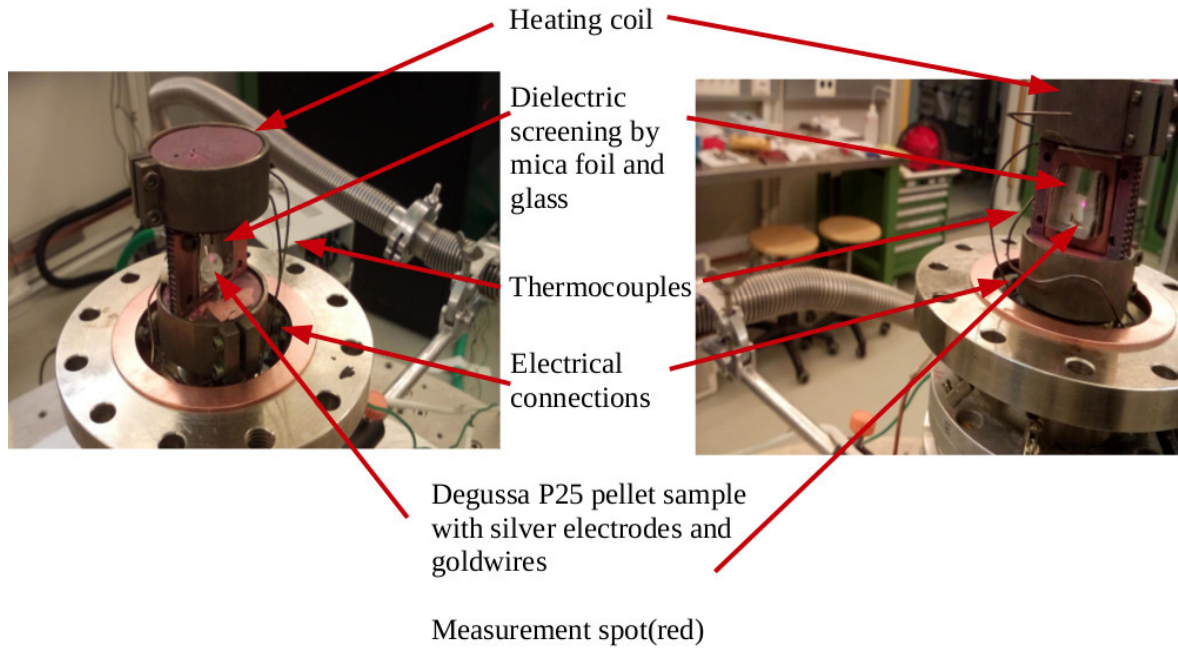


Figure 3.1.2: Photography of the heating coil and the sample holder of the own build furnace for in-situ XRD experiments after the alignment and before the measurement of a Degussa P25 pellet with an applied external electrical field.

field applied tangential to the surface. It can be seen that the measurement spot is close to the silver electrode but it is not penetrating the mica foil.

The in-situ experiments are carried out with a beam diameter of $600\ \mu\text{m}$ with a beam energy of 100 keV which corresponds to a wavelength of $\lambda = 0.012\ \text{nm}$. The electrical circuit is similar to the measurement circuit in chapter 3.1.4.

3.1.2 SURFACE AREA AND POROSITY

The deposition of gas molecules on solid surfaces is called adsorption and offers the determination of the morphology of nanostructured powders. Adsorption processes are distinguished into chemisorption and physisorption based on the nature of the gas to solid bonding type. For morphology determination physisorption experiments are preferred, because the long ranged van-der-Waals interaction between gas molecules and the surface allows a multilayer adsorption. This leads to the possibility of a qualitative and quantitative analysis [85–87].

N_2 -ISOTHERM

In principle, any gas can be physisorbed on any solid surface. In experiments the adsorption of nitrogen gas at a surrounding temperature of 77 K is preferred. The amount of adsorbed molecules at a constant temperature depends on the surrounding pressure. During nitrogen adsorption experiments a $n_{ads} v_S \frac{p}{p_{0,77K}}$ -isotherm is measured with the amount of adsorbed gas molecules n_{ads} , the surrounding pressure p and the saturation pressure of nitrogen at 77 K $p_{0,77K} = 1 \text{ bar}$.

An experimental setup for measuring nitrogen adsorption-desorption isotherms consists of a sample tube with a known volume V_{tube} , a gas inlet and a pressure gauge. The whole system is placed in a liquid nitrogen bath to guarantee a constant temperature. During a measurement step for a defined pressure-ratio $\frac{p_{inlet}}{p_{0,77K}}$ the sample tube is filled with nitrogen up to the aimed pressure of p_{inlet} . The system is then closed. The nitrogen will adsorb on the material and the pressure inside the tube is controlled until it reaches a constant value p_{equi} . At this point the adsorption and desorption of nitrogen is in an equilibrium. The amount of adsorbed molecules can be calculated by the ideal gas law [85, 88]:

$$n_{ads} = \frac{R \cdot T}{(p_{inlet} - p_{equi}) \cdot V_{tube}}$$

By measuring n_{ads} over the pressure-ratio $\frac{p_{inlet}}{p_{0,77K}}$ from 0.005 to 1 one obtains the adsorption branch of the isotherm and the pressure ratio from 1 to 0.2 the desorption branch. The complete isotherm is the basis for both analyses.

QUALITATIVE ANALYSIS

For a qualitative analysis of the morphology the shape of the isotherm is crucial. It is classified by IUPAC [50, 89] and determine the average particle shape, pore shape and pore types.

The classification of pores by its size d is defined by the IUPAC [89]:

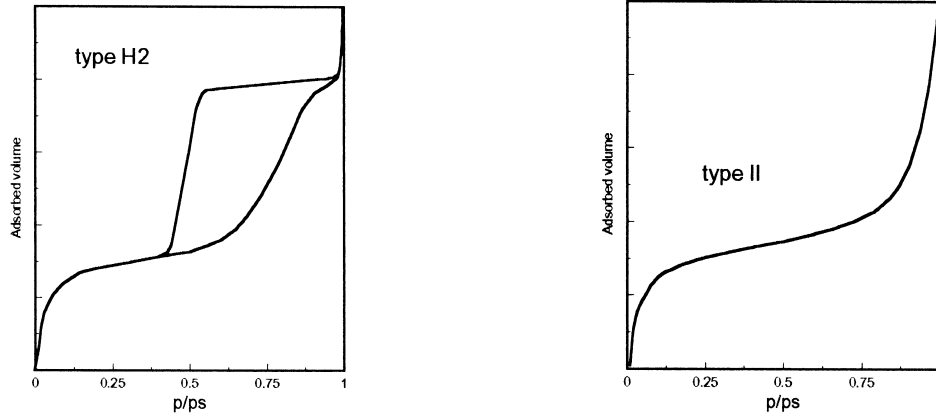


Figure 3.1.3: Examples of isotherms of a mesoporous catalysts material with open pores(left) and closed pores(right) from [89].

- micropores : $d \leq 2 \text{ nm}$
- mesopores : $2 \text{ nm} < d \leq 20 \text{ nm}$
- macropores : $20 \text{ nm} < d$

Typical isotherms for mesoporous materials are shown in figure 3.1.3. They are characterized by a steady slope of adsorbed gas, especially between $0.05 \leq \frac{p}{p_{0;77K}} \leq 0.8$. The presence of a hysteresis means the presence of open pores. Inside open pores capillary effects leads to locally higher pressure compared to the outside and to capillary condensation. Therefore, the amount of gas molecules layers on the surface is not uniform and the desorption branch is not equal to the adsorption branch. The shape of the hysteresis defines the shape of the open pores, whether they are cylindrical, ink bottled, or slit shaped [50]. The given example in figure 3.1.3 shows a type IV-isotherm with an H2-hysteresis characteristic for photocatalytic transition-metal-oxide powders.

QUANTITATIVE ANALYSIS

The isotherms can also be used for a quantitative analysis which includes the calculation of the surface area by BET-method.

The BET-method is a widely used method to calculate the surface area of a material [50, 87, 88]. It is assumed that the formation of multilayer adsorption is possible while there is no direct interaction between these layers. This leads to a simplified equation 3.1.3:

$$\theta = \frac{c \cdot \frac{p}{p_0}}{\left(1 - \frac{p}{p_0}\right) \left(1 + [c - 1] \frac{p}{p_0}\right)} \quad (3.1.3)$$

with the coverage $\theta = \frac{n_{ads}}{n_{max}}$ the maximum amount of molecules for one layer n_{max} and the velocity constant c .

In the pressure range of

$$0.05 \leq \frac{p}{p_0} \leq 0.35$$

a linear behaviour of n_{ads} vs $\frac{p}{p_0}$ is observable resulting in the linear BET-equation:

$$\frac{p}{n_{ads}(p_0 - p)} = \frac{1}{n_{max}c} + \frac{c - 1}{n_{max}c} \cdot \frac{p}{p_0} \quad (3.1.4)$$

The critical assumptions can be made, because the monolayer formation is completed at $0.05 \leq \frac{p}{p_0}$ and the pore effects are negligible at $\frac{p}{p_0} \leq 0.35$ which result in the linear behaviour and the possibility to calculate the monolayer coverage and the specific surface area [88].

EXPERIMENT

To determine the specific surface area and the pore size distribution, a Micromeritics ASAP 2020 is used. Before the measurement the samples were degassed at 323,15 K for 10 h at a pressure of 50 mmHg. The weight of the sample is determined before and after the measurement. A isothermal adsorption of nitrogen is done at 77 K. The specific surface area is calculated by the BET equation in the range of $0,05 \leq \frac{p}{p_0} \leq 0,25$. The pore size distribution and pore area is calculated by the BJH theory with Halsey correction in the range of $0,42 \leq \frac{p}{p_0} \leq 1$ of the adsorption branch [51].

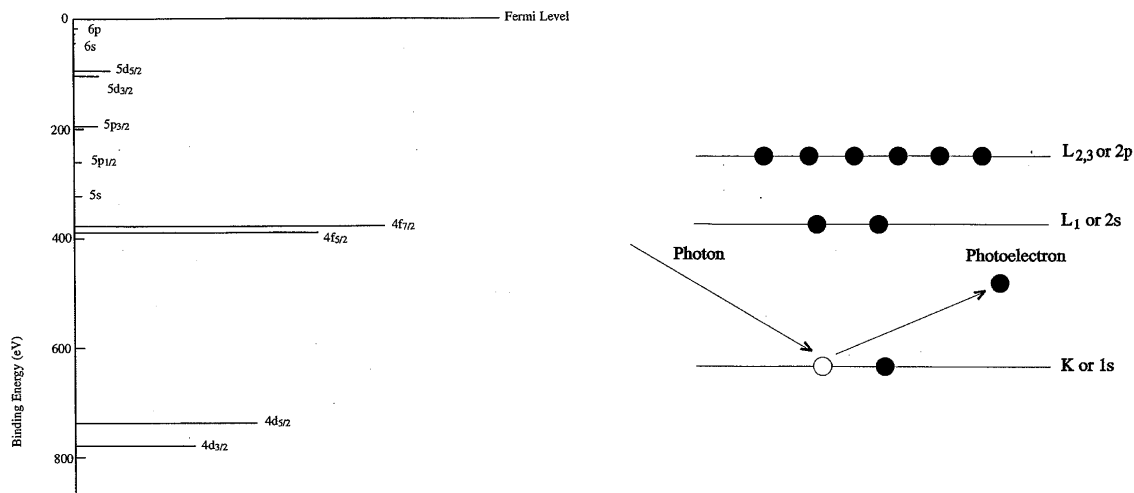


Figure 3.1.4: Example of binding energies depending on the Fermi-energy(left) of Uranium and scheme of photoelectron emission process(right) from [91].

3.1.3 CHEMICAL COMPOSITION

There is a strong interest to determine the purity of a material to be sure that there are no foreigner atoms inside and that there is the exact stoichiometric relation of a metal-oxide-ratio to discuss the influence of self-doping on physical and chemical properties [40,90]. Therefore, measurements of the chemical composition of a material depending on the chosen system, powders, thin films or bulk materials depending on the surface sensitivity of the method is necessary. In this work a high surface sensitive method, X-ray-photoelectron-spectroscopy (XPS), a bulk sensitive method, Energy-dispersive-X-Ray-measurements (EDX), and a temperature depending method to characterize the nature of defects in powders, Electron-paramagnetic-spin-resonance-spectroscopy (EPR), are performed.

X-RAY-PHOTOELECTRON-SPECTROSCOPY

Investigating the chemical composition as well as the stoichiometric relation of a material, X-ray-photoelectron-spectroscopy is widely used. It is based on determining the binding energy of electrons emitted by soft X-rays.

Figure 3.1.4 shows the theoretical principle of binding energies related to the Fermi-energy and the emission of a photoelectron. An incoming X-Ray-photon hits an electron on a shell of an atom and this electron is emitted and can be detected. With an energy dispersive detector the binding energy(BE) of such an electron can be calculated with [91]:

$$BE = h\nu - KE - \phi_d \quad (3.1.5)$$

with the wavelength of the X-rays ν , the Planck's constant h , the measured kinetic energy of the electron KE and the working function of the detector ϕ_d .

To determine the chemical composition of different elements of a material the peak-area of one orbital of every detected element A_i is used with:

$$at\%_i = \frac{A_i \cdot \sigma_i^{-1}}{\sum_j A_j \cdot \sigma_j^{-1}} \quad (3.1.6)$$

with the sum over all detected elements, the atom weight ratio of a specific element $at\%_i$, and the cross-section of the analysed orbital σ_i . This cross-section can be understood as the possibility of a photon to hit an electron of this specific orbital relative to electrons of the 1s-orbital of the Fluor atom [91, 92]. In 3.1.4 the cross-section is illustrated as the length of the line for a energy level.

While the survey measurement mode is used to investigate the chemical composition, chosen detailed measurements analysing the binding state of an element are done. Depending on the covalent bond and on the oxidation state of an element, the binding energy of the electrons are changed for hundreds of mEV up to several eV . A carefully study with high resolution allows the calculation of the atom ratio between two different species of an element by calculating the simple specific peak area ratios. A cross-section conversion factor is not necessary, because only different bonding and oxidation states of one element are compared [92].

EXPERIMENTAL SETUP

In this work a PHI-5600-spectrometer with monochromated Al- K_α -X-Ray source is used. The setup, figure 3.1.5, is located at the IFW Dresden supervised by Prof. Knupfer. A monochromated Al- K_α X-Ray source operating at 1486.7 eV is used in combination with an electron energy analyser model 10-360 single channel analyser [91]. This analyser operates at 20 eV pass energy and 0.5 eV step width for the survey spectra and at 5.85 eV pass energy and a 0.05 eV step width for the detailed spectra.

Two different XPS experiments were performed. On one hand, selected heat treated powder samples are studied. They are kept in a floodgate at $p \approx 10^{-7} mbar$ at room temperature for 2 h before each measurement in order to clean the surface from physisorbed water and organic compounds [29].

On the other hand, Degussa P25 pellets are studied by a quasi-in-situ measurements to determine the defect dynamics in mild temperature regime. Quasi-in-situ means that the pellet samples are annealed in a preparation chamber which is directly connected with the measurement chamber to avoid any oxygen contact. The pellet samples are annealed in ultra high vacuum of $p \approx 10^{-9} mbar$ for 2 h at each temperature step between 100 °C and 350 °C. The annealed samples are analysed at room temperature after their transfer into the measurement chamber [29].

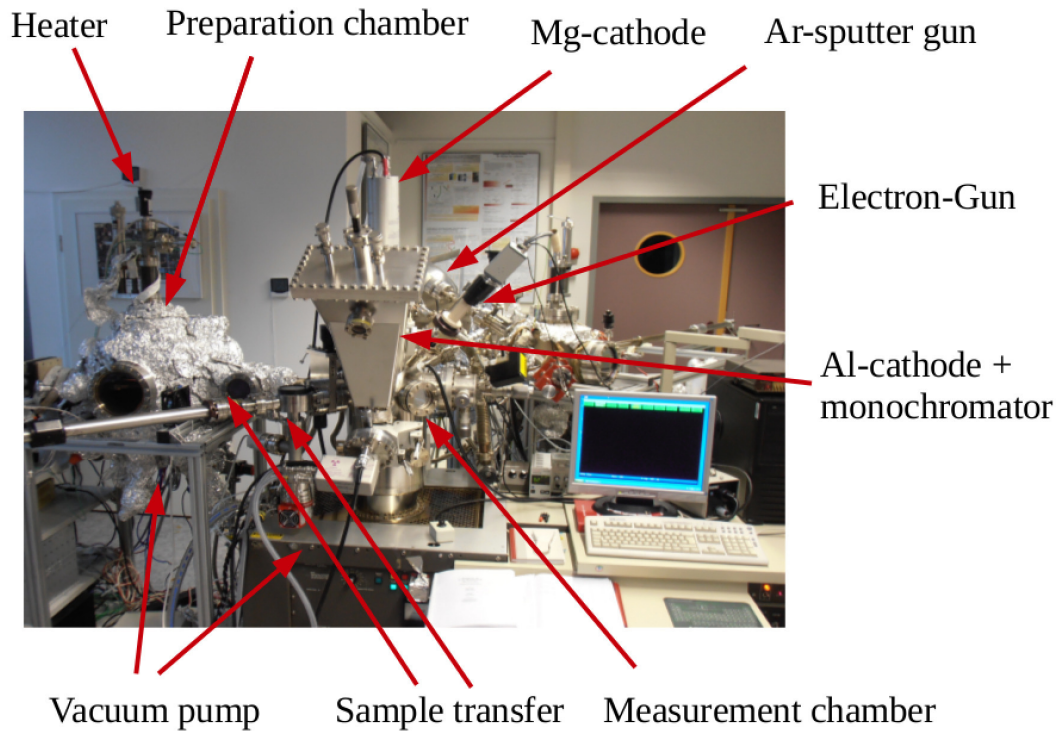


Figure 3.1.5: XPS-setup at the IFW Dresden, including a preparation chamber with an external heating system for quasi-in-situ measurements.

The chemical composition is calculated using equation 3.1.6 with the sensitivity factors σ of $\sigma_{Ti} = 1.798$ for Ti 2p, $\sigma_O = 0.711$ for O 1s and $\sigma_C = 0.296$ for C 1s from the survey spectra [29, 91]. The determination of the defect dynamics are explained in detail in chapter 2.1.

ENERGY-DISPERSIVE-X-RAY-MEASUREMENTS

Energy dispersive X-ray measurements, EDX, are a well established method to determine the atomic species inside a material. In contrary to the XPS-analysis, this method provides a increased information depth. This means, that the chemical composition of a specific bulk area can be determined instead of the surface composition [93]. Whereas, a detailed defect analysis is not possible because of high specific errors for so called light atom species, e.g. oxygen or carbon, the method is used to determine the influence of the silver glue and the copper furnace. The aim is to prove that inside the different titanium dioxide samples are no foreign atoms detectable and a silver diffusion can be neglected.

Detailed information about the EDX-principles are published elsewhere [93].

A Zeiss Supra 25 field emission SEM microscope with high resolution, equipped with a liquid nitrogen free, Peltier cooled EDX detector X-Flash 3001 with Quantax was used with the help from Regina Lange of the institute of computer science and electrical

engineering, IEF, of the Universität Rostock, Germany [94]. Depending on the nature of the samples, selected titanium dioxides are coated with carbon via sputtering to avoid any charging effects during the measurements. The microscope operates with an acceleration voltage of 16,0 kV.

ELECTRON-PARAMAGNETIC-SPIN-RESONANCE-SPECTROSCOPY

Whereas the chemical composition of the titanium dioxide bulks are analysed by EDX, the bulk defect states inside selected samples are analysed using electron-paramagnetic-spin-resonance-spectroscopy(EPR). This is a well established method in case of determining the nature of the lattice defects in different titanium dioxide systems [23, 95, 96].

The samples are placed in a external magnetic field. Microwave radiation is used to excite unpaired electrons inside the material. Unpaired electrons are a result of lattice defects. By changing the magnetic field strength a resonance frequency can be observed due to the paramagnetic spin of the excited unpaired electrons. This resonance frequency depends of the Landé-factor, g , of the different defect species. The g -values can be calculated by [29]:

$$g = \frac{h \cdot \nu}{\mu_B \cdot B} \quad (3.1.7)$$

with the Planck constant h , the microwave frequency ν , the Bohr magneton μ_B and the magnetic flux density B .

In this thesis, X-Band EPR measurements are performed using a Bruker EMX CW-microspectrometer with the help from Dr.Hollmann from the LIKAT Rostock, Germany. Approximately 15 mg of the powders or maled pellets are filled in a commercial X-band EPR tube. These samples are analysed at room temperature and at 100 K using a liquid nitrogen stream. During each experiment the magnetic field is varied between 3100 G and 3600 G while the microwave frequency is constant [24, 29].

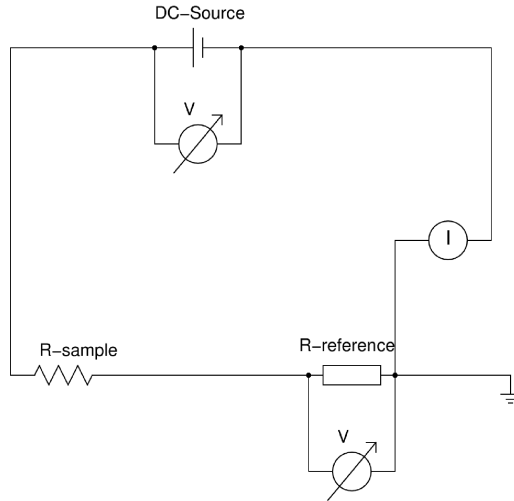


Figure 3.1.6: Schematic draw of the circuit diagram for the resistivity measurement setup, with reference resistance R_r , sample resistance R_s [29].

3.1.4 RESISTIVITY

Knowledge about the charge carrier transport inside different titanium dioxide systems is crucial to enhance the charge carrier separation during photocatalytic processes. Though, the ohmic resistivity of these titanium dioxide systems is analysed.

Firstly, cold pressed pellets were used with silver electrodes attached symmetrically in the centre of both sites of the titanium dioxide disks. The electrodes had a diameter of around 1.5 mm and were connected to the setup by gold wires [29]. It is assumed that the electrical field is directed normal to the surface of the pellet and the charge carrier transport is located through the volume of the material.

Secondly, titanium dioxide thin films prepared by CVD-method were studied with silver electrodes attached on the end of the sample at the titanium dioxide side. The electrodes had dimensions of around 1.5 mm x 1.5 mm and were connected to the setup by gold wires. It is assumed that the electrical field is directed tangential to the surface of the sample and the charge carrier transport is located in the titanium dioxide thin film, because of the non-conductive substrate material.

Figure 3.1.6 shows the applied resistive setup. Ensuring a wide range of resistivity measurable as well as a high resolution during the annealing, the resistance of the P25 sample, R_s , was measured indirectly via a reference resistance R_R . The sample resistance, R_s , was calculated by [29]:

$$R_s = R_r \frac{U_0 - U_r}{U_r} \quad (3.1.8)$$

$$R_s = 2 * R_c + R_i \quad (3.1.9)$$

with the contact resistance R_c , intrinsic sample resistance R_i , original voltage U_0 and voltage over the reference resistance U_r . Assuming that the contact resistance between the silver electrodes and the titanium dioxide is negligible compared to the intrinsic sample resistance and using equation 2.1, the resistivity ρ of pellets is:

$$\rho = \frac{R_s * A}{l} \quad (3.1.10)$$

with the thickness of a titanium dioxide disk l and the area of an electrode A .

And the resistivity ρ of thin films is:

$$\rho = \frac{R_s * t * e}{d} \quad (3.1.11)$$

with the electrode-to-electrode distance d , the thickness of a titanium dioxide film t and the dimension of an electrode e .

The samples were measured in-situ in vacuum as well as in air in different temperature ranges up to $T_{max} = 800^\circ C$.

For the vacuum measurement, the titanium dioxide samples were placed in a copper furnace inside a vacuum chamber of $\approx 5.0 \cdot 10^{-6}$ mbar. They were dielectricly screened by a quartz glass and a mica foil. Inside the furnace, two halogen lamps (1 kW) are installed as external heat sources [29].

The setup is also used to measure the I-V-characteristics of the titanium dioxide systems in different atmospheres as well as at different temperatures.

Further informations about the correlation between defect structure and ohmic resistance is explained in chapter 2.1.2.

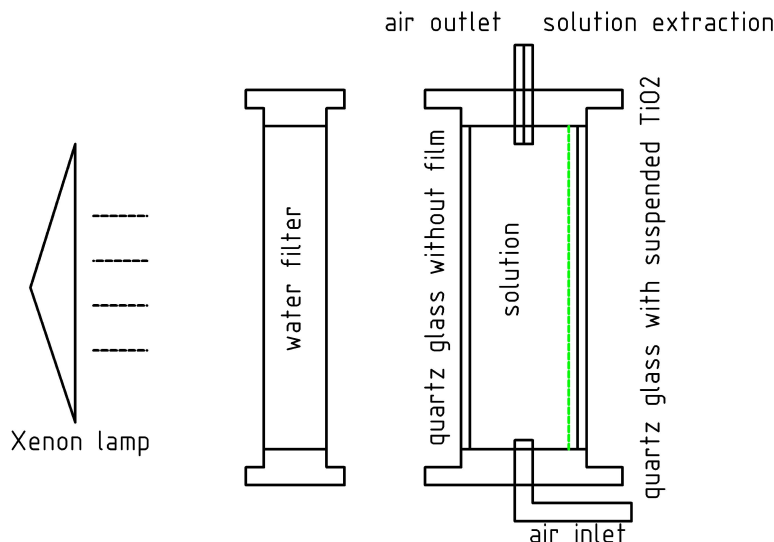


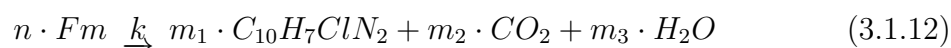
Figure 3.1.7: Schematic sketch of the photocatalytic reactor cell used in this work [97].

3.1.5 PHOTOCATALYTIC ACTIVITY

The photocatalytic process is explained in section 2.3. The determination of the photocatalytic activity of a material system is measured in an photocatalytic reactor. The reactor used in this work is shown in figure 3.1.7. It consists of a light source (Xenon-lamp), the water bath with the water-organic-pollutant-solution, a quartz-glass window, the active surface where the catalyser material is adhered, a water outlet to exclude small probes and an air inlet to cause air bubbling in the solution. This is necessary to achieve a stirring of the water and to ensure the oxygen supply during the photocatalytic reaction. Additionally, a water filter is included to prevent the photocatalytic reactor from overheating because of the Xenon lamp [51, 94, 98]. The setup is build in the chemistry department of the Universidad do Algarve supervised by Prof. Mateus.

DEGRADATION OF THE ORGANIC POLLUTANT

As organic pollutant fenarimol is chosen. The photocatalytic degradation of fenarimol is [98]:



with the fenarimol ($C_{17}H_{11}Cl_2N_2 - OH$) Fm , the overall kinetic constant of this reaction k and the stoichiometric factors n , m_1 , m_2 and m_3 .

The fenarimol degradation follows a first order kinetic [51, 94]:

$$[Fm](t) = [Fm]_0 \cdot e^{-kt} \quad (3.1.13)$$

with the concentration of fenarimol in water $[Fm]$ and the starting concentration $[Fm]_0$. By measuring the concentration of fenarimol in water over the time it is possible to calculate the overall kinetic constant of the degradation k which is the sum:

$$k = k_c + k_0 \quad (3.1.14)$$

of the degradation by the catalyser k_c and the photolysis by UV-light k_0 . The kinetic constant of the chemical reaction k_c is determined for the different titanium dioxide systems [51,94].

DETERMINATION OF THE FENARIMOL CONCENTRATION

The determination of the fenarimol concentration at each measurement step is crucial to calculate the photocatalytic activity of a sample. The concentration of fenarimol in water is carried out by using high-performance-liquid-chromatography (HPLC). This liquid chromatography is based on the interaction between the different monomers in the sample solution and a stationary phase inside the experimental setup. The sample solution is mixed with a mobile phase and flows along the stationary phase. The monomers inside the sample solution are now separated and the flowing time for each monomer is depending on the interaction with the stationary phase due to capillary effects [99,100].

After that the flowing liquid is analysed by an UV-VIS-spectroscopy, because every monomer has different light absorption properties [98]. The exact composition of the sample solution can be determined by measuring the UV-adsorption over the time and the fenarimol concentration can be calculated at each time step of the photocatalytic measurement.

The sample solutions are taken out of the photocatalytic reactor and immediately analysed by a HPLC system. This is a Agilent Technologies 1220 LC Infinity system with UV detector. The liquid chromatography is carried out under the following conditions: LichroCART 125-4 column; Lichrospher 100 RP-18; $5\ \mu m$; eluent; acetonitrile 65%, MilliQ water 35 %; 1.0 ml/min flow; UV detection at 220 nm [51].

3.2 SYNTHESIS AND SAMPLE PREPARATION

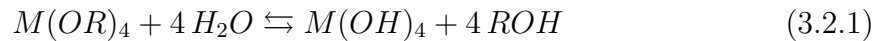
In this thesis the focus is on titanium dioxide nanopowders and nanostructured thin films. The thin film preparation is similar to the preparation of the titanium dioxide photocatalyst in the water purification reactor designed during this work [17]. Additionally, there are two different powders chosen. Firstly, the commercial Degussa P25 powder which will be the reference material and secondly, a powder series based on sol-gel-synthesis. This synthesis method is chosen because it is comparable to the thin film samples since they are both based on the same precursor [17, 59, 101].

All sample series will be heat treated at various temperatures in various atmospheres and with various external electrical fields.

3.2.1 POWDER SAMPLES

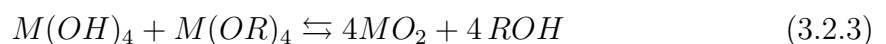
SOL-GEL-SYNTHESIS

The sol-gel-synthesis is a wet chemical method which is widely used in industries and science to synthesis inorganic nanostructures, because it proceeds under mild conditions and offers the possibility to create nanostructured powders, fibres or thin films [59, 60, 102]. Basically, it is the series of the hydrolysis and condensation of an organic metal-pre-cursor, resulting in a solid network of nanoparticles. That means this is a bottom-up synthesis method [60].



Equation 3.2.1 shows the beginning of the hydrolysis process where a organic metal-pre-cursor $M(OR)_4$, with M for metal and R for organic rest, reacts with water to a metal-hydroxide molecule $M(OH)_4$ and organic products ROH . The solid metal-hydroxides are dispersed in a solution of water and organic products. This dispersive solution is called **sol**. The solid particles have no interaction with each other which results in a stabilisation of the nanoparticles and avoid any aggregation or agglomeration [59, 103] of the particles. The metal-hydroxides are called homogeneous condensation cores and are important for the following condensation and poly-condensation process which will transform the sol into a gel.

In an ideal system the condensation leads to the formation of pure metal-oxide-particles MO_2 in water and organic products:



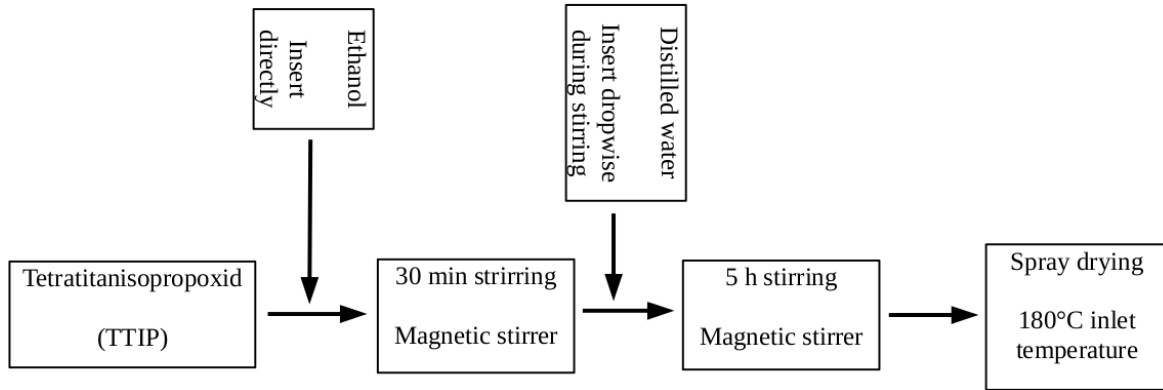


Figure 3.2.1: Flow chart of the sol-gel-synthesis of amorphous titanium dioxide powder.

In a real system monomers with hydroxide- and alkoxide-bondings are formed following equation 3.2.4:



with the monomer MOM and the alkoxide-bondings $(RO)_n$. Due to growth processes such as agglomeration or Ostwald-ripping polymer like chains and networks are formed inside the water. The type of growing can be influenced by the parameters of pH-value, synthesis temperature or water-to-pre-cursor-ratio. The high viscose mixture of solid particle networks and liquids is called **gel** [61, 103–105].

Out of this gel powders(drying), films(dip coating) or fibers(spining) can be produced depending on the further processes which shows the wide usage range of this synthesis method.

To produce nanostructured amorphous titanium dioxide powder which can be transformed to a single phase anatase powder the sol-gel-method is chosen. A flow chart of the detailed synthesis is given figure 3.2.1. As metal-pre-cursor tetratitanisopropoxid, TTIP or $Ti(OCH(CH_3)_2)_4$ was used. This pre-cursor is known for a preferred anatase crystallisation [59, 61, 106]. The reagent-ratios in *ml* are given in equation 3.2.5:

$$TTIP : H_2O : Ethanol = 5 : 50 : 200 \quad (3.2.5)$$

The then formed gel is dried by a spray drying process with a maximum temperature of $T_{max} = 180^\circ C$. The synthesis parameter are chosen with the motivation to produce uniform spherical particles [105, 106].

In this thesis powders synthesised by this very sol-gel-method will be label 'sol-gel-based powder'.

HEAT TREATMENT

Each powder system, sol-gel based powder and commercial Degussa P25 powder, are heat treated in air as well as in vacuum. The vacuum is characterised by a pressure of $p \approx 2.5 \cdot 10^{-5} \text{ mbar}$. Each powder samples are treated without an external electrical field and are annealed at their maximum temperature between 200 °C and 700 °C for 4 h. During the heat treatment the powders are placed in titanium foil crucibles within a stainless steel furnace with a copper cylinder for temperature homogenization [51]. As heaters, two halogen lamps (1 kW) were used, similar to the heaters in the resistivity setup.

The samples heat treated with an external electrical field are powders which are pressed to a pellet of a diameter of 1 cm by using a hydraulic press at room temperature. The pressure is approximately 50 kPa and it is applied for approximately 5 min [29]. The pellets are heated in various atmospheres with an external electrical field applied with a ramping rate during the heating process and the cooling process of $200 \frac{K}{h}$. Therefore, the overall treatment time of powders and pellets is comparable.

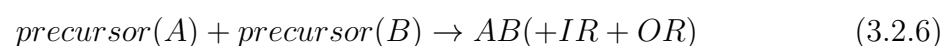
3.2.2 THIN FILM SAMPLES

The formation of uniform nanostructured thin films is of a high interest because it combines the properties of nanostructured powders with a long lasting static construction especially when it comes to photocatalytic applications [17, 107]. Although a comparison of thin films and powders with respect to their electrical or photocatalytic properties can help to distinguish between internal effects or external effects, such as pore- or surface-caused changes.

To prepare uniform thin films vapour deposition methods are widely used. During these processes atoms and molecules from a source are deposit on a substrate. Depending on how the gas molecules are provided a distinction is made between physical vapour deposition, PVD, or chemical vapour deposition, CVD. The first method is often preferred for pure metal thin film preparation while the CVD method is commonly used to prepare metaloxide or metalsulfide thin films [108].

COMPLEX-COMPOUND-CHEMICAL-VAPOUR-DEPOSITION

During chemical-vapour-deposition a chemical reaction inside the preparation chamber took place where the aimed metaloxide is one of the reaction products:



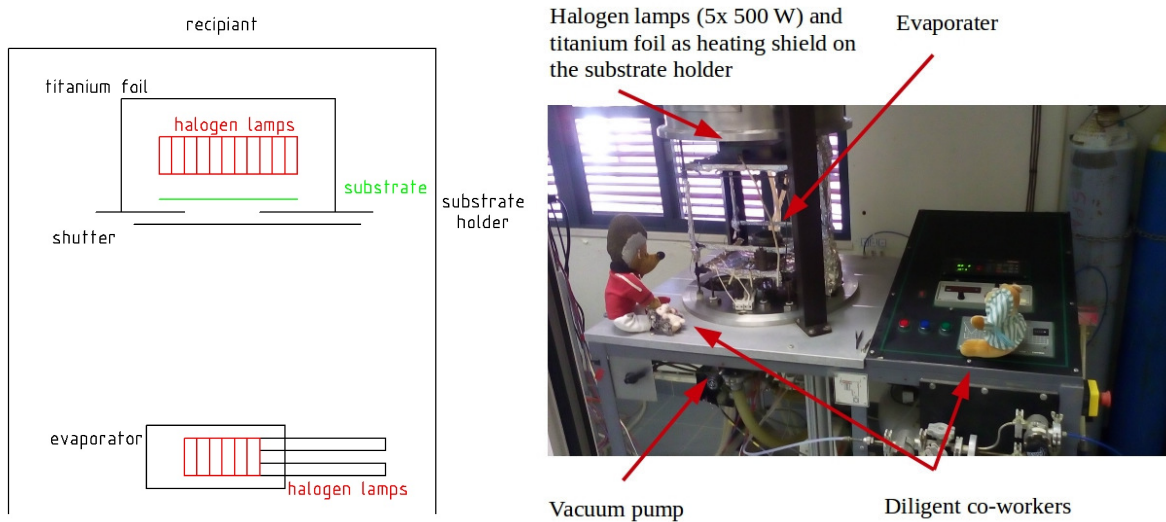
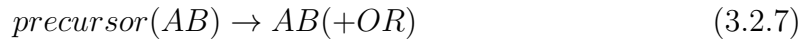


Figure 3.2.2: Schematic draw (left) and photography (right) of the used CC-CVD setup.

with a precursor for a metal A, a precursor for oxygen or sulphur B, an possible inorganic rest IR and a possible organic rest OR.

On one hand this require more than one precursor and on the other hand interfering secondary products can be present which will lead to a contamination of the metal-oxide thin film.

A possible solution for this problem is the complex-compound-chemical-vapour-deposition, CC-CVD:



with the complex-compound-precursor AB and a possible organic rest OR [108]. The advantage of this method is that the aimed metal oxide is already present inside one organic precursor. Inside the preparation chamber is no critical chemical reaction necessary. The precursor is evaporated which will lead to the elimination of organic rests and will left a pure metal oxide molecule flow which will be deposited on the substrate. Due to this advantage titanium dioxide thin films are prepared by CC-CVD method during this work. A schematic draw and a photography of the preparation chamber is shown in figure 3.2.2.

For the preparation of TiO_2 thin films, TTIP is used as precursor to be able to compare the thin films with the sol-gel-based powder. The precursor is filled inside the evaporator at the bottom of the chamber while the substrate is placed above the evaporator at the top of the chamber. The evaporator is connected with the cooling system. Before the thermal treatment of the precursor, the chamber is evacuated to a pressure of $p_{pre} \approx 1 \cdot 10^{-5} \text{ mbar}$ and the substrate is heated with halogen lamps(1 kW) up to a temperature of $T_{substrate} = 420^\circ\text{C}$ to ensure the crystallisation of anatase on the quartz glass substrate [17, 101, 107]. When the substrate temperature is reached

the chamber is flooded by an argon oxygen mixture of $\frac{Ar}{O_2} = \frac{100}{50}$ up to a pressure of $p_{dep} \approx 1 \cdot 10^{-1} mbar$. This argon oxygen atmosphere should provide enough oxygen to guarantee the formation of TiO_2 molecules and the burning of organic rests to avoid contamination of the film. Following the flooding of the chamber the evaporator is heated up to $T_{evaporator} = 50^\circ C$ and the substrate shutter is opened to start the chemical process. During this deposition process the pressure inside the chamber increase. When the value of p_{dep} is restored the precursor is completely evaporated and the deposition process is finished.

Chapter 4

Results

4.1 PHOTOCATALYTIC ACTIVITY

The overall photocatalytic constants of the Degussa P25 powder series annealed in vacuum and in air are shown in figure 4.1.1.

The vacuum curve, red, begins with a significant increase of the photocatalytic degradation of fenarimol in water from $3.02 h^{-1}$ for the initial powder up to $5.28 h^{-1}$ for powders annealed at 400°C . After that a local minimum at 600°C is reached, followed by a short increase at 620°C which is below the initial powder. At higher temperatures a strong drop down to $0.39 h^{-1}$ which is very close to the natural degradation rate of $0.26 h^{-1}$, is observed.

In contrary, the samples annealed in air, blue curve, show a significant decrease at lower temperatures, resulting in a minimum between 200°C and 400°C . The curve itself has two local maxima at 550°C and 620°C , while the strong drop down occur at 670°C which is 20 K higher compared to the vacuum samples.

There are several points that need to be investigated. Firstly, the gap at 400°C , where a maximum is reached in vacuum and a local minimum occurs in air. Secondly, the material properties at 620°C , because at this point always a local maximum can be observed. And thirdly, the temperature of the photocatalytic drop down when a value in the range of the natural decomposition is reached, because this temperature is about 20 K higher in air than in vacuum.

The photocatalytic efficiency can be influenced by the three major parameters: band gap energy, surface area and charge carrier transfer, as it is explained in section 2.3. While a change in band gap energy can be neglected, the phase composition of the Degussa P25 powders annealed at higher temperatures needs to be carefully studied. Rutile is considered as a non active phase compared to anatase [26, 51] which is also demonstrated by the photocatalytic kinetic constant at 700°C in vacuum. This powder is pure rutile powder and it has the lowest kinetic constant close to pure photolysis. The higher temperature for the drop down of the kinetic constant can be explained by

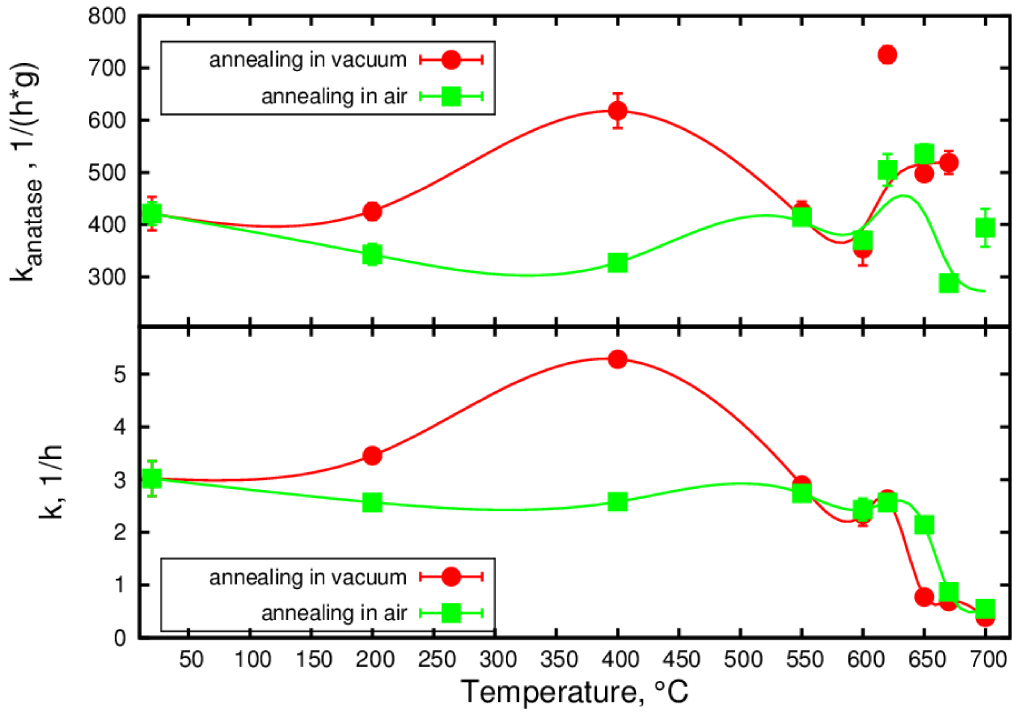


Figure 4.1.1: Overall photocatalytic kinetic constant of Degussa P25 powder series annealed in vacuum and air (bottom) and photocatalytic kinetic constant of the anatase phase of Degussa P25 powder series annealed in vacuum and air (top), modified from [51].

the strong increase of the rutile fraction inside the Degussa P25 composition, showed in table 4.7.1. The drop down is connected with a rutile fraction of more than 75 %. By neglecting the amount of the rutile fraction it is possible to calculate the photocatalytic kinetic constant of the anatase phase k_A with the following equation, considering that there is no synergetic effect between anatase and rutile [51, 63]:

$$k_A = \frac{k - (m_R \cdot k_R + k_0)}{m_A} \quad (4.1.1)$$

with the kinetic constant of the rutile phase k_R , the kinetic constant of the photolysis by UV-light k_D and the mass of the titanium dioxide phases calculated by XRD m_A and m_R .

The results are shown in figure 4.1.1.

The vacuum curve shows again two maxima at 400 °C and 620 °C with a minimum at 600 °C. But compared to the overall kinetic constant, there is no drop down to the range of the photolysis, at higher temperatures a value of around 500 $(h \cdot g)^{-1}$ is stabilized which is in the range of the initial not annealed anatase phase inside the Degussa P25 powder.

The air treated powder series show a similar behaviour. The minima at 400 °C and

600 °C also occur like the maxima at 620 °C. The increase up to 650 °C and $536 (h \cdot g)^{-1}$ is not significant. At high temperatures, the value of $394 (h \cdot g)^{-1}$ is very close to the initial value of $421 (h \cdot g)^{-1}$ but a short dip at 670 °C is observed.

The first and second observation at the overall kinetic constant, the gap at 400 °C between the vacuum treated powder and the air treated powder and the maxima at 620 °C are still established. So, they are independent of the anatase-to-rutile-ratio and they have to be connected to the surface area and the charge carrier transport inside the material. The drop downs at higher temperatures are in strong dependency of the rutile fraction. This is the reason why this observation is neutralized and values close to the initial anatase phase of the untreated powder are reached.

Further discussions to the gap at 400 °C and the maxima at 620 °C are in section 4.2.

4.2 SURFACE AREA AND POROSITY

The results of the nitrogen adsorption will be distinguished into results of the shape of the particles and shape of the pores by a quantitative analysis and results of the surface area and the pore size distribution by a qualitative analysis.

QUALITATIVE ANALYSIS

Figure 4.2.1 shows the typical nitrogen adsorption-desorption isotherms for Degussa P25 titanium dioxide powder samples annealed in different atmospheres compared to Degussa P25 pellet samples. The powders are showing a type II isotherm with a H3-hysteresis. In contrary, the pellet samples are showing a type IV isotherm with a characteristic type H2-hysteresis [89]. Both isotherms include a small slope from the B-point, at $\frac{p}{p_0} = 0.05$, up to $\frac{p}{p_0} = 0.60$ which is characteristic for meso-porous material. The slope in the adsorption branch of the pellet samples is stronger pronounced than in the adsorption branch of the heat treated Degussa P25 powders. Following $\frac{p}{p_0} = 0.60$ the slope drastically increases until the adsorbed quantity reaches a maximum value at $\frac{p}{p_0} = 0.94$. The maximum value of the adsorbed nitrogen gas is smaller than for the powder samples, which shows that the macro-pore volume between the powder particles is larger than the external surface area of the pellet [50, 87].

During the desorption, a quantity of adsorbed nitrogen gas molecules stays constant on the surface of the pellet samples until a strong decrease at $\frac{p}{p_0} = 0.82$ is observed, followed by a slightly decrease until the formed hysteresis is closed at $\frac{p}{p_0} = 0.58$. The desorption branch of the powder samples decreases directly with the decreasing of the surrounding pressure forming a slim hysteresis which is closed at $\frac{p}{p_0} \approx 0.80$. This indicates that there are open macro- and meso-pores inside the pellet which is different to

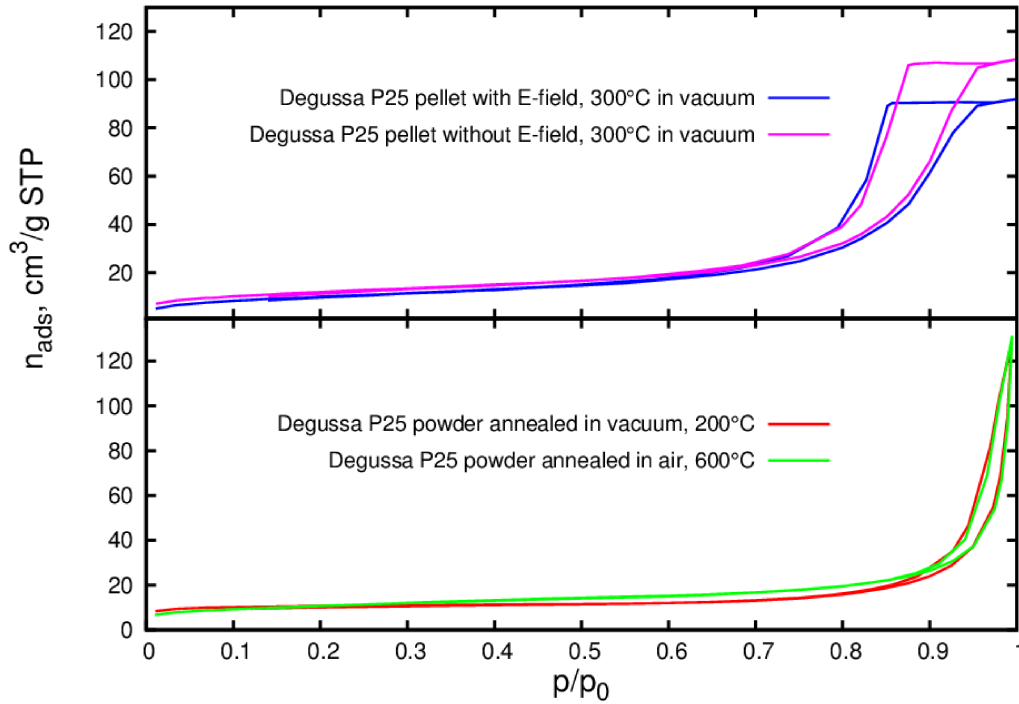


Figure 4.2.1: Examples of typically nitrogen adsorption isotherms of Degussa P25 powder samples annealed in different atmospheres (bottom) and examples of typically nitrogen adsorption isotherms of Degussa P25 pellet samples treated in vacuum with and without an applied electrical field (top), modified from [42].

the closed meso-porous structure inside the powder samples.

The formed H2-hysteresis implies that the Degussa P25 pellets are consisting of aggregated spheroidal particles forming cylindrical channels. The pores are in non-uniform size and shape and they vary from cylindrical shape to ink-bottled shape. The H3-hysteresis of the powders is characteristic for plate like shaped particles forming slit shaped pores of non-uniform size. [50].

It could be assumed that this difference in morphology between Degussa P25 pellets and powders is caused by the cold pressing during the pellet formation which induces a mechanical stress to the material. This stress will lead to changes in the shape and size of particles and pores. In contrary, the morphology of sol-gel based pellets derived by nitrogen adsorption isotherm is significantly different after the heat treatment in vacuum despite they are cold pressed similar like the Degussa P25 pellets. This can be explained by structural changes in the mild temperature region. While the initial sol-gel based pellet is highly amorphous and containing organic rests from the synthesis, during heat treatment in vacuum the evaporation of this organic rests and the amorphous to anatase phase transition took place. The latter leads to more spherical particles and weakens the mechanical stress induced by the cold pressing procedure. This leads to the more powder like morphology. In contrary, during the treatment of

Degussa P25 pellets, a structure containing two crystallite phases, only aggregation took place in mild temperature regime and this process benefits from mechanical induced stress.

To determine the influence of an applied electrical field on the Degussa P25 pellet samples, a Degussa P25 pellet after the resistivity measurement and its satellite pellet (without electrical field) is studied. The satellite pellet was installed in the copper furnace next to the measured sample, so it was treated in the exact same way except that there was no electrical field applied.

Figure 4.2.1 shows the results of the nitrogen adsorption experiments for these Degussa P25 pellets. They both showed the same isotherm type II and hysteresis type H2 which is typical for all Degussa P25 pellet samples [89]. The satellite sample shows a slightly higher amount of nitrogen gas adsorbed than the sample with an electrical field applied. Which shows that the surface area should be larger for the satellite sample than for the other one. From $\frac{p}{p_0} = 0.01$ to $\frac{p}{p_0} = 0.60$, the isotherms are parallel and show the exact same behaviour. After this the quantity adsorbed at the surface of the satellite sample rises stronger than the one of the sample with electrical field leading to a higher maximum value. The satellite sample has a larger pore volume compared to the other sample. Another difference is that the hysteresis of the satellite sample is slimmer than the hysteresis of the sample with an electrical field applied. That implies a more uniform shape and size of the pores of the satellite pellet compared to the other pellet [89]. The smaller surface area, the lower pore volume and the less uniform size and shape of the pores of the sample with an electrical field applied indicate that the aggregation of the particles to is stronger than in the satellite. Applying an electrical field in vacuum favours the formation of covalent bonds between titanium dioxide particles at mild temperatures. This process is probably localised on the conducting path of the electron current. Hence, there are positions inside the sample where a formation of a covalent bond has a higher possibility which explains the less uniform size and shape of the pores inside the material compared to the sample without an electrical field applied.

QUANTITATIVE ANALYSIS

The measured samples are analysed using BET-method to determine the specific surface area of different treated powders and pellets and using BJH-method to determine the pore size distribution of this titania systems. The quantitative analysis is crucial to understand the surface changing processes during mild temperature treatments in different atmospheres as well as with or without an electrical field applied. Furthermore it made a discussion of the influence of the surface area on the photocatalytic activity accessible [29, 51].

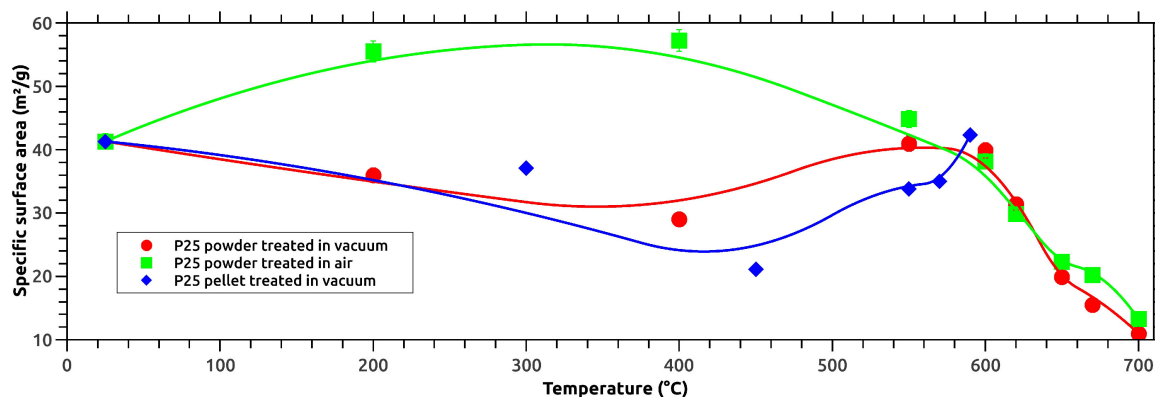


Figure 4.2.2: Specific surface area of Degussa P25 powders and pellets treated at various temperatures and various atmospheres, modified from [42, 51]. The errors are numerical errors from BET- and BJH-calculations and are in the range of the size of the symbols.

Firstly, the Degussa P25 powders treated in air and vacuum for 4 h are analysed. These are the titanium dioxide powders, where their photocatalytic activity is already discussed in figure 4.1.1. The results of the specific surface area analysis is presented in figure 4.2.2. Like for the photocatalytic activity a gap between the different atmospheres with its maximum spread at 400 °C and a neutralisation at 550 °C is observable in this measurement, but in contrary to the overall photocatalytic constant the powder treated in vacuum shows the decrease of specific surface area down to a minimum of $29.0 \frac{m^2}{g}$ at 400 °C while the powder treated in air shows a increase of specific surface area up to maximum of $57.3 \frac{m^2}{g}$ at 400 °C. This means that during heat treatment in air a strong gain of surface area took place. There are two processes which favourable this growth. Firstly, the exothermic burning of water and organics adsorbed inside the material in oxygen rich atmosphere which leads to a pore formation and secondly, the aggregation of particles [48, 49, 51].

The treatment in vacuum under mild conditions, below the anatase to rutile phase transition temperature, leads to a significant loss of surface area. On one hand, this is due to the endothermic evaporation of water and organics adsorbed inside the material in oxygen poor atmosphere where the pore formation is not as strong as during burning processes. And on the other hand, in vacuum the aggregation of grains is preferred instead of particle agglomeration following a loss of surface area [51]. XRD results show that under this mild conditions, no crystallite growth can be detected. So, this surface losing process can be neglected for powders heat treated up 400 °C in both atmospheres.

At 550 °C in both atmospheres the surface area changes are neutralised and the specific surface area is restored at a value of $41.0 \frac{m^2}{g}$ which is nearly the value of the original untreated Degussa P25 powder. This means that morphology changes during mild

temperature treatment are lost with the beginning of the phase transition and the start of crystallite growth at 550 °C leading to a loss in specific surface area [67, 109]. The formed particles in air are growing and pores are closed due to the crystallite growth and in vacuum the formed grains are destroyed because the phase transitions from anatase to rutile start at lattice defect points. The covalent bonds broke and the new pores are formed leading to a significant strong gain in specific surface area [51]. During treatment under high temperature conditions, above 600 °C, the specific surface area decreases independently of the surrounding atmosphere to a minimum due to a strong crystallite growth and a high rutile fraction formation. Both processes cause an high loss in pore volume and in surface area.

During the resistivity measurements the white titanium dioxide Degussa P25 pellets are turning either black in high vacuum ($p \approx 6 \cdot 10^{-6} \text{ mbar}$) or getting a black surface and a blue coloured bulk in slightly lower vacuum ($p \approx 1 \cdot 10^{-4} \text{ mbar}$). The specific surface area of these now black titania called samples are analysed and presented in figure 4.2.2, blue curve, and in table 4.2.1.

The Degussa P25 pellets treated in mild temperature range in vacuum with an electrical field applied showing in principle a similar behaviour like the Degussa P25 powders treated in vacuum. The specific surface is decreasing slightly from the untreated pellet to a pellet treated at 300 °C followed by a minimum at 450 °C. The results shows that the agglomeration of grains significantly rises at temperatures above 300 °C and is strengthened with applying an electrical field. It is possible that the electron flow inside the material induced by the electrical current through the titanium dioxide pellet improves the possibility of the formation of short ranged strong chemical bonds such as covalent or ionic bonds due to a reduction of the titanium atoms [29, 110].

At temperatures close to the phase transition temperature, the surface area increases significantly because of pore closing processes. The original specific surface area is again restored at 590 °C with $42.3 \frac{\text{m}^2}{\text{g}}$ which shows that the phase transition starts again at the lattice defects induced by reduction of titanium atoms and neutralises surface area losses due to agglomeration. Overall, the surface area of the pellets follows the same trend like the Degussa P25 powders, but the agglomeration of grains is stronger pronounced with a electrical field applied.

As last step of the morphology analysis of different titania powder systems the pore size distribution of the samples is determined by the BJH-method. The results of the pore volume shows that the Degussa P25 powders includes a higher pore volume than the Degussa P25 pellet samples. This is caused by the different sample shape and the mechanical induced stress due to the pressing of the pellets.

A detailed comparison between pellets and powders is presented in figure 4.2.3. On one hand, it is observable that pressing Degussa P25 and applying an electrical field during heat treatment in vacuum leads to a more dominant meso-porous structure than

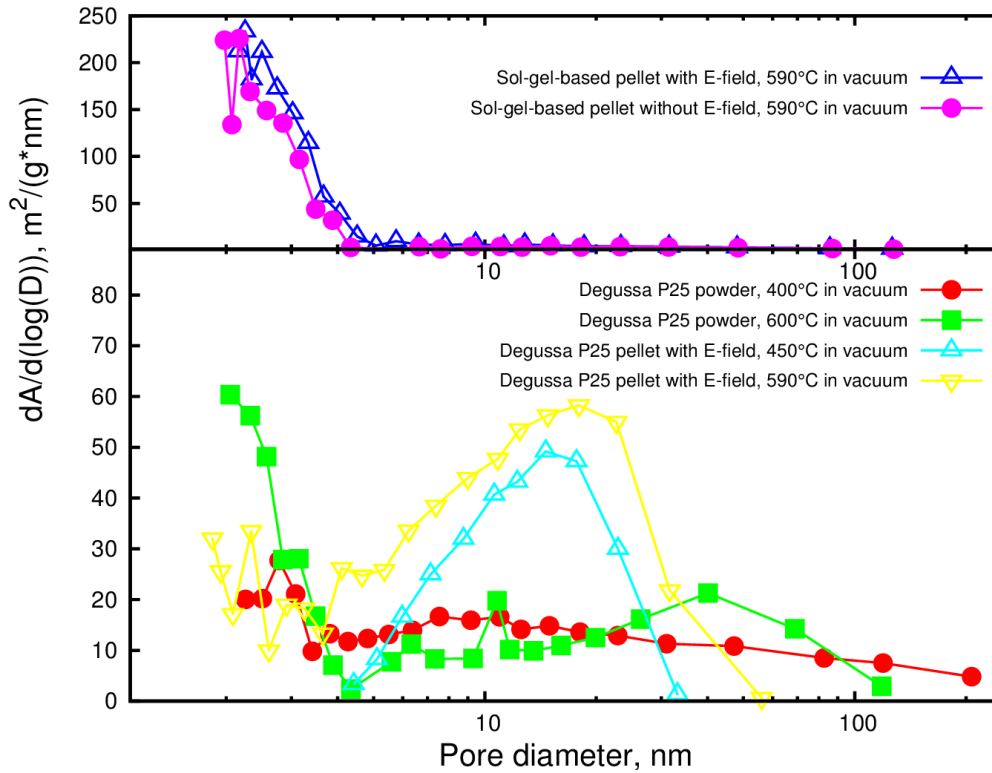


Figure 4.2.3: Pore size distribution of selected Degussa P25 powders treated in vacuum and air and Degussa P25 pellets treated in vacuum with an electrical field applied (bottom). Pore size distribution of sol-gel based pellets treated in vacuum with and without an electrical field applied (top), modified from [42, 51].

the simple heat treatment in vacuum of the pure unpressed powder. This supports the assumptions that with an electrical field applied the material enhance the grain formation in this samples and leading to a loss of micro-pores but gain meso-pores. On the other hand, it is shown that in mild temperature regime no micro-pores with a diameter smaller than 2 nm are detectable because of strong agglomeration, while in phase transition temperature range smallest micro-pores can be observed for both samples. This is caused by the starting anatase to rutile phase transition, which is located close to lattice defects and so the agglomeration is partly destroyed and micro-pores are formed [51].

The difference between the sol-gel-based pellets and the Degussa P25 pellet at the point of neutralisation, 590 °C, is shown in figure 4.2.3. While the Degussa P25 based pellet includes a wide range of pores with diameters from 2 nm up to 50 nm, the sol-gel-based pellets are dominated by micro-pores. During the heating the grain formation process in the sol-gel-based samples is suppressed by the amorphous to anatase crystallisation [67]. Which caused the more uniform pore size distribution and the lower pore volume despite the larger specific surface area compared to Degussa P25 pellets. The measurement of the sol-gel based samples also shows that a slightly higher amount of pores is present when an electrical field is applied during material manipulation, while

the specific surface area is lower. This could indicate a structural difference, such as a second crystalline phase, which influences the morphology significantly.

Nevertheless, the results of the specific surface area analysis and the pore size distribution are consistent with the qualitative analysis of the nitrogen adsorption isotherms.

Table 4.2.1: Calculated results of specific surface area and pore volume analysis of different titanium dioxide systems. The errors are numerical errors from BET- and BJH-calculations [42, 51].

			T / °C	E-field	surface area / $\frac{m^2}{g}$	pore volume / $\frac{cm^3}{g}$		
powder	P25	air	25	no	41.3 ± 1.3	0.179 ± 0.007		
			200	no	55.5 ± 1.7	0.280 ± 0.010		
			400	no	57.2 ± 1.8	0.289 ± 0.011		
			550	no	44.9 ± 1.4	0.214 ± 0.008		
			600	no	38.2 ± 1.2	0.201 ± 0.008		
			620	no	29.8 ± 0.9	0.169 ± 0.006		
			650	no	22.3 ± 0.7	0.125 ± 0.005		
			670	no	20.3 ± 0.7	0.097 ± 0.004		
			700	no	13.3 ± 0.4	0.058 ± 0.004		
	vacuum	200	no	36.0 ± 1.1	0.189 ± 0.007			
		400	no	29.0 ± 0.9	0.231 ± 0.009			
		550	no	41.0 ± 1.3	0.196 ± 0.007			
		600	no	39.9 ± 1.2	0.204 ± 0.008			
		620	no	31.4 ± 1.0	0.176 ± 0.007			
		650	no	19.9 ± 0.6	0.093 ± 0.004			
		670	no	15.5 ± 0.5	0.073 ± 0.003			
		700	no	11.0 ± 0.4	0.035 ± 0.002			
		pellet	P25	vacuum	300	yes	37.1 ± 1.5	0.143 ± 0.007
					300	no	43.3 ± 1.8	0.169 ± 0.007
450	yes				21.1 ± 0.9	0.111 ± 0.005		
550	yes				33.8 ± 1.4	0.153 ± 0.006		
570	no				35.0 ± 1.4	0.162 ± 0.007		
590	yes				42.3 ± 1.7	0.171 ± 0.007		
Sol-gel	vacuum				590	yes	49.5 ± 2.0	0.087 ± 0.004
		590	no	56.5 ± 2.3	0.073 ± 0.003			

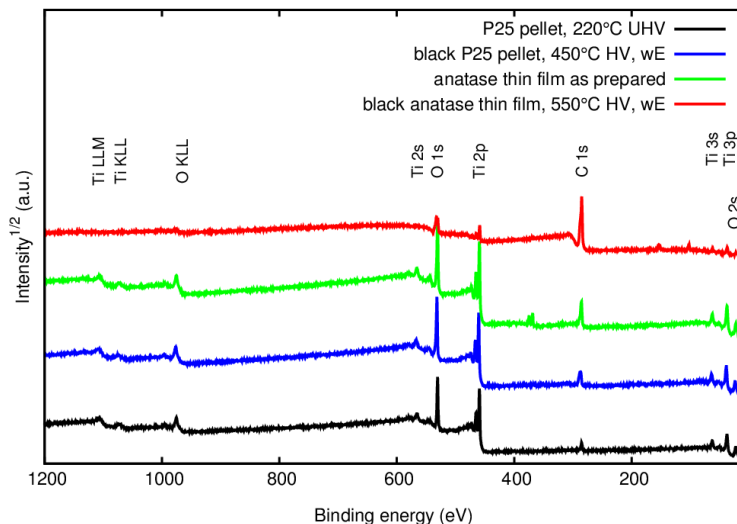


Figure 4.3.1: Survey measurements of Degussa P25 pellets and anatase thin films with and without an applied electrical field during heat treatment in vacuum.

4.3 X-RAY PHOTOELECTRON SPECTROSCOPY

X-ray photoelectron spectroscopy is used to analyse the surfaces of the Degussa P25 pellets as well as the anatase thin films prepared by CVD. Firstly, the chemical composition of the as prepared samples and the black samples, titania systems treated in vacuum with an electrical field applied, are investigated to study whether silver diffusion is the basis of the black colour. Secondly, the titanium defects close to the surface are analysed by measuring detailed spectra of the Ti 2p-peak and the O 1s-peak.

4.3.1 CHEMICAL COMPOSITION

Table 4.3.1 presents the calculated results for all measured titania systems using CasaXPS [111] and fityk [112] as fitting routines. The chemical composition of the black titania samples is of an high interest to study the colour centres which will lead to the drastic change. In figure 4.3.1 the survey measurements of a black samples and their references are shown. The survey of the black pellet is measured in centre position after carefully scratching of the silver electrode. The survey of the black thin film is measured between two electrodes.

In Degussa P25 pellets only oxygen, carbon and titanium is detected. The carbon value in the black sample is significantly higher than in the original powder but the amount is not big enough to explain the change in colour. The Degussa P25 pellet sample treated in the preparation chamber at 350 °C contains more carbon atoms on the surface than the black pellet but it is still white. The higher carbon amount in the black sample could indicate a better adhesion of organic material on the surface of the titanium dioxide.

The anatase thin film on quartz glass is the only sample in this work, where a charging of the titanium dioxide during XPS-measurements is observed. To avoid the use of an electron gun, silver glue is used to bring electrical contacts on the sample and the survey is measured close to the silver spot. This explains the silver edge at 378 eV in this sample, green curve, which is the only new species compared to Degussa P25 [91]. So the measured area was too close to the silver glue added to avoid charging effects during the measurement. Nevertheless, in the black anatase film there is no silver detectable. Proving that there is no silver diffusion during heat treatment in vacuum with an electrical field applied. Although, this sample contains the highest amount of carbon species of every measured samples. Showing that there was such a strong adsorption of molecules on the surface that the dominant carbon species avoid a useful defect analysis. It is not clear whether the carbon species are adsorbed during the heat treatment under mild temperature conditions in high vacuum or they are adsorbed after exposing the sample to air and storing the sample in air filled boxes.

The quasi-in-situ treated anatase thin films deposited on Si-B-substrate are not showing any anomalies concerning the chemical composition. As it can be seen in table 4.3.1 the carbon species stays nearly constant at low temperatures and decreases for samples treated at temperatures above 250 °C. The titanium content stays nearly constant and the oxygen content is slightly increasing with higher temperature. This could be correlated with cleaning the surface from carbon species and a crystallisation process of amorphous structures at temperatures above 400 °C .

In contrast, in the Degussa P25 pellet samples measured with quasi-in-situ method a anomaly at 350 °C is observed with a significant increase of the carbon species. The temperature corresponds to strong morphology change in Degussa P25 pellets, observed in the analysis of the surface area. The decrease in porous structure could lead to a release of absorbed organic rests from the centre of the pellet to the surface, but this process is not finished yet. Resulting in carbon species still adsorbed in sub-surface bulk layers or adsorbed directly on the surface due to a better adhesion ability due to higher titanium defect states [33, 113, 114].

4.3.2 SURFACE DEFECT ANALYSIS

The surface defect analysis is done by analysing the Ti 2p_{3/2}-peak and the O 1s inside the detailed spectrum of each sample. The experimental results are used in a fitting procedure using CasaXPS-program [111] and fityk [112].

The fitting procedure is analogous to [29] where the Ti³⁺-states are detected in the lower energy shoulder of the Ti 2p-peak. The titanium species are fitted using a pseudo-Voigt line shape in product form. As fixed fitting parameters the binding energy of the Ti⁴⁺-

and the Ti^{4+} -states and the full-width-half-maximum (fwhm) are chosen as:

$$BE_{Ti^{3+},centre} = 457.8 \text{ eV} (\pm 0.2 \text{ eV}) \quad fwhm_{Ti^{3+}} = 0.95 \text{ eV} (\pm 0.02 \text{ eV})$$

$$BE_{Ti^{4+},centre} = 459.4 \text{ eV} (\pm 0.2 \text{ eV}) \quad fwhm_{Ti^{4+}} = 0.95 \text{ eV} (\pm 0.02 \text{ eV})$$

Additionally, the fixed parameters for fitting the oxygen O 1s-peak are chosen as:

$$BE_{O_{structural},centre} = 530.5 \text{ eV} (\pm 0.1 \text{ eV}) \quad fwhm_{O_{structural}} = 1.08 \text{ eV} (\pm 0.02 \text{ eV})$$

The amount of Ti^{3+} defect sites are estimated by the calculating the area ratios of the fitted titanium species using:

$$Ti^{3+}(\%) = 100 \cdot \frac{A_{Ti^{3+}}}{A_{Ti^{3+}} + A_{Ti^{4+}}} \quad (4.3.1)$$

with $A_{Ti^{3+}}, A_{Ti^{4+}}$ are the calculated areas of the titanium species from the fitting procedure of the Ti 2p-peak.

The amount of oxygen vacancies are estimated by the ratio of structural oxygen to titanium:

$$\frac{O_{structural}}{Ti} = \frac{A_O \cdot \sigma_{Ti}}{\sigma_{Ti} \cdot A_{Ti}} \cdot O_{structural} \quad (4.3.2)$$

with the area of the oxygen O 1s peak A_O and the area of the titanium Ti 2p peak A_{Ti} in the survey measurement of the sample, the sensitivity factors σ_{Ti} and σ_O [91] and the relative amount of the structural oxygen, $O_{structural}$, in the O 1s band. The value is underestimated because there is no distinction between structural and interstitial titanium species [29].

The results in table 4.3.1 show that the defect structure in anatase thin-films on silicon-substrates is not changing significantly during the quasi-in-situ treatment. This can be explained by a highly stoichiometric synthesis process in argon-oxygen atmosphere. Furthermore, the missing of a high amount of line defects exceeds the formation energy for oxygen defects and the pure anatase phase prefers the formation of bulk defects [33, 44, 115]. The information depth of the XPS-setup is not deep enough to observe these bulk defects. As a result the analysis is focussed on the Degussa P25 samples.

DEGUSSA P25 PELLETS AND POWDERS

Figure 4.3.2 presents the results from the defect structure calculations based on the XPS-measurements. It shows a slightly increase of Ti^{3+} -sites and a slightly decrease of oxygen vacancies with increasing temperature.

The first decrease in the structural oxygen between room temperature and 100 °C can be neglected because it is correlated with a cleaning process of the surface. The

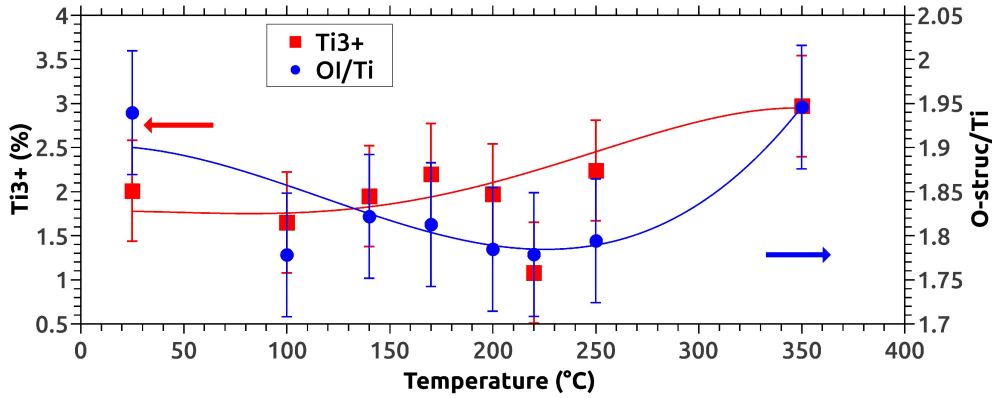


Figure 4.3.2: Calculated results from the XPS-analysis of Degussa P25 pellets quasi-in-situ treated in ultra-high vacuum ($p \approx 1 \cdot 10^{-9} \text{ mbar}$) for 2 h, presenting the Ti^{3+} percentage and the $\text{O}_{\text{structural}}/\text{Ti}$ relation, modified from [29].

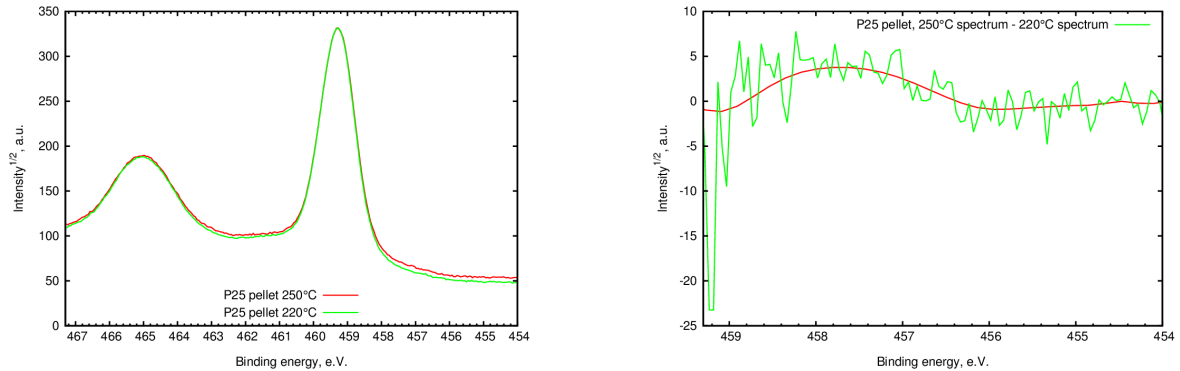


Figure 4.3.3: XPS detailed spectra of Ti 2p-peaks (left) of a Degussa P25 pellet during quasi-in-situ heat treatment for two different temperatures and the difference of these Ti 2p-spectras (right). The spectra are normalised in intensity and shifted in the binding energy achieve the difference plot [29].

information depth is increased and the organic layers with a various oxygen states is removed. After that, the structural oxygen stays constant until a increase of structural oxygen is measured between 250 °C and 350 °C. This means a decrease of lattice oxygen defects close to the surface at elevated temperatures is caused by oxygen diffusion processes and defect redistribution in this mild temperature range [29, 116].

The Ti^{3+} -states shows a steady increase with an anomaly at 220 °C. At this temperature the calculated Ti^{3+} -states are significantly lower. A further investigation is done to proof the significant loss of Ti^{3+} -states. A difference plot between the samples treated at 220 °C and 250 °C is shown in figure 4.3.3. The original spectra of the samples is shown and is subtracted from each other [117].

As a result, a peak is observed at a binding energy of 457.8 eV which is the binding energy of Ti^{3+} -states [117–119]. This proofs that more Ti^{3+} -sites are present in the sample treated at 250 °C compared to the sample treated at 220 °C and the observed minimum is a real material effect.

Table 4.3.1: Results of the XPS analysis for selected powders and for quasi-in-situ experiments of different titanium dioxide systems, based on Degussa P25 or anatase thin film (A-tf). The samples are either treated in air, in high vacuum (HV, $p \approx 1 \cdot 10^{-5} \text{ mbar}$) or in ultra high vacuum (UHV, $p \approx 1 \cdot 10^{-9} \text{ mbar}$).

		T, °C	Ti,%	O,%	C,%	O/Ti	C/Ti	O-struct,%	O-struct/Ti	Ti3+,%
P25 powder	original	25	30.51	62.75	6.73	2.06	0.22	85.08	1.75	2.12
		200	28.27	64.90	6.83	2.30	0.24	86.87	1.99	2.14
		400	28.02	64.94	7.04	2.32	0.25	86.72	2.01	2.33
	air, 4h	600	20.09	74.09	5.81	3.69	0.29	87.20	3.22	1.73
		400	29.29	64.78	6.97	2.21	0.24	86.34	1.91	1.84
P25 pellet	black	450	23.78	57.41	18.81	2.41	0.79	84.10	2.03	1.41
		25	28.96	64.82	6.22	2.24	0.22	86.59	1.94	2.01
	In-situ UHV, 2h	100	30.32	62.39	6.46	2.06	0.21	86.32	1.78	1.65
		140	29.63	62.9	7.47	2.12	0.25	85.94	1.82	1.95
		170	29.84	62.48	7.69	2.09	0.26	86.73	1.81	2.20
		200	30.88	63.08	6.04	2.04	0.20	87.48	1.78	1.97
		220	30.46	61.70	7.84	2.03	0.26	87.62	1.78	1.08
		250	29.86	61.64	8.50	2.06	0.29	87.10	1.79	2.25
		350	23.54	51.33	25.13	2.18	1.07	89.26	1.95	2.97
A-tf on glass	original	25	22.83	55.17	22.00	2.42	0.96	81.39	1.97	2.83
	black	550	2.67	15.24	82.08	5.71	30.74	39.51	2.26	0.68
A-tf on Si-B	In-situ UHV, 2h	25	22.39	68.89	8.72	3.08	0.39	85.56	2.63	2.70
		200	21.99	68.97	9.04	3.14	0.41	86.07	2.70	3.27
		250	22.01	69.31	8.69	3.15	0.39	85.64	2.70	2.42
		300	22.85	70.27	6.92	3.08	0.30	85.77	2.64	2.97
		350	22.64	70.94	6.42	3.13	0.28	86.86	2.72	2.57
		450	22.69	73.02	4.28	3.22	0.19	81.34	2.62	2.95

The results of the black titanium dioxide samples, especially, their defective structure is discussed in more detail in chapter 5.4.

4.4 EDX - CHEMICAL COMPOSITION

The EDX-analysis is done to determine the chemical composition of the black titanium dioxide pellets. The advantage compared to the XPS-method is a information depth which is deeper than the first atomic layers.

The silver electrode is removed and the analysed area is chosen on the spot of the former electrode. It is not necessary to coat the black pellets with a conducting layer, because there is no charging effect observable during the experiment which is in contrary to original Degussa P25 titanium dioxide powders.

The EDX-spectrum of the black titanium dioxide pellet, figure 4.4.1, shows the presence of titanium, oxygen and carbon atoms. There are no further foreigner atoms detectable, neither silver nor copper. This proves that there is no significant diffusion of silver atoms from the electrode into the titanium dioxide lattice, which is consistent with the XPS-analysis.

The atom percentage of every included element is given in table 4.4. It shows there is only a minority of carbon present compared to oxygen and titanium. It could be assumed that the carbon atoms detected are organic substances adsorbed to the surface

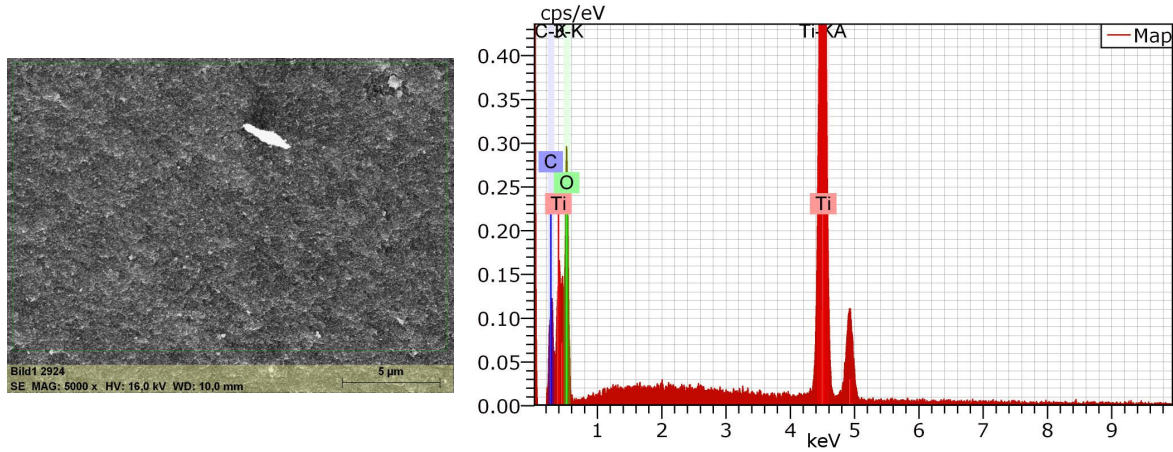


Figure 4.4.1: SEM image of the analysed area(left) and EDX spectrum(right) of the black titanium dioxide pellet.

of the titanium dioxide after getting in contact with air. So, the significant change in conductivity as well as the change in colour from white to black is not connected with a drastically increase of carbon inside the titanium dioxide lattice. Furthermore, it is not connected with a possible formation of titanium carbonates. Both is consistent with XPS and XRD results.

Table 4.4.1: Results from the EDX measurements of the black titanium dioxide pellet calcinated in vacuum with an applied external field normal to the surface at 450°C. The errors are absolute errors.

	Ti	O	C
Atom-%	35.16 ± 1.9	59.04 ± 27.1	4.98 ± 0.4

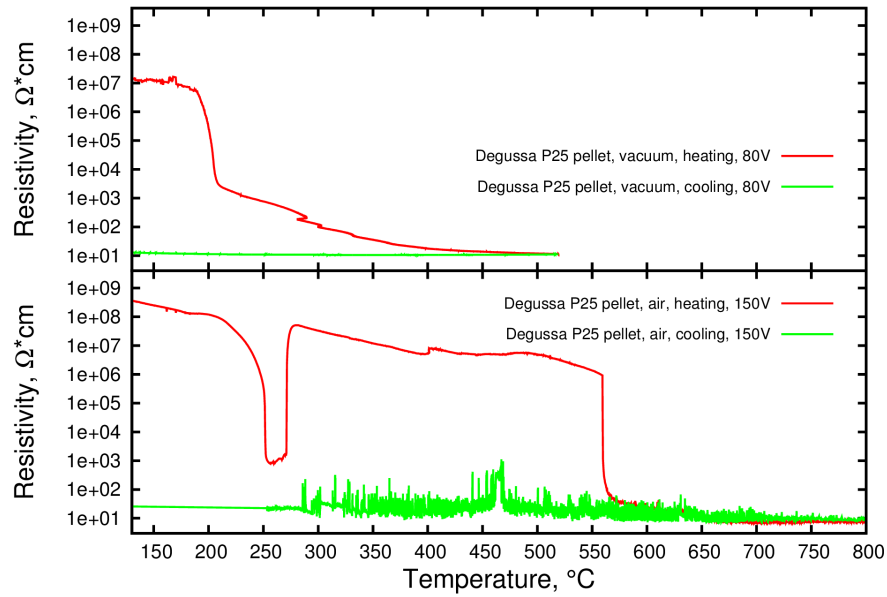


Figure 4.5.1: Measurement of the resistivity over temperature of Degussa P25 titanium dioxide pellet samples in vacuum and in air. The reference resistance is $R_R = 1 M\Omega$. Modified from [29, 42].

4.5 RESISTIVITY

Characterisation of the ability of a titanium dioxide system to transfer free charge carriers through the material is done by using resistivity measurements with a direct current setup. The measurements will be performed in the mild temperature range, below the anatase to rutile phase transition temperature of 600°C in air and in vacuum.

In the following section the different titania systems will be distinguished in powder pellets which will include a high amount of pores and in thin film systems which will be interpreted as quasi fully densified material. This divide is important to analyse whether a change in the resistivity is due to internal effects, such as structural or defective changes, or due to external effects such as leaking currents through pores.

4.5.1 P25 - POWDER

As reference material Degussa P25 titanium dioxide powder is analysed. The results for Degussa P25 pellets in vacuum, top, and in air, bottom, measured with a high applied voltage are shown in figure 4.5.1.

The heating of the first sample in vacuum, red curve, starts with a high resistivity of several $M\Omega\cdot\text{cm}$ at room temperature. The influence of water and absorbed organics

can be seen as noise in the beginning of the measurement. Overall the Degussa P25 pellet is in an insulating state. At 200 °C there is a sharp break down effect where the resistivity decreases immediately about 5 orders of magnitude.

Following this break down effect a slower decrease of the resistivity is observable from 210 °C up to 420 °C. The Degussa P25 pellet changes its nature from an insulating mode to a conductive mode with a resistivity of several hundred Ohms. The reason could be a possible leaking current through the pores or a change in conductive mode due to a high defective structure [39, 116, 120]. This resistive switching effect is known for high defective SrTiO₃ ultra thin films with a high electrical field applied (≈ 10 MV/cm) [121]. The detailed internal changes during this switches are not clear yet. The applied electrical field during the presented measurement is about $E_{max} \approx 1$ kV/cm which is 4 orders of magnitude smaller than in the literature. A detailed discussion of this switching effect can be found in section 5.2.

From this temperature up to the final temperature of 520 °C the resistivity shows a steady small linear decrease which is due to the trap filling current [45, 122].

During the cooling the stays in conductive configuration, even in oxygen contact and at room temperature. Although, the Degussa P25 pellet is turned from white to black. Because, the morphology analysis showed a dominance of meso-pores inside the sample and all noise in the signal at temperatures higher than 200 °C can be correlated with temperature ramping artefacts leaking current flow can be neglected. So the resistive switching is connected with a change in the defect structure of the material. It is considered that dipole moments are created similar to SrTiO₃. It can be assumed that a dipole-electrical field interaction process will lead to conducting channels inside the material. Applying a higher voltage triggers a stronger interaction and could open more conducting channels which will lead to a lower overall resistivity. The idea of the conducting channels is discussed in chapter 5.4.

To combine the resistive switching in mild temperature range with the presence of oxygen defects, the titania systems are also analysed in a non-reducing atmosphere, in this case in air. The results for Degussa P25 pellets are shown in figure 4.5.1.

Heating the Degussa P25 pellet, red curve, in air shows a high initial resistivity, slightly higher than in vacuum. At 225 °C a strong peak is observed reaching its minimum of 1 k Ω *cm at 250 °C until an immediate re-storage of the initial resistivity values at 265 °C can be observed. This peak is corresponding with the resistive break down in vacuum. Redistribution of natural lattice defects due to diffusion driven by thermal energy leads to the formation of permanent dipole moments and opens conductive channels analogous to the sample treated in vacuum [29]. The higher possibility of defect healing in oxygen rich atmosphere, air, should cause the restoring of the initial insulating configuration [35, 40]. This proves that stable conductive channels in Degussa P25 are correlated with oxygen defects inside the crystal structure. Although the

aggregation of particles during the heating in air leads to a higher external surface area and lower interface area inside the material which will avoid the formation of stable conductive channels.

At 550 °C a second hard breakdown is measured, where the Degussa P25 pellet changed its resistivity by four orders of magnitude. The temperature is in the range of the phase transition temperature from anatase to rutile. The sample remains in conductive configuration at high temperatures and during the complete cooling. The results shows that at elevated temperatures in air a feasible charge carrier transport is possible. It can be connected with the phase transition temperature, because the formation of rutile triggers a agglomeration of grains. This process lowers the external surface area while the interface area between single particles starts growing which allows an enhanced charge carrier transfer through the metal-oxide pellet. It can be considered that the agglomeration of grains during morphology changes in mild temperature conditions are crucial for the formation of conducting channels.

The measured Degussa P25 pellet stays in a conductive configuration during the cooling but showing a noisy signal between 700 °C and 250 °C. The noise can be connected with leaking current through newly formed micro-pores. This current is not stable when morphology changing processes are not finished yet. Steady changes in the pore size distribution inside the material during the cooling influences directly the leaking current. After the air treatment the sample stays white and did not turn into a black pellet.

The measurements in air show a strong influence of external effects, especially leaking current due to changes in the pore size distribution.

4.5.2 SOL-GEL-BASED-POWDER

The sol-gel-based sample is characterised by an amorphous structure which includes high amounts of organic rests despite the spray-drying process at 180 °C. The resistivity shows a significant differences compared to crystalline titanium dioxide measured in vacuum. The results are presented in figure 4.5.2.

A strong decrease of resistivity can be observed at low temperatures which is caused by the pyrolysis of organic rests from a non-complete polycondensation [59, 123]. This strong decrease up to 180 °C can be determined as ionic current during this pyrolysis. This proofs that high slopes during the measurement are characteristic for ionic current flow instead of trapping current flow. Furthermore, there is no hard break down effect observed at around 220 °C despite the high external electrical voltage. The loss of resistivity is observed in a wider temperature range with three different steps up to a temperature of 300 °C. After that the sample stays in a conductive configuration with a constant resistivity value during the further heating process and the following cooling

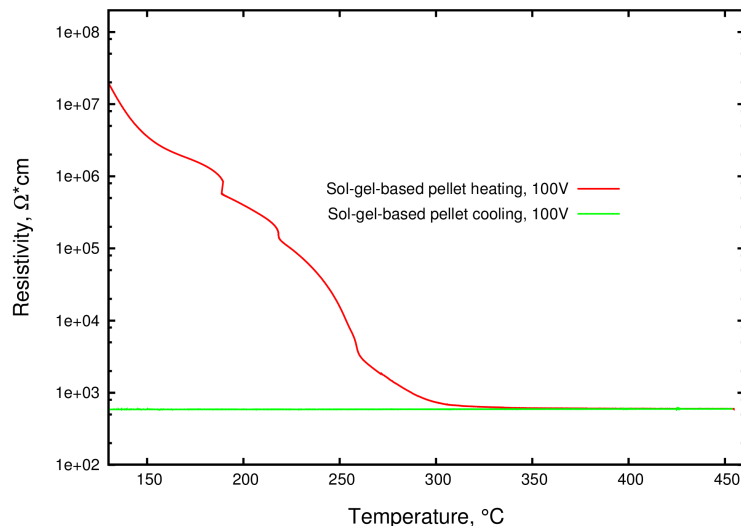


Figure 4.5.2: Measurement of the resistivity over temperature of sol-gel-based-sample in high vacuum. The reference resistance is $R_R = 1 M\Omega$.

process. It could be assumed that the formed anatase crystals at temperatures higher than 400°C are highly defective [40]. This results in a titanium dioxide configuration which should show electrical properties that are significantly different compared to the electrical properties of the Degussa P25 pellets and the anatase thin film samples.

4.5.3 THIN FILMS

The characterisation of the charge carrier transfer in titanium dioxide thin films will be done analogous to the characterisation of the charge carrier transfer in titanium dioxide pellets. The main advantage of the thin films is that external effects caused by pores can be neglected because the anatase thin films synthesised by CVD-method are assumed as quasi-fully densified.

The results of the thin film analysis are presented in figure 4.5.3 top. The applied external voltage is smaller than for Degussa P25 pellet samples because of the thinner titanium dioxide structure (thickness $< 1 \mu\text{m}$).

At 180°C a hard resistivity breakdown is observable which lead to a change in resistivity of five orders of magnitude. The breakdown can be distinguished into two parts. First, a strong decrease from 180°C to 210°C and second, a slighter decrease from 210°C to 400°C . The heating curve shows that even in fully densified pure anatase thin films the permanent resistive switching from insulating to conducting configuration can be observed in vacuum which is also stable during the cooling process. In contrary to the pressed pellet systems a minimum in resistivity can be reached at 400°C . Although, an instantaneous rise of resistivity can be measured when the valve is opened and the sample is exposed to air. The insulating state of titanium dioxide is restored.

The anatase thin films are monocrystalline and quasi-fully densified, so the influence of

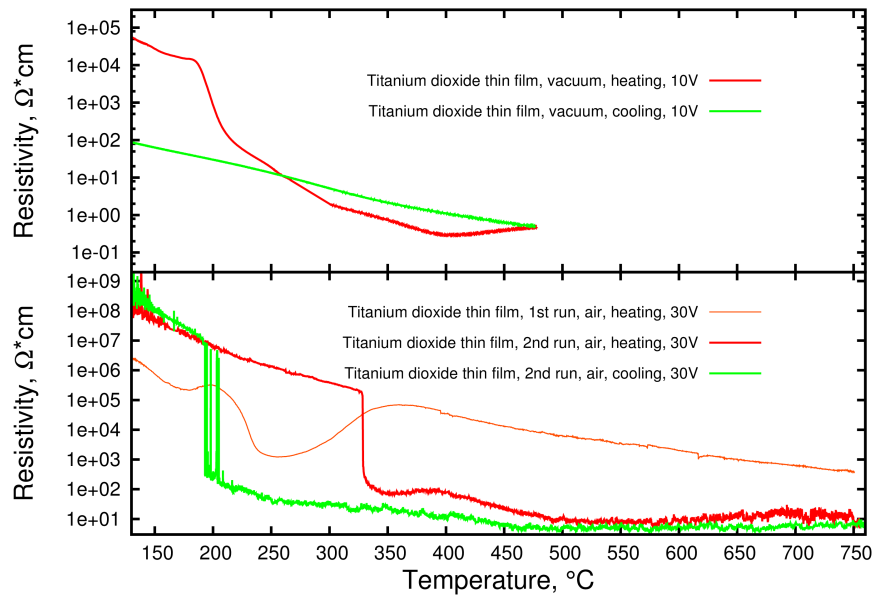


Figure 4.5.3: Measurement of the resistivity over temperature of thin film anatase samples in vacuum and air. The reference resistance is $R_R = 1 M\Omega$. Between the first run and the second run of the second sample an I-V-characteristic was performed. The reference resistance is $R_R = 1 k\Omega$ during the 2nd run of the second sample. Modified from [42].

external effects and morphology changes can be neglected, so the results are showing that a change in the crystalline structure of titanium dioxide could be the actuator of the conducting configuration of titania. It is assumed that oxygen vacancies formed by electron flow and heat treatment in vacuum leads to defective titania octahedrons with a permanent dipole moment [110, 124]. The alignment of these dipoles in an external electrical field could open conducting channels. The minimum of resistivity at 400°C can be explained by reaching a maximum of defect formation and the growth of the resistivity at the end of the heating is due to a polarisation field inside the titanium dioxide thin film which reaches a significant strength. With the exposition to air oxygen atoms relaxed in lattice vacancies and the initial insulating state is restored. Because there are not enough line defects, such as grain boundaries between two different phases, the lattice defects are highly de-localised and oxygen atoms can easily diffuse through the material and heal lattice defects and restore insulating configuration of the sample.

In the last step the resistivity of a pure anatase quasi-fully densified thin film is characterised in air. The measurement is presented in figure 4.5.3 bottom. An error during the cooling causes an different way of presentation. The orange curve presents the original resistivity measurement. Followed by a second run on the exact same sample which is presented in red and green curves.

During the 1st heating of the thin film sample, orange curve, a similar behaviour compared to the Degussa P25 pellet in air is observed in mild temperature regime. This is characterised by a short break down in resistivity followed by the re-storage of the insulating configuration at elevated temperatures.

The second heating process, red curve, starts at high resistivity, proofing during the initial resistivity level was formed during the first cooling process. At 330°C a hard breakdown into a conductive state is observable. The titanium dioxide stays in the conductive configuration during the further heating as well as during the cooling down to 190°C. At this temperature a hard re-switching in insulating state is observable. The second run shows that because of the lattice changing processes below 350°C in the first run and the formation of a two crystalline phase system, a rutile formation during the first heating process, a titania thin film with an increased amount of line defects is designed so that dipoles are stable even in air. These dipoles can be aligned by applying an electrical field and heat the sample up to 330°C. Conductive channels are opened and these channels stays accessible till 190°C where the dipoles are in arbitrary orientation again and the insulating state of the titanium dioxide is restored at the exact same value like during the heating. A hysteresis curve can be observed.

In summary, the resistivity measurements are showing that a structural change during a heating process causes a resistive switching. This switching is connected with oxygen defects, newly formed or redistributed, because in vacuum a permanent conductive configuration is observed. Permanent dipole moments are induced due to this new oxygen defect structure. The alignment of the dipoles opens conductive channels causing the resistive switching. The presence of line defects, grain boundaries or phase boundaries, pins special oxygen defects and the permanent dipole moments. This leads to a permanent conductive configuration even in air and at room temperature in Degussa P25 pellets until the alignment is nullified.

4.5.4 BARRIER ENERGY OF THE CHARGE CARRIER TRAPS

The resistivity measurements are the basis of the calculation of the barrier energy of charge carrier traps inside the titanium dioxide systems. The method of analysis is explained in chapter 2.1.2. An example of the analysing procedure is given in figure 4.5.4. The slope of the linear parts are calculated by a linear fit. The aim is to analyse the energy barrier for a temperature range before the resistive switching and after the resistive switching. Additionally, a third calculation for the cooling system is performed.

The results of the energy barrier calculation is presented in table 4.5.1 for each titanium dioxide system. Firstly, the energy barrier in anatase thin films calculated during

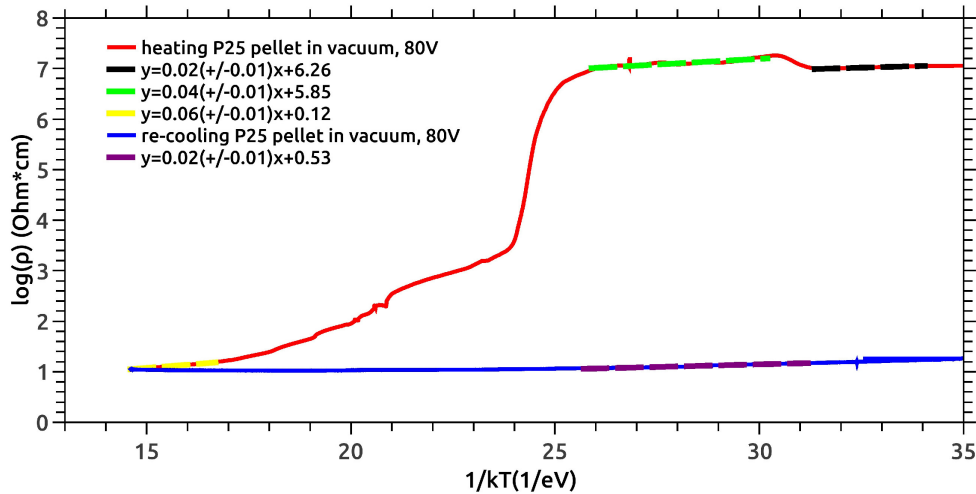


Figure 4.5.4: Measurement of the resistivity over temperature of a Degussa P25 titanium dioxide pellet in vacuum including linear fits to calculate the barrier energy of the charge carrier traps during the resistive switching process. The reference resistance is $R_R = 1 M\Omega$.

the heating process is naturally higher than the energy barrier in Degussa P25 pellets. This means that less trapping sites are included in anatase thin films than in Degussa P25 pellets. Furthermore, the high values in anatase thin films, $E_B > 0.2 eV$, shows that the method reaches its limits. It is assumed that a low doped semi-conductor is measured which shows no thermoelectric current flow [45]. But the anatase thin films are not fully crystallised and included an amorphous fraction which could lead to ionic based current flow and influencing the measurement results. Nevertheless, the second heating process of a anatase thin film sample shows similar behaviour like Degussa P25 pellets. The sample is fully crystallised and shows no significant change in trapping sites structure before and after the resistive switching in vacuum.

The Degussa P25 pellets are characterised by a energy barrier of $E_B \approx 0.055(\pm 0.011) eV$ before and after resistive switching in vacuum. This shows that the defect structure could be redistributed but the pure amount of trapping sites inside the sample is not changing significantly. The high error is caused by the unique setup and by the assumption of a low doped semiconductor with constant doping concentration. In vacuum a shallow reduction process as well as a redistribution process of defects could lead to new formation or loss of trapping sites [29]. This will influence the measured trapping current.

The barrier energies calculated from the cooling measurements are slightly smaller than during the heating process and a similar to low temperature energy barriers (from $65^\circ C$ to $100^\circ C$) which shows that the current flow during cooling could be influenced by ionic current or other neglected processes.

Finally, the measured sol-gel-based pellets shows a significant change in energy barrier.

But this can be explained because of the pure amorphous structure before the switching. The sample itself is crystallising during the measurement, leading to a highly defective conductive titanium dioxide structure which reaches the limits of the used method. The assumptions are not working for highly doped semiconductors.

In summary, the results are showing that the resistive switching is not directly connected with a significantly increase of charge trapping sites and oxygen defects inside titanium dioxide. Furthermore, it could be considered that the resistive switching is caused by a structural change which will lead to dielectric phase transition which can trigger anisotropically conductive channels.

Table 4.5.1: Calculated energy barrier of charge carrier traps for various titanium dioxide systems under different measurement conditions. The energy barrier calculation is based on the slope of the in-situ resistivity measurements [29, 42].

Sample	run	Temperature range / °C	energy barrier / eV
Degussa P25 pellet, vacuum, 80 V	1st heating	65 - 95	0.023
		110 - 175	0.045
	1st cooling	420 - 520	0.064
		175 - 95	0.021
Degussa P25 pellet, vacuum, 30 V	1st heating	117 - 160	0.048
	1st cooling	290 - 500	0.045
		500 - 280	0.029
	2nd heating, after I-V	160 - 110	0.025
		15 - 60	0.170
		310 - 500	0.086
2nd cooling		500 - 330	0.009
		190 - 85	0.007
Degussa P25 pellet, air, 50 V	1st heating	160 - 220	0.068
		315 - 375	0.101
Sol-gel based pellet, vacuum, 100 V	1st heating	145 - 175	0.216
	1st cooling	325 - 455	0.005
		185 - 60	< 0.001
TiO ₂ thin film, vac, 10 V	1st heating	125 - 170	0.222
		280 - 395	0.283
	1st cooling	475 - 305	0.021
		205 - 80	0.010
TiO ₂ thin film, vac, 100 V	1st heating	105 - 175	0.087
	1st cooling	365 - 430	0.339
		455 - 365	0.113
	2nd heating	115 - 25	0.028
		115 - 170	0.077
		330 - 520	0.077
	2nd cooling	520 - 725	0.067
500 - 185		0.112	
		125 - 40	0.085
TiO ₂ thin film, air, 100 V	1st heating	130 - 175	0.420
		380 - 750	0.330
	2nd heating, after I-V	130 - 190	0.357
		380 - 515	0.400
	2nd cooling	495 - 240	0.137
		190 - 130	0.404

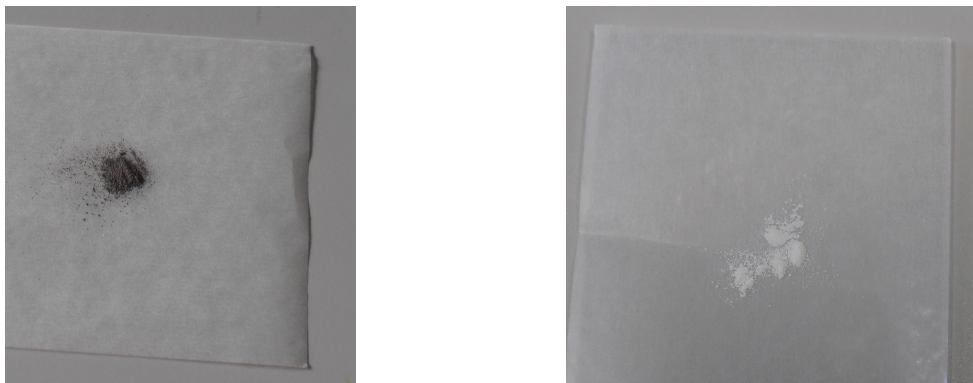


Figure 4.6.1: Photography of the mauled black titania pellet treated at 450 °C before(left) and after(right) healing process. This healing process includes a heat treatment in air at 400 °C for 2 h.

4.6 DEFECT ANALYSIS - EPR

While using XPS and resistivity measurements only small changes in defect structure can be determined. Therefore the bulk sensitive method of electron spin paramagnetic resonance spectroscopy is done. The aim is to specify the black colour centres in titanium dioxide pellets after the resistivity measurement in vacuum.

According to [125] titanium dioxide turns black when either a hydrogenation took place or the transition metal oxide is heavily reduced. The first process means the coverage of the TiO_2 surface with hydrogen molecules forming an amorphous outside layer [126]. The second process assumes the formation of monoclinic $TiO_{1.66}$. The strong reduction is based on an electron flow due to an electrical current in the conducting state of titanium dioxide after the break down effect which will lead to [110]:



It is possible that during the heat treatment in vacuum the increasing current during the resistivity measurement benefits the reduction of the titanium atoms or forming and stabilizing oxygen vacancies. Therefore the reversibility of this process is analysed by performing a healing process to the black pellet sample. In this case the pellet is mauled and then tempered for 2 h in air at 400 °C. The aim is to oxidise the titanium dioxide and heal possible defects.

Figure 4.6.1 shows the powder before and after the healing process. It is obvious that the powder restore the white colour, which works with both systems, the Degussa P25 powder as well as the sol-gel-based powder.

To characterise the defect structure during the changes from white powder to black powder back to white powder EPR experiments are performed. Starting with the original Degussa P25 powder, the most photocatalytic efficient powder (Degussa P25 powder treated at 400 °C in vacuum) and a intermediate sample(Degussa P25 pellet

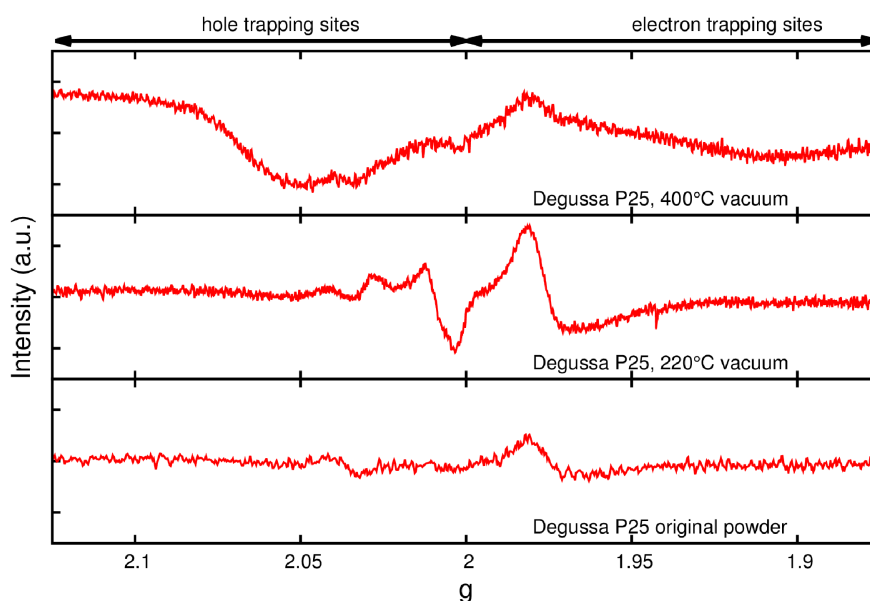


Figure 4.6.2: EPR-spectrum of selected Degussa P25 powder or pellet samples measured at 100 K [29].

treated in the XPS preparation chamber at 220 °C). The results for these very samples are shown in figure 4.6.2 measured at 100 K. The focus is on the g -factors of the titanium or oxygen resonance lines, namely [127–129]:

- the Ti^{3+} -lattice states in anatase and rutile at $g = 1.981$
- the lattice oxygen vacancies V_O at $g = 2.002$ - the quasi free electron
- adsorbed O_2^- -states at $g = 2.012$ and $g = 2.028$ - which are indirectly proofs of former oxygen defects which adsorbing this oxygen species after the powder was exposed to the air
- surface hole trapping sites at $g > 2.000$
- electron trapping sites at $g < 2.000$

Inside the original Degussa P25 powder only Ti^{3+} -states can be detected which are natural defects in Degussa P25 titanium dioxide powder. The powder treated at 400 °C in vacuum as well as the pellet treated at 220 °C in the XPS preparation chamber shows a higher response at this g -value, so the amount of Ti^{3+} defects has risen during mild temperature treatment in high vacuum, but there is no significant difference between 400 °C and 220 °C.

The sample treated at 220 °C shows resonances that indicates oxygen vacancies, because in this sample resonances at $g = 2.002$ as well as at $g = 2.012$ and $g = 2.028$ can be measured. This could mean that the highest amount of oxygen lattice vacancies was

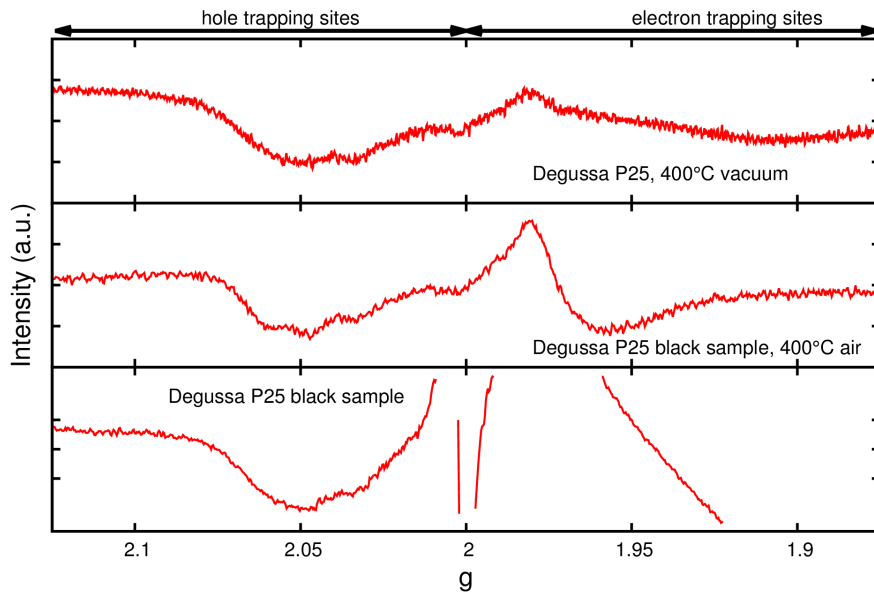


Figure 4.6.3: EPR-spectrum of selected Degussa P25 powder or black pellet samples measured at 100 K, the Degussa P25 powder heat treated at 400 °C in vacuum is chosen as a reference powder.

formed during the treatment of this sample. That means, despite the higher temperature the amount of oxygen vacancies is lower in powder treated at 400 °C compared to Degussa P25 pellets treated at 220 °C.

Furthermore the Degussa P25 powder heated at 400 °C is the only powder that shows the clear presence of charge carrier traps indicated by a broad resonance around $g = 2.050$. It can be assumed that during the tempering process in an reduced atmosphere a formation and redistribution of TiO_2 defects took place. Starting with the formation of oxygen vacancies and Ti^{3+} -states at temperatures between room temperature and 220 °C, a redistribution of the lattice oxygen defects into charge carrier traps between 220 °C and 400 °C is observed [29].

In the following step the black pellet designed by applying an electrical field and electrical current during the heat treatment in vacuum is analysed and compared with Degussa P25 powder treated in vacuum at 400 °C. Because, on one hand a black P25 pellet treated up to 450 °C is chosen, so the maximum temperatures for both samples are close to each other and on the other hand the reference powder is the photocatalytic improved powder.

In figure 4.6.3 the results for the black pellet as prepared, the black pellet after the healing process and the Degussa P25 powder treated at 400 °C in vacuum as reference sample measured at 100 K is presented. It is obvious that the most defective sample is the black Degussa P25 pellet sample. The resonances for the Ti^{3+} -states as well as for the lattice oxygen vacancies are an order of magnitude higher than in the reference

powder. For a better comparison of the charge trapping sites, the high resonances were cut in this presentation. The complete EPR-spectra are presented in figure C.1. The significant stronger intensities indicating a strong reduction inside the black sample. Oxygen lattice vacancies as well as Ti^{3+} -lattice sites are formed which are highly delocalised.

The signal correlated with charge trapping sites is also pronounced in the black Degussa P25 pellet and is significantly stronger for electron trapping sites, $g = 1.908$, compared to the reference powder. The signal resonance for hole trapping sites, $g = 2.050$, is similar with the signal resonance for this g-values in the Degussa P25 powder treated at 400°C . So this kind of metal oxide defect is not directly connected with the strong reduction of the metal oxide lattice by using an electron overflow.

Inside the healed sample, a white powder, Ti^{3+} -sites are detected comparable with other white samples. It seems that oxygen lattice vacancies are not present in this sample. The tempering in air even at a temperature lower than the maximum temperature during the reduction process leads to the healing of the oxygen defects. Nevertheless, a resonance for hole trapping sites can be measured for this sample. This shows on one hand that the black colour is correlated with a strong reduction of the TiO_2 -crystals. On the other hand, the presence of hole trapping sites did not depending on the presence of oxygen lattice vacancies. It is possible that the hole trapping sites are localised defects, formed in the interface area [29]. That means that grain boundaries, especially between two different crystalline phases, are preferred areas for oxygen defects acting as hole trapping sites. These defects are showing a high stability and can not be healed by heating the sample air.

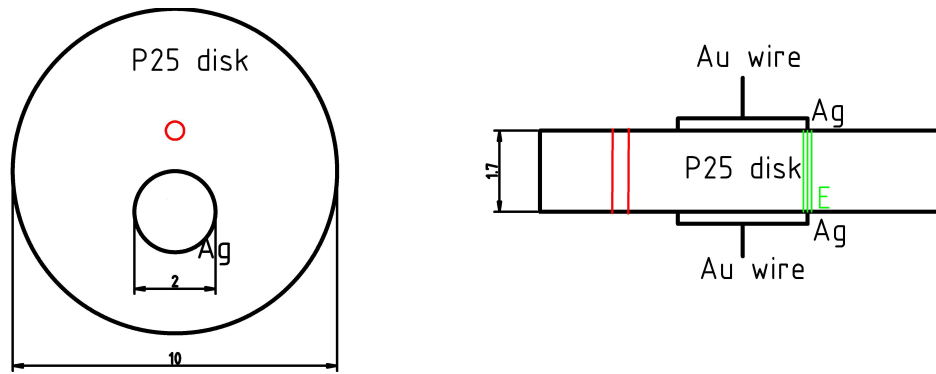


Figure 4.7.1: Sketch of the measured Degussa P25 pellet, with a measurement spot (red) or channel, respectively, outside of the silver electrode and an external electrical field normal to the surface (green).

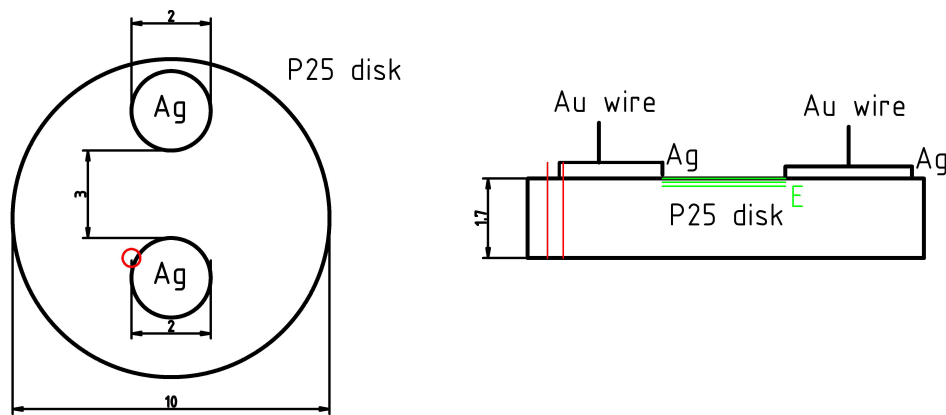


Figure 4.7.2: Sketch of the measured Degussa P25 pellet, with a measurement spot (red) or channel, respectively, on the edge of the silver electrode and an external electrical field tangential to the surface (green).

4.7 STRUCTURAL ANALYSIS - XRD

4.7.1 IN-SITU-MEASUREMENTS

At the P07 beam line at the DESY in Hamburg in-situ experiments are performed to determine structural changes in the titanium dioxide crystal structure during the resistive switching effect. The unique setup is explained in chapter 3.1.1.

For this investigation the structure is measured while the Degussa P25 pellets are heated in a vacuum chamber ($p \approx 10^{-4} \text{ mbar}$) with three different external electrical field configurations. Firstly, without any external electrical field (E_0) applied to measure a reference pellet. Secondly, with an external electrical field orientated normal to the surface (E_n) and a measurement spot outside of the silver electrode. A detailed sketch is shown in figure 4.7.1. Thirdly, with an external electrical field orientated tangential to the surface (E_t) and a measurement spot on the edge of the silver electrode. A detailed sketch is shown in figure 4.7.2.

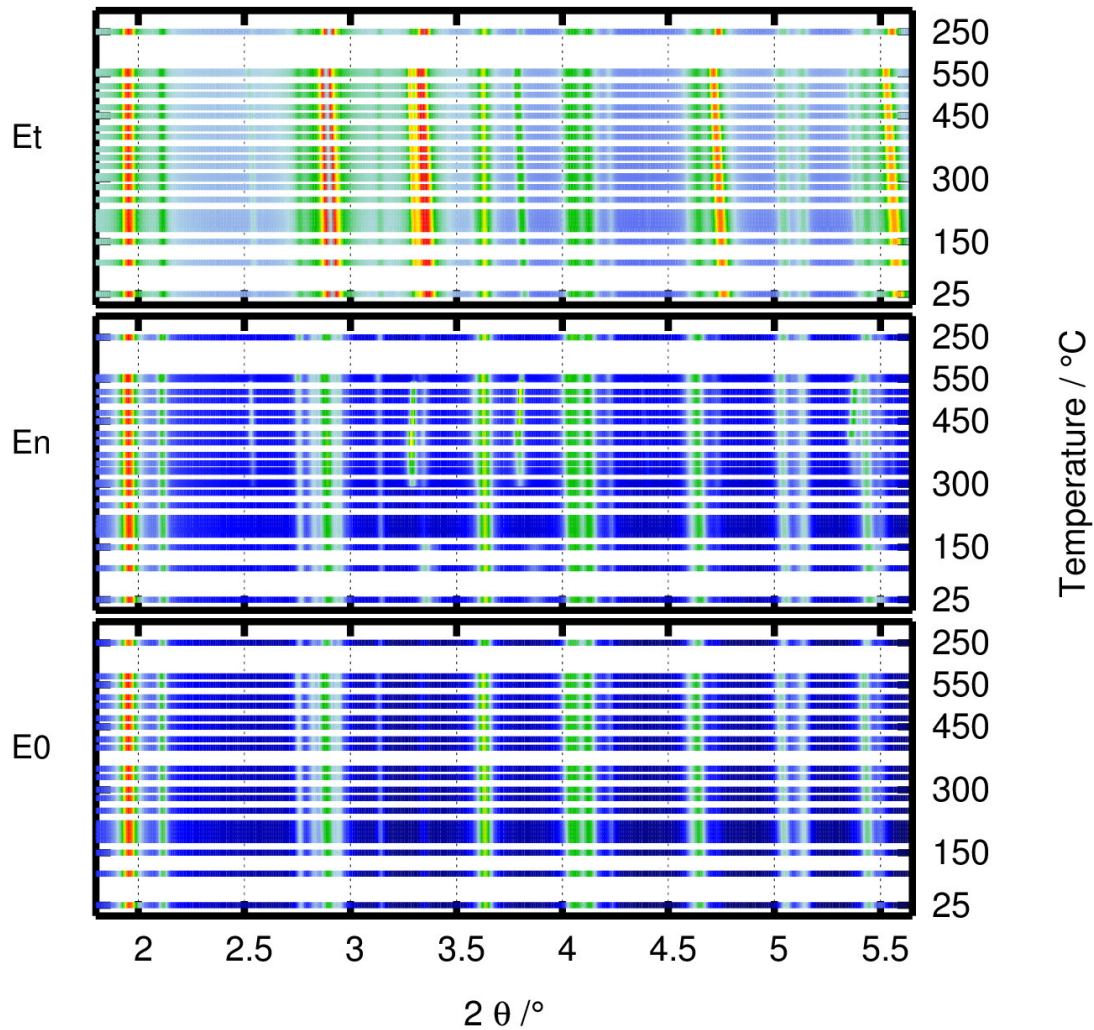


Figure 4.7.3: Intensity mapping of in-situ X-ray diffraction measurements in vacuum ($p \approx 1 \cdot 10^{-4} \text{ mbar}$) with different external electrical field orientation and different measurement positions on Degussa P25 pellets. The intensity is standardised to the intensity of the anatase (101)-reflex of each measurement and is plotted in logarithmic scale in the range of $[0.02 \cdot I_{A(101)} : 6.00 \cdot I_{A(101)}]$, modified from [42].

The overall results of the in-situ X-ray diffraction measurement are shown in figure 4.7.3. In this graphical presentation the 2D-X-ray patterns of every measurement step is integrated over the whole χ -angle and will not show any texture characteristics. The resistivity measurements during the in-situ X-ray diffraction are presented in figure A.1 and proof that a resistive switching from insulating to conducting can be achieved for the samples with an applied external field. The breakdown is more shallow than during resistivity measurements in higher vacuum. This can be explained by the lower vacuum as well as by the smaller applied external voltage of 5 V.

The intensity mapping shows no anomalies for the sample without the external electrical field. Only anatase and rutile crystal phase can be detected.

The intensity mapping for the Degussa P25 pellets with an external electrical field

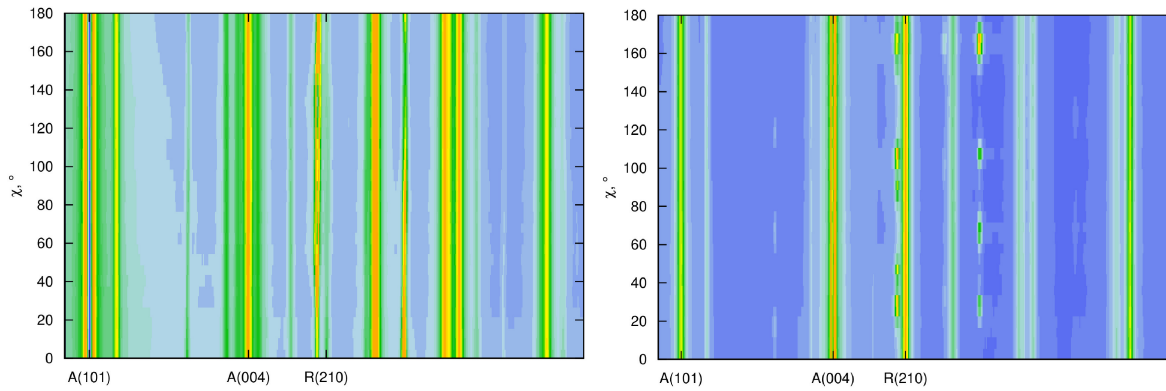


Figure 4.7.5: 2D map-plot of Degussa P25 pellet samples measured at 500 °C during the heating process in vacuum. The external electrical field is applied normal to the surface and the measurement spot is outside of the electrode(left) or the external electrical field is applied tangential to the surface and the measurement spot is on the edge of the electrode(right). The intensity is in square-root scale [42].

It is possible to consider the presence of a superstructure due to induced lattice defects. But the number of the new reflexes and their different intensity evaluation would imply a minimum of four different superstructures due to periodical orientation and reorganisation of lattice defects which is not probable.

The position dependency of the presence of the new reflexes are presented by an intensity mapping over the χ -angle in figure 4.7.5. A strong curvature in the unknown reflexes compared to anatase reflexes indicates a strong mechanical stress inside the material. It also demonstrates a significant texture for the unknown reflexes.

While the reflexes with strong intensity in the Et-sample could be connected with silver, because the measurement spot is on the edge of the electrode these three ($2\theta = 2.89^\circ ; 3.32^\circ ; 4.28^\circ$) reflexes are neglected. Then the new reflexes in the Et-samples are equal to the En-sample which is demonstrated in figure 4.7.6. The integration over selected χ -angles and for characteristic temperatures shows in both cases, En and Et, a different orientation dependency especially for the reflexes at [$2\theta = 2.54^\circ ; 3.29^\circ ; 3.58^\circ ; 3.80^\circ$].

Furthermore, the texture characteristic, figure 4.7.5, is stronger pronounced. This can be explained by the different evaluation of the homogenisation of the internal electrical field during the heating and resistive switching process. Close to the outside edge of the electrode for an external electrical field tangential to the surface, the orientation of the internal electrical field stays constant. While the internal electrical field for the En sample shows a non-homogeneous orientation after the conductive switching.

All these factors leading to the possibility that a new titanium dioxide phase was formed during the vacuum calcination with an electrical field applied. The idea of this new phase is discussed in the following chapter.

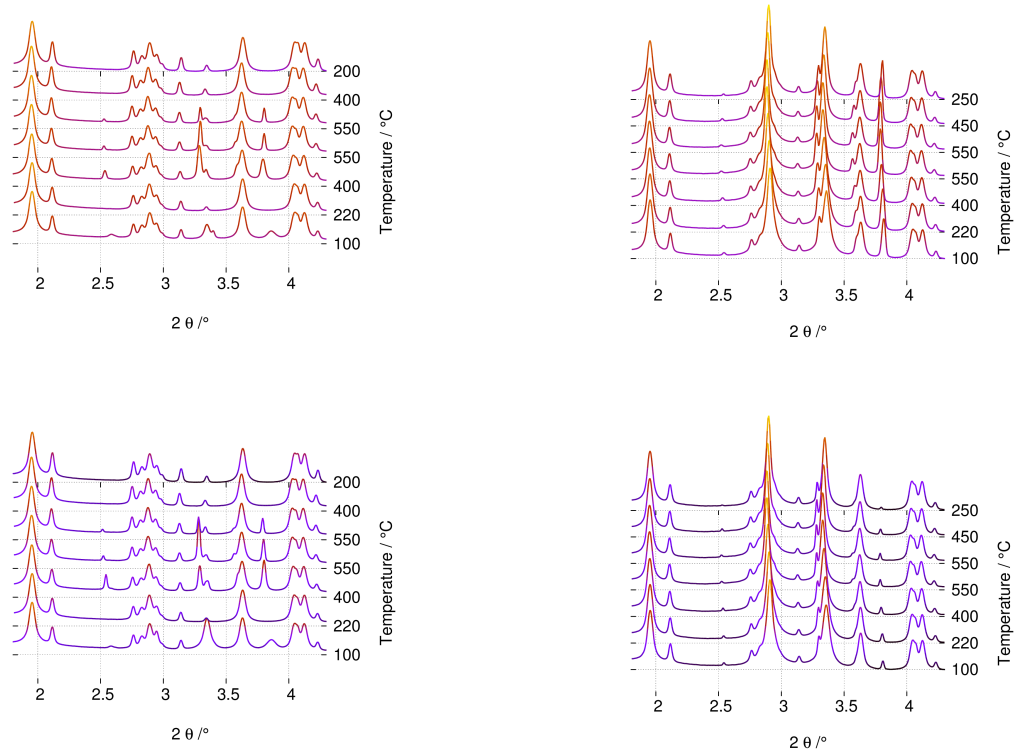


Figure 4.7.6: Orientation dependency of the X-ray diffraction in-situ measurements in vacuum ($p \approx 10^{-4}$ mbar) for Degussa P25 pellets at selected temperatures. **Left:** external electrical field normal to the surface and the measurement spot in 1.5 mm distance to the electrode integrated in $\chi = 20^\circ$ (top), $\chi = 110^\circ$ (bottom). **Right:** external electrical field tangential to the surface and the measurement spot on the edge of the electrode integrated in $\chi = 20^\circ$ (top), $\chi = 110^\circ$ (bottom) [42].

4.7.2 PSEUDO TITANIUM DIOXIDE PHASE - ARMINIASE

Titanium dioxide phase formation processes are based on the thermodynamic potential of the Gibbs free energy [66]. The equation 2.2.1 can be written as:

$$G = H - T \cdot S + p \cdot V_m + \frac{2f_s}{r} \cdot V_m + \gamma \cdot A_m + \phi$$

with the Gibbs free energy G , the enthalpy H , entropy S , temperature T , surrounding atmospheric pressure p , internal pressure of the material $p' = \frac{2f_s}{r}$ including the surface tension f_s and the particle radius r , molar volume V_m , free surface energy γ , molar surface area A_m , and remaining factor for shape or porosity ϕ .

It is known that anatase formation is preferred for small crystallite sizes due to the smaller free surface energy compared to rutile [26,62]. Nevertheless, rutile is the thermodynamic stable configuration of titanium dioxide, which is caused by its smallest volume free energy compared to other titanium dioxide crystal configurations.

Additionally, brookite is known as the third stable titanium dioxide configuration. It

is a orthorhombic crystal structure which can be synthesised by a bottom up method including a high mechanical stress during the tempering process of amorphous titanium dioxide [26, 135]. It follows that:

$$G = H - T \cdot S + \underbrace{p \cdot V_m + \frac{2f_s}{r} \cdot V_m}_{\text{rutile term}} + \underbrace{\gamma \cdot A_m}_{\text{anatase term}} + \underbrace{\beta(f_s, \phi)}_{\text{brookite term}} \quad (4.7.1)$$

the Gibbs free energy includes a rutile term, an anatase term and a brookite term, respectively. This brookite term includes a shape factor and a factor of high mechanical internal stress. Considering a system where the brookite term is most dominant compared to the other an orthorhombic crystal system is formed instead of a tetragonal one. An anatase to brookite phase transition is probable [136].

Analogous to the brookite formation process it seems likely that inside an external electrical field the Gibbs free energy of the titanium dioxide systems is changed. Additionally, the presence of lattice defects which can cause permanent dipole moments will change the internal stress depending on the orientation of the external electrical field. Hence, equation 4.7.1 is extended by a factor depending on an external potential:

$$G = H - T \cdot S + \underbrace{p \cdot V_m + \frac{2f_s}{r} \cdot V_m}_{\text{rutile term}} + \underbrace{\gamma \cdot A_m}_{\text{anatase term}} + \underbrace{\beta(f_s, \phi)}_{\text{brookite term}} + \underbrace{\alpha(E_e, \iota)}_{\text{new defective phase}} \quad (4.7.2)$$

with a term of a new phase α depending on an external potential E_e and an ionic structure ι defined by the defective structure of the material.

According to [137] theoretical calculations predicting that TiO_2 is based on covalent titanium-oxygen-bonds while TiO_1 is based on ionic titanium-oxygen-bonds. It predicts also that the defective configuration Ti_2O_3 or $\text{TiO}_{1.66}$ is an intermediate state between covalent and ionic bonding which is characterised by an extension of the Ti-O bond length up to 18 % compared to TiO_2 .

That means a change in the defective structure of titanium dioxide will lead to a possible extension of the titanium-oxygen-bond length and give the titanium dioxide system a more ionic character. So, highly localised oxygen defects can change the properties from titanium dioxide to a similar configuration of e.g. strontium titanate, SrTiO_3 [138]. Strontium titanite can also be in orthorhombic crystal structure [139]. The determination of the chemical composition of the Degussa P25 pellets by various methods revealed that assuming $\text{TiO}_{1.66}$ overestimates the true amount of oxygen defects. Nevertheless, it can be considered that there is a non-isotropic defect distribution. It is probable that highly defective areas are present inside the samples especially close to line defects such as grain boundaries.

Hence, for the overall sample it might be possible to write the stoichiometry of the

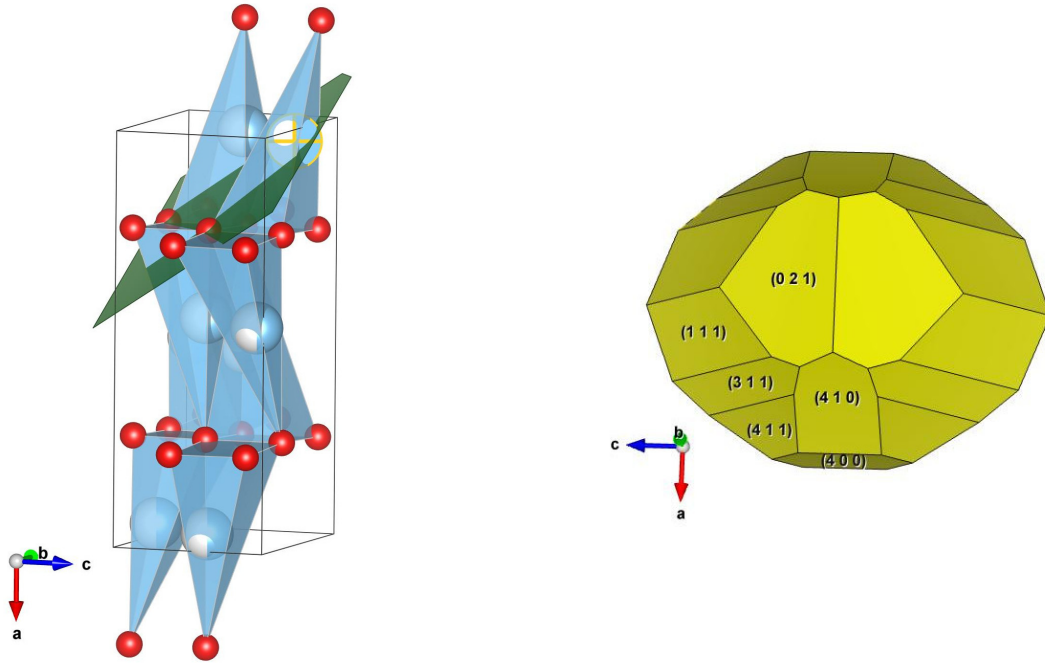
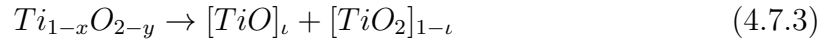


Figure 4.7.7: Graphical representation of the unit cell of the arminias phase with the lattice plane (411) which defines the characteristic titanium-oxygen-bond (left) and of the crystal shape of the arminias phase represented by the characteristic lattice planes defined by the reflections which could not be dedicated to real titanium dioxide phases (right) [42]. Plotted by [41].

analysed titanium dioxide system in the following way [42]:



with a factor of possible ionic bond formation ι which depends on the defective structure.

The combination of equation 4.7.3 and the Gibbs free energy equation 4.7.2 will be used to design a theoretical pseudo titania phase that could explain the unknown reflexes measured during the in-situ experiments. An orthorhombic crystal structure with a oxygen-to-titanium ratio of $\frac{O}{Ti} < 2$ is assumed. The titanium positions are based on the brookite system and the oxygen positions are refined for the measured unknown phase. The bonding length of Ti-O bonds is limited to:

$$1.6 \text{ \AA} \leq l \leq 2.80 \text{ \AA}$$

with the lower limit as covalent bond length in TiO_2 [137] and the upper limit as metal-oxygen bond length in $SrTiO_3$ [140].

The result of this refinement is an auxiliary titania phase which is presented in figure 4.7.7. It needs to be mentioned that the occupancy of the titanium lattice spots is 0.5. It depends on the orientation of the electrical field which titanium lattice site is

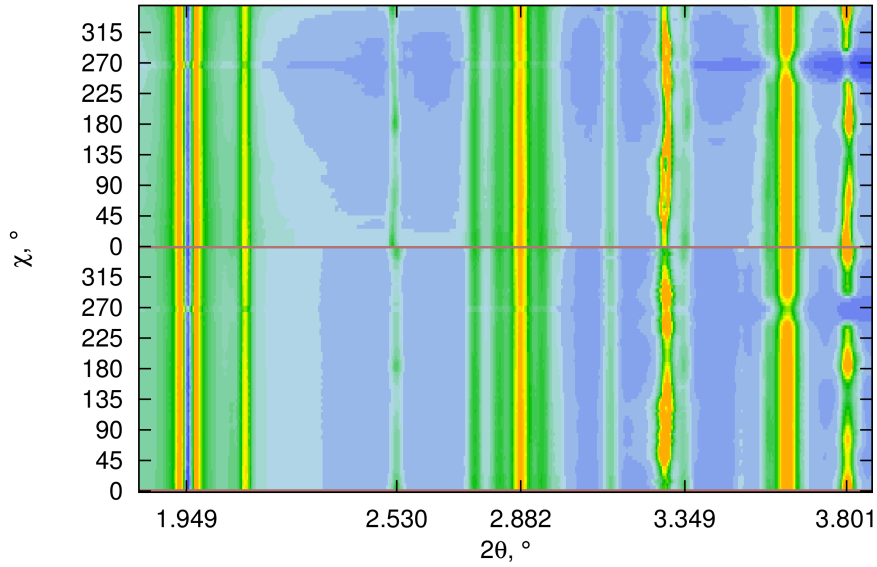


Figure 4.7.9: 2D experimental data(bottom) and 2D theoretical calculated data (top) of the integrated XRD-spectra of a Degussa P25 pellet measured in-situ in vacuum ($p \approx 1 \cdot 10^{-4} \text{ mbar}$) with an external electrical field normal to the surface at 500°C . Refinement includes the arminiase-phase. The intensity is in square-root scale. Modified from [42].

on the assumption of the existence of an arminiase phase with the cell parameters:

$$a = 9.31(\pm 0.04) \text{ \AA}$$

$$b = 4.69(\pm 0.06) \text{ \AA}$$

$$c = 3.54(\pm 0.03) \text{ \AA}$$

and an arbitrary texture characteristic.

It can be observed that the crystallite growth and the phase transition from anatase to rutile depend on the presence of an external electrical field and on the measurement position on the Degussa P25 pellets. The sample with an electrical field normal to the surface shows a stronger crystallite growth for anatase and rutile crystals compared to the sample without any electrical field and the sample with an electrical field tangential to the surface. Furthermore, a significant increase in the anatase-to-rutile ratio can be determined during the annealing in vacuum. In this case amorphous material crystallises because of the influence of the external field.

It can be assumed, that the electrical field enhances the agglomeration of grains and this supports the crystallisation process [109, 141]. This leads to larger average crystallite sizes and a higher anatase fraction.

Furthermore, the results for samples annealed at 550 °C show that the phase transition from anatase-to-rutile is declined. This indicates, that a third crystalline phase, arminiase, is present. The grain growth of such a third phase can suppress the anatase-to-rutile transition [56, 142–145].

Table 4.7.1: XRD results of selected titanium dioxide samples from XRD measurements calculated by Rietveld refinement [42, 51].

Sample	atmosphere		Anatase (A)		Rutile (R)		A/R			
			%	cryst. size, nm	%	cryst. size, nm				
powder	vacuum	E(0)	25 °C	83.3	25.0	16.7	42.3	5.0		
			200 °C	83.6	25.4	16.4	42.4	5.1		
			400 °C	83.8	25.6	16.2	43.3	5.2		
			550 °C	77.7	26.8	22.3	43.5	3.5		
			600 °C	67.0	28.4	33.0	51.7	2.0		
			620 °C	40.3	27.7	59.7	54.5	0.7		
			650 °C	10.0	33.9	90.0	68.4	0.1		
			670 °C	8.5	39.1	91.5	75.5	0.1		
			700 °C	0.0	-	100.0	86.0	0.0		
			air ()	E(0)	25 °C	83.3	25.0	16.7	42.3	5.0
					200 °C	83.5	25.2	16.5	42.6	5.1
					400 °C	83.4	25.7	16.6	44.5	5.0
					550 °C	78.2	28.6	21.8	48.5	3.6
					600 °C	67.7	28.4	32.3	50.0	2.1
620 °C	53.4	32.6			46.6	61.0	1.2			
650 °C	36.6	32.4			63.4	66.5	0.6			
670 °C	23.0	35.2			77.0	75.9	0.3			
700 °C	6.6	45.8			93.4	97.8	0.1			
pellet	vacuum	E(n)			450 °C	78.7	36.5	16.0	60.7	4.9
pellet in-situ XRD heating	vacuum	E(0)			25 °C	85.7	39.4	14.3	55.7	6.0
					180 °C	86.6	40.0	13.4	56.8	6.5
					220 °C	87.0	40.7	13.0	58.3	6.7
					300 °C	87.3	42.4	12.7	68.0	6.9
			450 °C	87.0	43.7	13.0	70.2	6.7		
			550 °C	82.8	52.5	17.2	83.0	4.8		
pellet in-situ XRD heating	vacuum	E(n)	25 °C	85.5	41.9	12.7	63.0	6.7		
			180 °C	87.3	39.8	12.7	56.8	6.9		
			220 °C	87.4	41.2	12.6	63.6	6.9		
			300 °C	86.3	44.3	11.7	75.1	7.4		
			450 °C	84.2	53.3	10.3	90.6	8.2		
			550 °C	84.4	50.5	14.8	130.2	5.7		
pellet in-situ XRD heating	vacuum	E(t)	25 °C	81.3	39.0	12.3	62.1	6.6		
			180 °C	81.5	46.6	12.0	62.6	6.8		
			220 °C	84.0	47.1	11.1	70.1	7.6		
			300 °C	80.0	49.3	11.7	70.4	6.8		
			450 °C	78.1	43.8	12.9	67.8	6.1		
			550 °C	78.3	45.7	11.87	72.8	6.6		

Chapter 5

Discussion

Treating different titanium dioxide systems, such as titanium dioxide thin films, Degussa P25 powder and sol-gel based powders in reducing atmosphere various anomalies are observed in the temperature range between 200 °C and 450 °C. These anomalies will be discussed in the following way:

Firstly, the photocatalytic efficiency for powders is analysed with the focus on the improvement at 400 °C and on the neutralisation at 600 °C. It is necessary to understand the correlation between these results and the evaluation of the morphologies.

Secondly, the charge carrier transfer as major parameter on influencing the photocatalytic efficiency will be discussed, separately. In order to isolate the charge carrier transfer through titanium dioxide, single phase systems are preferred for the study of connections between the structural changes and the dielectric properties.

Thirdly, a detailed defect analysis will be linked with the in-situ X-Ray diffraction measurements for the study of the temperature dependency of the structural changes triggered by the defect distributions.

Fourthly, the validity of the correlation between the defect distribution and the structural changes for single-phase crystalline systems, multi-phase crystalline systems and amorphous phase systems will be studied to open a new manipulation method of transition metal oxides for specific applications.

5.1 SURFACE AREA AND THE PHOTOCATALYTIC ACTIVITY

As mentioned in chapter 2.3, the photocatalytic efficiency of a semiconductor can be influenced by three parameters, the charge carrier formation, the charge carrier transfer and the surface area of the material. In this work, the charge carrier transfer and the surface area are of high interest. Whereas the change in charge carrier formation ability of titanium dioxide is neglected in this work. It is necessary to find a method to distinguish between the influence of the charge carrier transfer and of the surface area during changes in the photocatalytic efficiencies of titanium dioxide. One possible

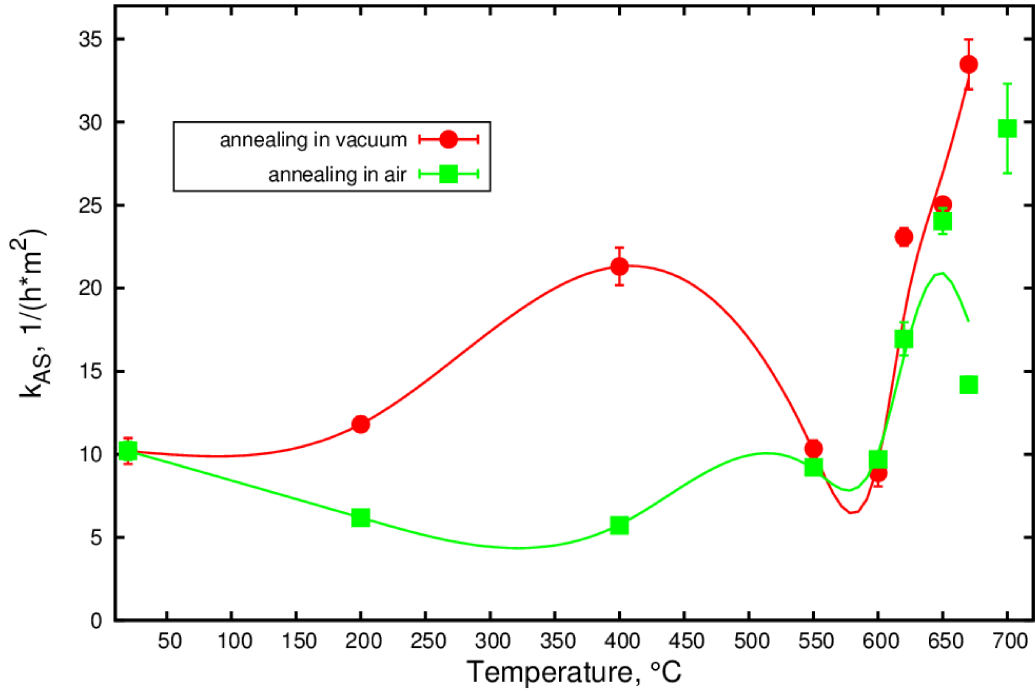


Figure 5.1.1: photocatalytic kinetic constant normed on the specific surface area of the sample, from [51].

way is to normalize the photocatalytic kinetic constant of a sample to its own specific surface area [51]. The normalized photocatalytic constant will be defined by:

$$k_{AS} = \frac{k_A}{A_{BET}} \quad (5.1.1)$$

with the photocatalytic kinetic constant of the anatase phase k_A and the specific surface area A_{BET} .

Adapting equation 5.1.1 on the results of figure 4.2.2 will lead to the normalized photocatalytic constant of the heat treated powders shown in figure 5.1.1. A strong pronounced gap between air and vacuum treated powders at 400 °C followed by a neutralisation at 600 °C is observed. After that the photocatalytic activity increases significantly independently of the surrounding atmosphere. While the improvement of photocatalytic efficiency for powders treated above 620 °C is correlated with a very low amount of anatase phase and a high possibility of newly formed oxygen defects, the strong pronounced gap at 400 °C is considered as mild temperature anomaly [29,40,51]. Focussing on the result achieved for powders treated below 620 °C, the sample with the smallest surface area showed the highest photocatalytic activity. This could mean that the surface area is a minor parameter when it comes to influencing the photocatalytic efficiency of a semiconductor material. So, the major parameter is the charge carrier transfer through the material which is responsible for a low electron-hole recombination

possibility [23, 29]. Nevertheless, the surface changing processes in mild temperature regime are still linked with the photocatalytic efficiency which can be concluded due to the neutralisation at 600 °C in the photocatalytic activity as well as in the surface area.

It could be considered that the strong agglomeration of grains by covalent bonds in reducing atmosphere at 400 °C triggers an high interface formation. These line defects are influencing the lattice point defects, such as oxygen vacancies, and significantly change the charge carrier transfer inside the titanium dioxide.

A second morphology changing process, the anatase to rutile phase transition, prefers to start close to the interfaces, and it will break the covalent bonds [26, 62]. As a result, a gain in surface area is observed leading to the neutralisation of the material and to restore the original photocatalytic properties.

In order to study the influence of the charge carrier transfer in more detail, the resistivity of titanium dioxide is analysed. It is necessary to study the thin-film-system that represents a single-phase system where grain agglomeration is negligible to ensure that changes in the charge carrier transfer can be correlated with the structural changes of the titanium dioxide.

5.2 CHARGE CARRIER TRANSFER ANALYSIS

In order to achieve the requirement of neglecting morphology changes, the analysed titanium dioxide system is a pure anatase thin film. This thin film is prepared by the CC-CVD-method.

In order to understand the changes of the charge carrier transfer ability, the resistivity of the samples is measured in-situ in vacuum for temperatures up to 520 °C. The results are shown in figure 5.2.1. In different titania systems the same anomalies can be observed. The thin film and the pellet sample show resistive switching from insulating configuration to conducting configuration at around 200 °C. Therefore, this breakdown is not correlated with leaking currents because the thin film sample is considered as fully densified. Since the same behaviour is measured in thin films and pellets it is possible to focus on thin films measurements in the following section.

The resistivities of the thin films show a breakdown at 200 °C and a minimum of the resistivity at around 400 °C which could mean that at this temperature the charge carrier transfer proceeds under most probable conditions. The resistivity is close to the resistivity of a metal system and it could be still overestimated because it is assumed that the current flow proceeds through the whole thin film and not only through single channels.

The slope of the resistivity measurement in dependence of the temperature is connected with a large error due to the unique setup used, as it is explained in chapter 4.5.4.

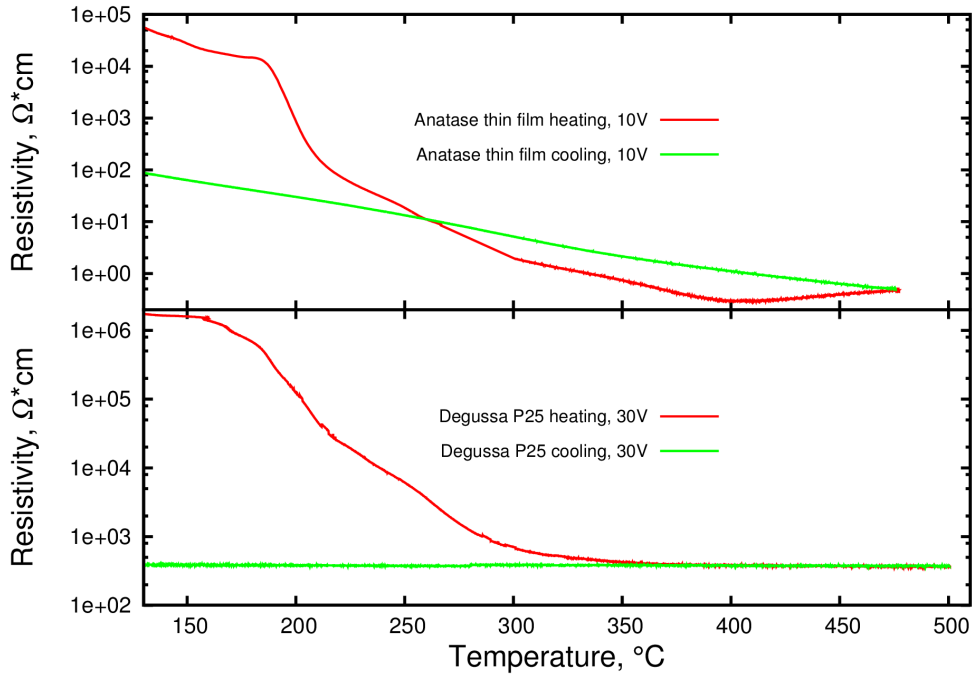


Figure 5.2.1: Resistivity of Degussa P25 pellets and anatase thin films in vacuum ($p \approx 1 \cdot 10^{-5} \text{ mbar}$).

So, it could be valuable to analyse the changes in I-V-characteristics at the anomaly temperatures, directly. Figure 5.2.2 presents these results for the anatase thin film sample. Hysteresis loops with different shapes and slopes can be observed for all samples. The smaller the slope is, the higher the resistivity of the sample is [146,147]. The advantage of the setup is that the I-V-characteristics in the sample can be calculated. As it can be seen in figure 5.2.2, the maximum applied voltage of the source is never measured over the sample because of the reference resistance. So it is possible to study the resistivity switching of the sample and the formation of a polarisation field inside the titanium dioxide, in more detail.

The polarisation field strength inside a solid material is [146]:

$$\vec{P} = \epsilon_0 \overline{\chi_e} \vec{E} = \epsilon_0 \overline{\chi_e} \frac{U}{d} \vec{e} \quad (5.2.1)$$

with polarisation field \vec{P} which is orientated in the opposite direction of the initial electrical field, applied voltage U , distance between the electrodes d , unit vector of the electrical field \vec{e} and the permittivity of the vacuum ϵ_0 .

The electric susceptibility $\overline{\chi_e}$ tensor can be expressed in an homogeneous electrical field by the dielectric constant ϵ_r as $\chi_e = \epsilon_r - 1$ and it depends on the material. The change

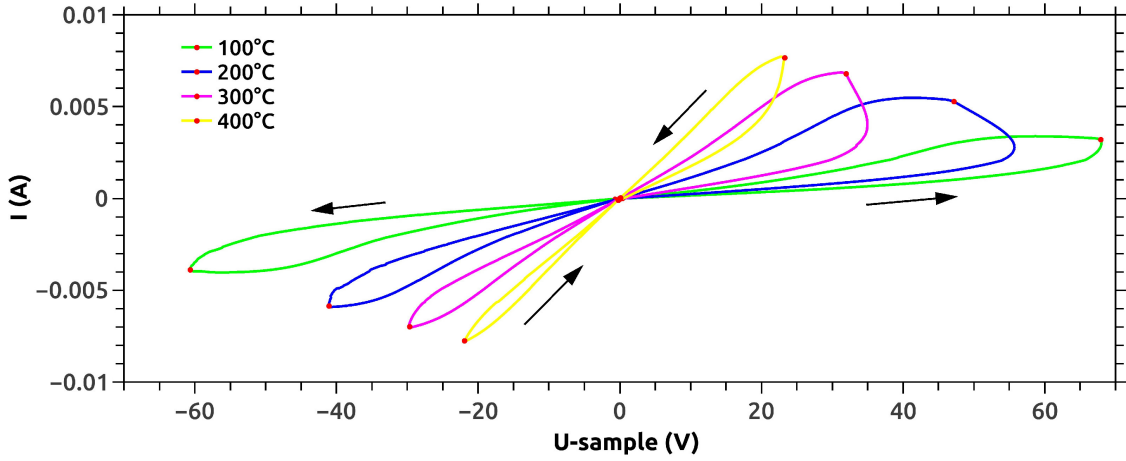


Figure 5.2.2: I-V-characteristics of the anatase thin film at anomaly temperatures in vacuum ($p \approx 1 \cdot 10^{-5} \text{ mbar}$) and a reference resistance of $1 \text{ k}\Omega$. The red dots marking the limits of applied source voltage $U_{source} = \pm 100 \text{ V}, 0 \text{ V}$. The black arrows marks the direction of the hysteresis, which is from insulating state to conducting state in every measurement.

of this parameter is expressed by:

$$\Delta\epsilon_r = \Delta\epsilon_i + \Delta\epsilon_e \quad (5.2.2)$$

with intrinsic effects that changes the permittivity such as creating permanent dipoles $\Delta\epsilon_i$ and external effects such as breakdown effects through pores $\Delta\epsilon_e$ [148,149]. External effects in changing the susceptibility are neglected because of the chosen analysed system.

It is possible to understand the voltage over the sample U_{sample} in the I-V-characteristics as:

$$\frac{U_{sample}}{d} \vec{e} = \epsilon_0 \vec{E} - \vec{P} = \epsilon_0 \frac{U_0}{d} (1 - \overline{\chi_e}) \vec{e} \quad (5.2.3)$$

with the applied voltage $U_0 = U_{source} - U_R$ including the voltage of the power supply U_{source} and the voltage measured over the reference resistance U_R . Derived from equation 5.2.3, the change of the applied voltage over the sample for every measurement step is:

$$\Delta U_{sample} \vec{e} = \epsilon_0 \Delta U_0 (1 - \Delta \overline{\chi_e}) \vec{e} \quad (5.2.4)$$

Adapting equation 5.2.4 on the measurement curve will result in the following behaviour of the I-V-characteristics:

$$\Delta U_0 > 0 \rightarrow \begin{cases} \Delta \overline{\chi_e} \circ \vec{e} = 0 \rightarrow 0 < \Delta U_{sample} = \Delta U_0, \\ \Delta \overline{\chi_e} \circ \vec{e} < 1 \rightarrow 0 < \Delta U_{sample} < \Delta U_0 \\ \Delta \overline{\chi_e} \circ \vec{e} > 1 \rightarrow \Delta U_{sample} < 0 \end{cases} \quad (5.2.5)$$

In the measured curve the different cases are presented as linear curve for $\Delta\overline{\chi}_e \circ \vec{e} = 0$, as curvature with positive slope for $\Delta\overline{\chi}_e \circ \vec{e} < 1$ and as curvature with negative slope for $\Delta\overline{\chi}_e \circ \vec{e} > 1$. There is no time left between each measurement step for relaxation. This means, the dynamic process behaviour is analysed.

According to this theory, two different structural changes can be observed during the measurement of the I-V-curve. Firstly, the formation of dipole moments inside the material which is indicated by the transition from a linear I-V-curve to a curvature with positive slope. In this case, the initial dielectric material is changed into a material with para-electric properties. From the classical point of view, the crystal structure of para-electric materials is well defined. It is necessary to be in a non-point-symmetrical crystal structure [150–152]. Since this is not defined for titanium dioxide crystal structures, the para-electric properties are caused by the defect structure. Therefore, the material will be called quasi-para-electric material in the following discussion.

Secondly, the alignment of these dipoles due to the applied external electrical field which leads to an enlarged polarisation field inside the titanium dioxide thin film. This process could be triggered by structural properties. For example it could require a minimum external electrical field to overcome mechanical limits during the alignment of the dipoles.

Inside the anatase thin film prepared by CVD method, a dependency of temperature and external field strength can be observed, presented in figure 5.2.2. While at 100 °C an insulating state could be considered, there are no further anomalies observable. There is no strong resistive switching and no strong change in the susceptibility indicated. Furthermore, the measured hysteresis is symmetric showing a reversibility of all processes, such as forming of non-permanent dipoles [32, 121, 124].

The I-V-characteristics in the temperature range of the resistive anomalies show non-symmetrical hystereses. A 'negative' resistance can be observed in the sample at 200 °C and 300 °C. In this case, the voltage over the sample decreases with increasing overall voltage and an increasing current is measured. These are the areas with negative slope. In this case, the change in the polarisation field strength inside the titanium dioxide is larger than the change of the external electrical field strength. It can be suggested that at temperatures above 200 °C, dipoles can be formed leading to a quasi-para-electric defective titanium dioxide. The alignment of these dipoles triggers a structural transition which opens conductive channels inside the thin film. In this moment, the anatase has a significantly lower resistance. The I-V-loop at negative applied external voltages begins with a stronger slope compared to the positive loop. This means that the original resistance is not restored and the formed dipoles are permanent and the material is still quasi-para-electric. This also explains the stronger curvature of the starting negative loop compared to the positive one.

At elevated temperatures, these asymmetrical hystereses are still present but the part



Figure 5.2.3: Photography of a titanium dioxide thin film sample after the resistivity measurement in vacuum from the front (left) and the rear (right). The electrical field was applied tangential to the surface between two electrodes. The third electrode is a blind electrode which was not connected.

with the negative slope due to the high initial conductivity of the material is missing.

The analysis of the I-V-characteristics in dependency of the temperature shows that the measured anomalies in the resistivity at 200°C are correlated with permanent dipole formation and alignment that trigger structural changes inside the anatase film causing highly conductive channels. A photography of an analysed film is shown in figure 5.2.3. The anatase thin film was prepared with three silver electrode while one of those is a blind electrode. The photography proofs that the conductive channels are highly orientated because the colour change of the anatase thin film is only between the contacted electrodes. Furthermore, a change to black colour can only be observed below the connected electrodes.

5.3 QUASI-PARA-ELECTRIC TiO_2 AND ITS CRYSTAL STRUCTURE

The analysis of the surface near states of titanium dioxide showed that neither the chemical composition nor the surface near defect structure explains the conductive switching inside titanium dioxide thin films during vacuum heat treatment. The chemical composition presented in figure 4.3.1 and in table 4.3.1 proofs that no foreign elements are included inside the film. Only titanium, oxygen and carbon can be detected. The detected carbon can be explained by adsorbing organic molecules after the sample is exposed to air which would mean that the thin film after the resistivity measurement shows an improved adsorption ability.

The determination of the defect structures close to the surface is presented in table 4.3.1. No significant changes can be observed. This indicates a low amount of oxygen lattice vacancies and a low amount of Ti^{3+} -species in the anatase black film on quartz, but this can be explained by the lower information depth because of the thicker organic layer on the surface. Nevertheless, it seems unlikely that a significant amount of surface

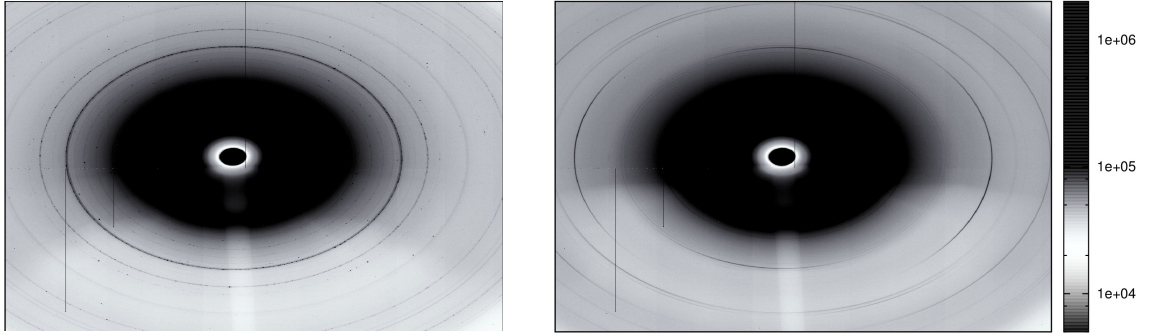


Figure 5.3.1: 2D-detector image of titanium dioxide thin film samples prepared by CVD method. The thin films are treated in vacuum ($p \approx 1 \cdot 10^{-6} \text{ mbar}$) up to 550°C . The conductive sample (left) and its insulating satellite sample, (right).

oxygen vacancies is created because of the high ratio of structural oxygen to titanium $\frac{O_{\text{struc}}}{Ti} > 2$ in the thin film samples. This confirms the known statement that anatase prefers to form bulk defect states instead of surface defect states [44].

Therefore, structural changes have to trigger the resistive switching and the formation of a quasi-para-electric state of titanium dioxide. The domain of this structural change can be in the crystallite range as well as in the grain range. The crystallite range is analysed by X-ray-diffraction experiments at the P07 beamline in DESY, Hamburg.

The 2D-detector images of anatase thin film in insulating state and in a stable conductive state are presented in figure 5.3.1. Significant structural differences can be observed in these detector images. While the insulating titanium dioxide thin film data shows peaks at the positions of the anatase main peaks [130], the intensity of these peaks is low and a strong amorphous background from the silica glass is detected. Nevertheless, a pure anatase phase is included with a strong texture due to the growth process during the CVD-syntheses.

The black thin film shows a stronger crystallisation which is indicated by the higher signal to noise ratio. On one hand, this crystallisation can be explained by the exposing temperature of 550°C . On the other hand, it is influenced by the applied external electrical field. The anatase main peak in (110)-direction did not change its texture properties compared to the original thin film. But there are rings with higher intensity observed. For example the anatase (004)-reflection. This ring has a high intensity and is also strongly textured which can be seen in more intensive parts, indicating a single crystallite.

More details can be seen in figure 5.3.2. The rings are showing strong deviations over the whole integrated area. These deviations indicate that a strong mechanical stress is induced inside the crystal structure via applying an external electrical field. Although, the main anatase crystallites are symmetrically placed on the intensity ring whereas the (004)-crystallites are shifted to larger angles. It could be considered that the lattice parameters of these crystallites are smaller than the ones for the original

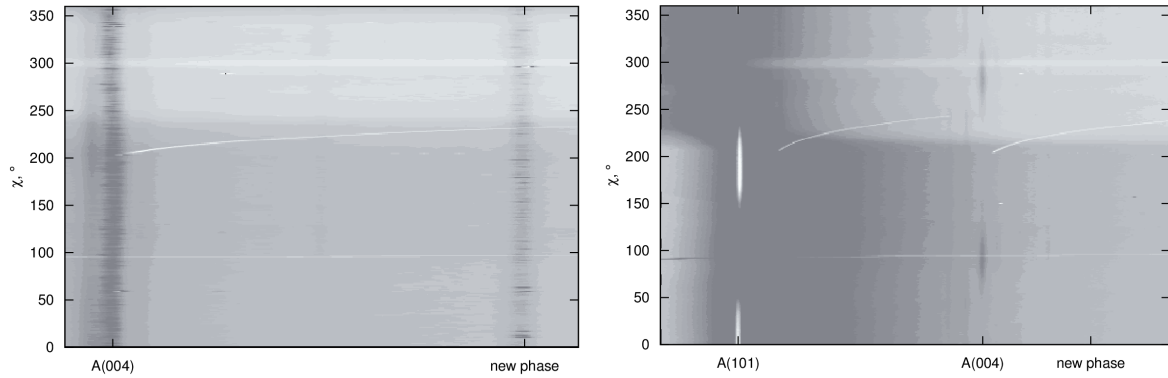


Figure 5.3.2: Integration over the χ -angle of the 2D-images of conductive titanium dioxide thin film (left) with the focus on anatase-(004)-reflex and the reflex of the new phase. Integration over the χ -angle of the 2D-images of the insulating titanium dioxide thin film (right) with focus on the A(101)-reflex and the A(004)-reflex.

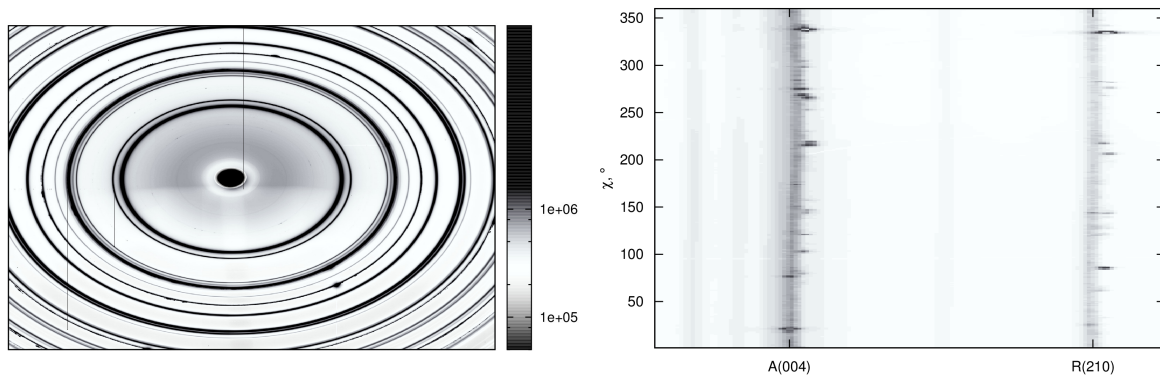


Figure 5.3.3: 2D-detector image (left) of black Degussa P25 pellet and the map plot as Integration over the χ -angle (right) of the 2D-images of the black Degussa P25 pellet with the focus on anatase-(004)-reflex and the rutile-(210)-reflex (left). The position of rutile-(210)-reflex is similar to the position of the reflex of the new phase in the conductive anatase thin film.

anatase phase. Smaller lattice parameters are caused by lattice vacancies. So the (004)-crystallites could include oxygen lattice vacancies.

Additionally, some new reflections are observed. They are not linked with brookite or rutile [131, 134] which means there could be a new titanium dioxide phase occurring which causes the conducting state. Because of the strong amorphous background of the quartz glass a quantitative analysis is omitted.

Therefore, the analysed system is again changed. Instead of anatase thin films Degussa P25 is studied. The results of activated P25 I-V-characteristics, figure 5.4.2, prove that this very titanium dioxide system shows the same transition to a para-electric-configuration which also improves the conductivity, drastically. Due to its powder shape, it is possible to analyse the structure as well as the morphology which allows a distinction between the effects in the crystallite domains and in the grain domains.

The 2D-Detector image of the conducting Degussa P25 pellet shows the same anoma-

lies like the black thin film samples. The insulating sample is characterised by typical powder diffraction patterns of non textured intensity rings. In contrary, the conducting sample shows strong texture in the anatase-(004)-, the rutile-(210)- and the rutile-(310)-reflex. The textured crystallites are non-symmetrical placed on the original ring with the tendency to higher angles which means that the lattice parameters are smaller in this textured titanium dioxide.

The calculation of the lattice parameters via Rietveld Refinement for the original titanium dioxide phase and the textured titanium dioxide phase after integration over the whole ring, shown in figure B.2, yields the following averaged changing vectors in:

$$\vec{A} = \begin{pmatrix} 0 \\ 0 \\ -0.0624 \end{pmatrix} \text{ \AA} \quad \vec{R} = \begin{pmatrix} -0.0264 \\ -0.0264 \\ 0.0031 \end{pmatrix} \text{ \AA}$$

with the changing vector of anatase unit cell \vec{A} und rutile unit cell \vec{R} . Calculated by VESTA [41], these changing vectors cause an average shrinking of 0.026 Å in the top-to-top axis and no change in the diagonal plane length of the anatase octahedron and a average shrinking of 0.023 Å in the top-to-top axis and 0.009 Å in the diagonal plane length of the rutile octahedron. So the main direction of the change is in the top-to-top oxygen axis which means that it is possible that mainly such a top-site contains a lattice oxygen vacancy inducing a dipole moment. Theoretical calculations predict a minimum in the formation energy for a lattice oxygen vacancy at top-sites in titanium dioxide octahedrons [44, 153].

In order to study the temperature dependency of the formation of textured defective titanium dioxide phases, an in-situ study is performed. The structure of Degussa P25 pellets is evaluated by measuring XRD-patterns during heating the pellet in vacuum atmosphere while applying an external electrical field.

The results are shown in figure 4.7.3 in the results section and they present an intensity mapping of Degussa P25 pellets measured with and without an applied electrical field, on the edge and on outside of the electrode and with different field distribution. In both cases with an external electrical field, newly formed crystalline phases could be detected compared to the sample measured without an applied electrical field. Rietveld refinement, figure 4.7.4, showed that neither silver(-oxide) nor brookite could explain these new phases.

The focus now will be on the structural evaluation of the Degussa P25 pellet with an electrical field normal to the surface. For this sample, the measurement spot was in approximately 1.5 mm distance to the edge of the silver electrode. In this sample, the new foreign phase is characterised by four new reflections, with one reflection close to the rutile (210)-reflex in the measurement pattern. They appeared with shallow inten-

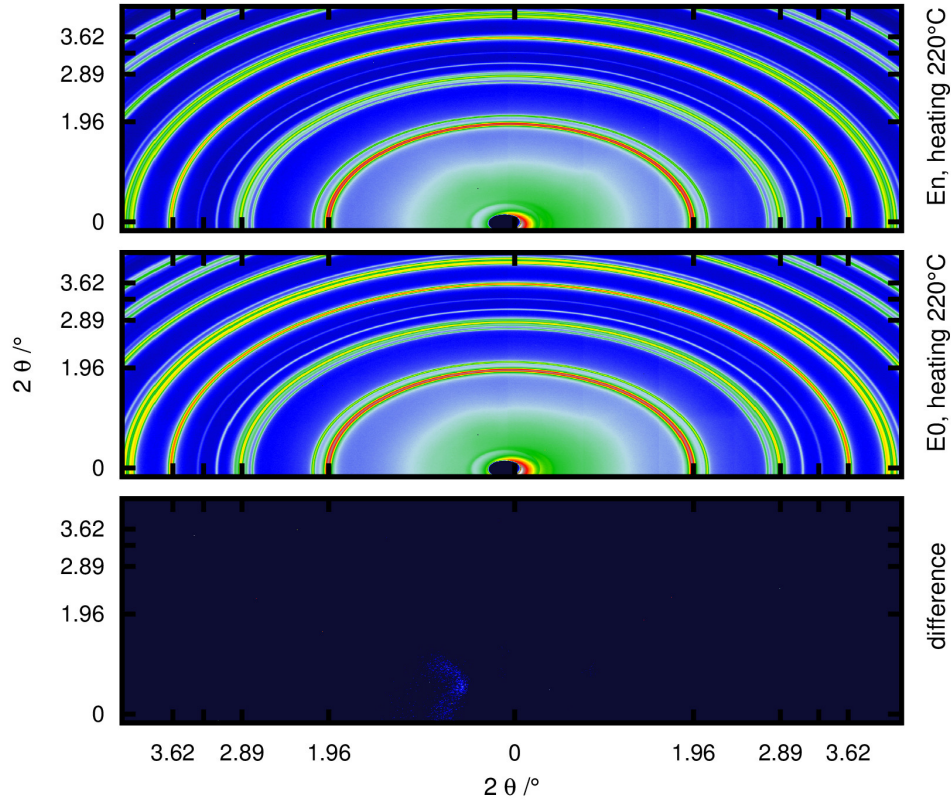


Figure 5.3.4: Difference plot between XRD 2D-detector image of a Degussa P25 pellet with an external electrical field applied normal to the surface (En) and a Degussa P25 pellet without an external electrical field (E0) measured in vacuum $p \approx 1 \cdot 10^{-4} \text{ mbar}$ at 220°C during heating. The intensity is in logarithmic scale. The limits of the intensity of the difference I_{diff} in dependency of the maximum intensity of the original measurement I_{max} is: $0.002 \cdot I_{max} < I_{diff} < 0.2 \cdot I_{max}$, modified from [42].

sity at room temperature in vacuum of $p \approx 1 \cdot 10^{-4} \text{ mbar}$ and disappeared at 180°C . At 300°C this same phase crystallises again at slightly lower angles and start growing significantly with increasing temperatures. The peaks disappear again during heating at 550°C and were never observed during cooling.

In order to proof that this new phase is correlated with the measured textured defective anatase and measured textured defective rutile phase in the black titanium dioxide samples, the 2D-patterns are studied in more detail. The intensities of the reflections of the new formed phase inside the sample treated in vacuum with an electrical field normal to the surface seem to be similar over the whole ring which means that the crystallites have no preferred orientation. In order to see more details of the X-ray patterns, the data is analysed by subtracting an 2D-pattern from a reference measurement. In this way, smallest differences inside the high intensed rings can be observed. An example is shown in figure 5.3.4. It contains the 2D detector image of a Degussa P25 pellet during in-situ measurements in vacuum at 220°C . As reference material the Degussa P25 pellet without an electrical field applied at the same temperature is

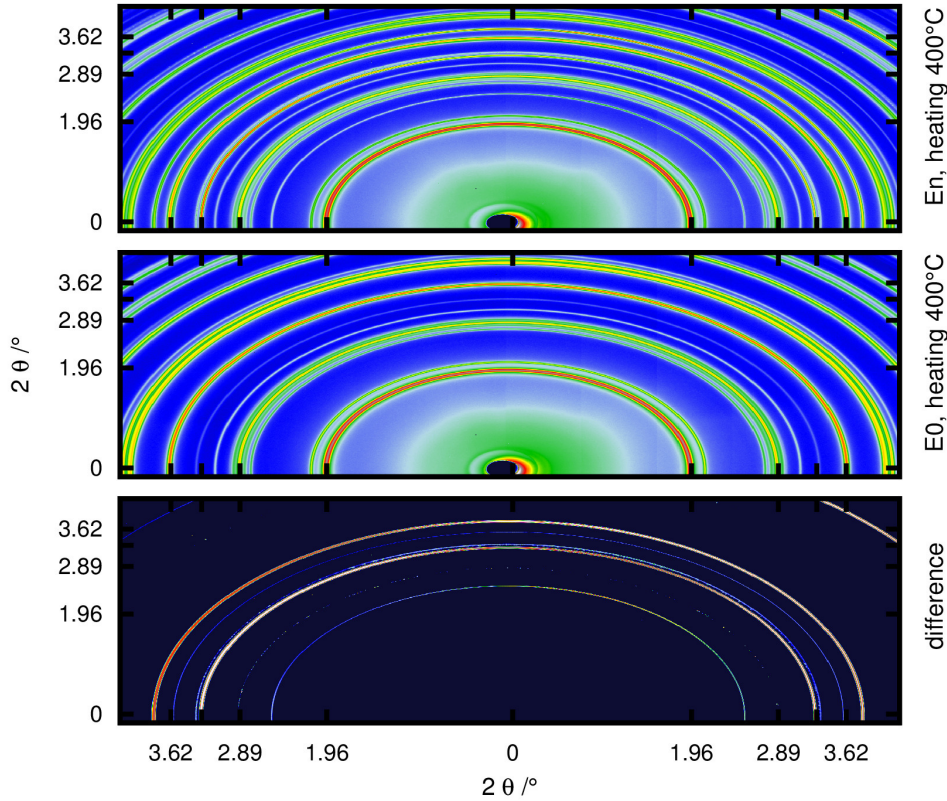


Figure 5.3.5: Difference plot between XRD 2D-detector image of a Degussa P25 pellet with an external electrical field applied normal to the surface (E_n) and a Degussa P25 pellet without an external electrical field (E_0) measured in vacuum $p \approx 1 \cdot 10^{-4} \text{ mbar}$ at 400°C during heating. The intensity is in logarithmic scale. The limits of the intensity of the difference I_{diff} in dependency of the maximum intensity of the original measurement I_{max} is: $0.02 \cdot I_{max} < I_{diff} < 0.2 \cdot I_{max}$, modified from [42].

chosen. The difference plot proves that these two samples show no significant difference between each other. At this temperature, close to the on-set temperature of the resistive switching in titanium dioxide systems, no structural changes can be observed when an external electrical field is applied.

Therefore, difference plots between P25 pellet measured in-situ in vacuum with an external electrical field applied and a P25 pellet measured in-situ in vacuum without an external electrical field are analysed in order study the correlation between charge transfer anomalies and structural changes.

A resistivity minimum could be observed at 400°C , therefore, the difference plot at this temperature during the heating process is presented in figure 5.3.5. In the mapping, figure 4.7.3, this measurement shows high intensities for the arminias phase, a defective pseudo titania phase. This phase can be identified by newly occurring X-ray diffraction rings which are strongly pronounced in the 400°C difference plot. The rings are observable over the whole χ -angle but they indicate the beginning of a texture due to the higher difference intensity on the right side of the plot. Additionally, small

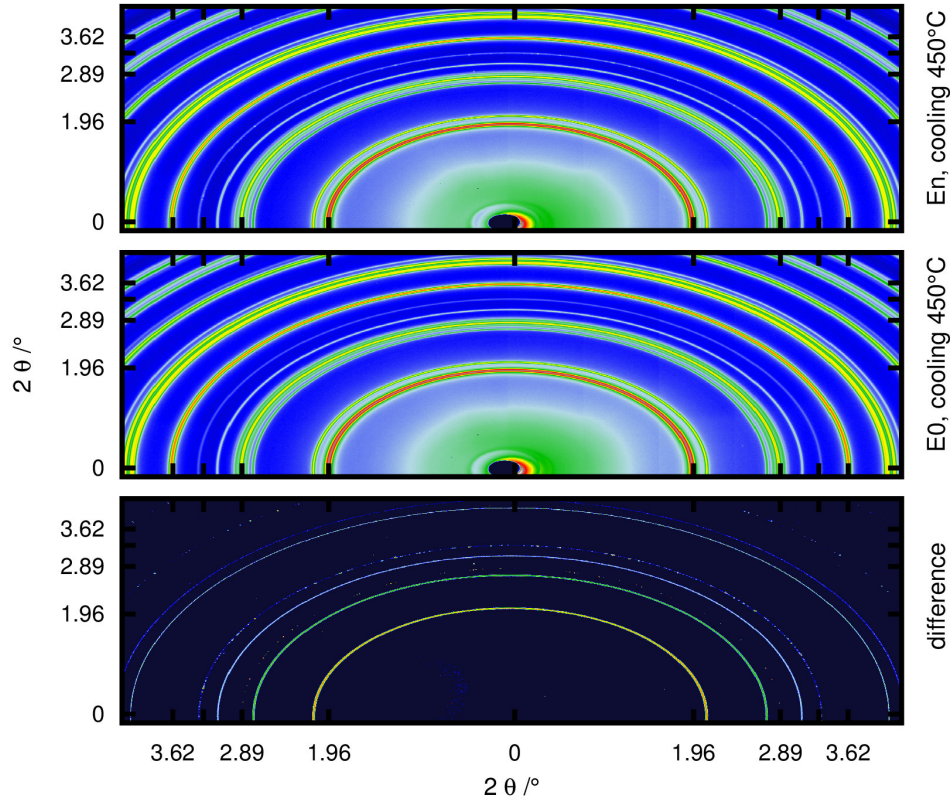


Figure 5.3.6: Difference plot between XRD 2D-detector image of a Degussa P25 pellet with an external electrical field applied normal to the surface (E_n) and a Degussa P25 pellet without an external electrical field (E_0) measured in vacuum $p \approx 1 \cdot 10^{-4} \text{ mbar}$ at 450°C during cooling. The intensity is in logarithmic scale. The limits of the intensity of the difference I_{diff} in dependency of the maximum intensity of the original measurement I_{max} is: $0.02 \cdot I_{max} < I_{diff} < 0.2 \cdot I_{max}$, modified from [42].

crystallites are included in this sample which leads to the dotted structure in the X-ray diffraction rings at $2\theta = 2.89^\circ$ and $2\theta = 3.24^\circ$. They are identified as the anatase (004)-reflection and the rutile (210)-reflection [130,131]. This could support the theory that permanent dipoles are formed, preferentially in anatase (004)-direction, leading to defective crystallites. They are aligned in an external electrical field and when the defect density and the dipole density exceed up to a critical value a new pseudo titania phase, arminiase, can be detected.

While the new titania phase seems to disappear with the beginning of the phase transition from anatase to rutile at 550°C in these samples, the Degussa P25 pellet stays in a conductive configuration. The difference plot at 450°C during the cooling, presented in figure 5.3.6, examines that the dipole centres are still detectable. On one hand, the non-textured diffraction rings are without exception identified as rutile reflections which can be explained by the starting anatase to rutile transition at the maximum temperature [26,62]. On the other hand, the anatase (004)-reflection with textured structure is also detectable, however, much weaker than during the heating

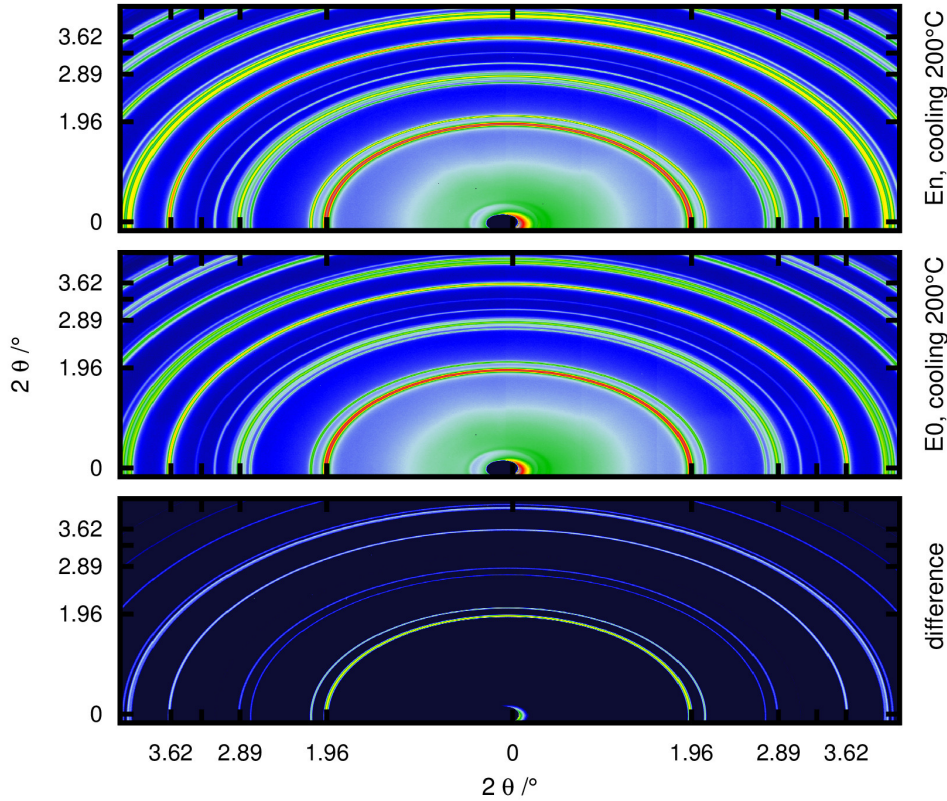


Figure 5.3.7: Difference plot between XRD 2D-detector image of a Degussa P25 pellet with an external electrical field applied normal to the surface (E_n) and a Degussa P25 pellet without an external electrical field (E_0) measured in vacuum $p \approx 1 \cdot 10^{-4} \text{ mbar}$ at 200°C during cooling. The intensity is in logarithmic scale. The limits of the intensity of the difference I_{diff} in dependency of the maximum intensity of the original measurement I_{max} is: $0.02 \cdot I_{max} < I_{diff} < 0.2 \cdot I_{max}$, modified from [42].

and the rutile (210)-reflection is strongly textured. Therefore, defective crystallites are still included inside the material.

Because of the lower vacuum and the low electrical field applied, a re-switching in insulating configuration below 250°C is observed. The difference plot for the samples at 200°C during cooling shows that there is no texture detectable anymore in any diffraction ring. The observed rings are identified as anatase and rutile reflexes, no further phases are detected. This means that the conductive configuration of titanium dioxide is correlated directly with the presence of defective crystallites which will form electrical dipoles.

In the last step, the crystallite growth is analysed by comparing a higher temperature sample with a lower temperature one with the same electrical field configuration. The difference between 400°C and 300°C for the sample with an external electrical field is shown in figure 5.3.8. In both cases, the sample is already in the conductive configuration. The difference plot shows that in the anatase-(004) and rutile-(210) reflexes there are nearly no changes, whereas the arminias phase is growing. Comparing the

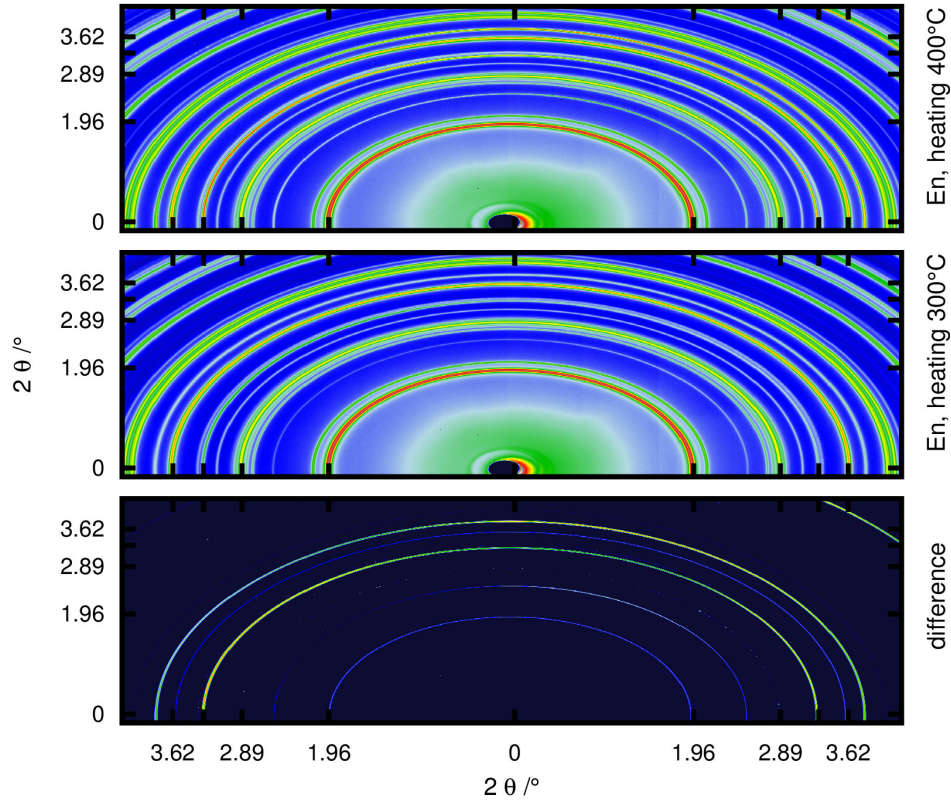


Figure 5.3.8: Difference plot between XRD 2D-detector image of a Degussa P25 pellet with an external electrical field applied normal to the surface (E_n) at 400°C and at 300°C during heating. The intensity is in logarithmic scale. The limits of the intensity of the difference I_{diff} in dependency of the maximum intensity of the original measurement I_{max} is: $0.02 \cdot I_{max} < I_{diff} < 0.2 \cdot I_{max}$, modified from [42].

arminiase distribution in the original 2D-plots illustrates that the growth of the arminiase phase from 300°C to 400°C leads to a more statistically distribution of the new phase. That means that a more inhomogeneous electrical field distribution inside the titanium dioxide pellet occurs and supports a wider spread of the new pseudo titania phase.

In summary, XRD measurements underline a significant structural difference between insulating and conducting titanium dioxide thin films as well as in titanium dioxide powders. This demonstrates the formation of a quasi-para-electric configuration in crystal domain size by crystallisation of defective anatase and defective rutile crystallites. Furthermore, the in-situ experiment illustrates that the alignment of newly formed dipoles opens conductive channels and could form a new titanium dioxide phase. The defective anatase and defective rutile crystallites acting as crystallisation centres for this new arminiase phase by changing the density distribution close to the discussed lattice planes [154, 155]. An inhomogeneous electrical field distribution inside the material due to a better conductivity leads to a reduction of the arminiase texture characteristic.

5.4 DEFECT STRUCTURE AND CRYSTAL STRUCTURE

While photocatalytic activity measurements and resistivity measurements illustrate the consequences of the defective crystal structure, XPS analysis and EPR measurements should characterise the nature of the defects being necessary for mild temperature anomalies.

The XPS results, presented in figure 4.3.2 and in table 4.3.1, make clear that no strong reduction could be observed in any sample, neither in quasi in-situ treated pellets nor in black titanium dioxide systems. Especially, the black system includes low Ti^{3+} -sites as well as a ratio of $\frac{O_{\text{structural}}}{\text{Ti}} \approx 2$ which demonstrates that the equation 5.4.1 [33,34,38]:

$$\text{Ti}_{1-x}\text{O}_{2-y} \quad , \quad x \leq 2y \quad , \quad y < 0.1 \quad (5.4.1)$$

is valid for the black samples.

Despite the surface sensitivity of the XPS method, it can be stated that there is no strong reduction in the black powder sample due to the statistical distribution of crystals inside powder samples.

The EPR method provides the opportunity to distinguish between lattice vacancy defects V_O and reductions caused by interstitial defects Ti^{3+} due to the different Lande-factors g of these defect sites. Furthermore, measurements at different temperatures can indicate the localisation of the lattice position of a defect. Highly de-localised lattice defects can be characterised by a small FWHM of the signal peak and by a missing signal at room temperature because of the fast relaxation ability of this defects.

The EPR results of simply heat treated Degussa P25 powders at 100 K, presented in figure 4.6.2, revealed a redistribution of the present defects. They change from de-localised lattice defects in the powder treated at 220 °C in vacuum to localised electron and hole trapping sites [29] in powder treated at 400 °C in vacuum. Furthermore, after this treatment lattice oxygen vacancies could not be detected. The defects in the sample treated at 400 °C are localised on interfaces, especially, the hole trapping sites. In connection with the surface area measurements, it can be stated that the loss in surface area due to grain agglomeration leads to a high amount of interfaces. Crystalline-crystalline-interfaces of different phases are described as a rigid amorphous fraction which links the two different crystals. The covalent bonded oxygen inside this rigid amorphous fraction is called bridging oxygen and has the highest possibility of forming an oxygen vacancy [44]. This vacancy is also highly localised cause it is placed inside this interface. The EPR results unveil that at 400 °C the reduction of the titanium dioxide is characterised by such oxygen vacancies acting as hole trapping sites.

The spectra of different titanium dioxide systems presented in figure 5.4.1 underline this theory because the resonance in the hole trapping area is detected for black pow-

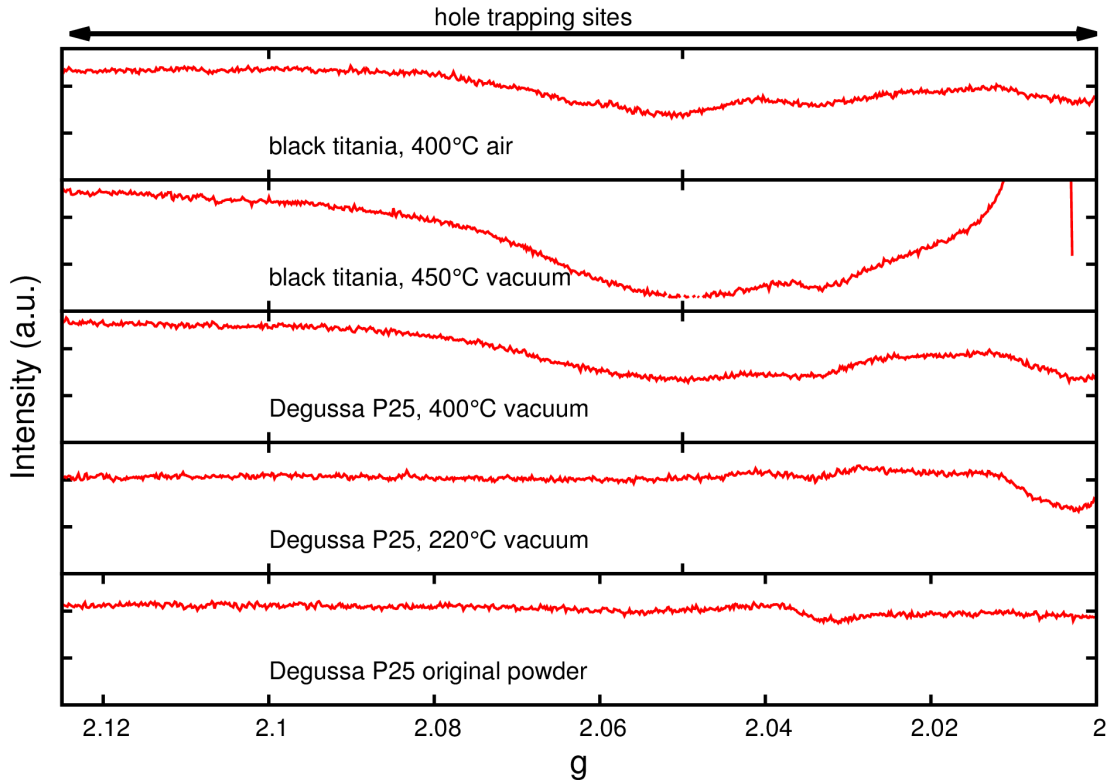


Figure 5.4.1: EPR spectra of Degussa P25 powder and black titania powders before and after calcination in air at room temperature with focus on the hole trapping sites close to interfaces.

ders and powders treated at 400 °C to be like the in measurements at 100 K.

If the bridging oxygen of the rigid amorphous fraction is also an oxygen atom at the top-to-top axis of a titania octahedron, then a periodical alignment along the grain boundary is possible. There is a probability of the formation of defective mono-crystallites which could be the defective anatase-(004) and rutile-(210) crystallites documented in the X-ray diffraction measurements. Furthermore, the localisation on grain boundaries would also lead to a high mechanical stress for these mono-crystallites causing a displacement along the χ -angle of the diffraction pattern as it is shown in figure 5.3.2.

The electron overflow during the resistivity measurements which lead to the black colour also causes a significant increase of lattice oxygen vacancies and Ti^{3+} -sites compared to simply heat treated powders.

Each one of these described effects, especially, the possible formation of defective mono-crystals are based on oxygen vacancies. This is proven by air calcination of the black titania powder. On one hand, this powder turned white on the other hand, the EPR results at 100 K as well as at room temperatures show a significant lower amount of each defective site. Lattice oxygen vacancies and Ti^{3+} -sites and hole trapping sites localised at interfaces are hardly observable.

In summary, the heat treatment in vacuum of titanium dioxide samples in combina-

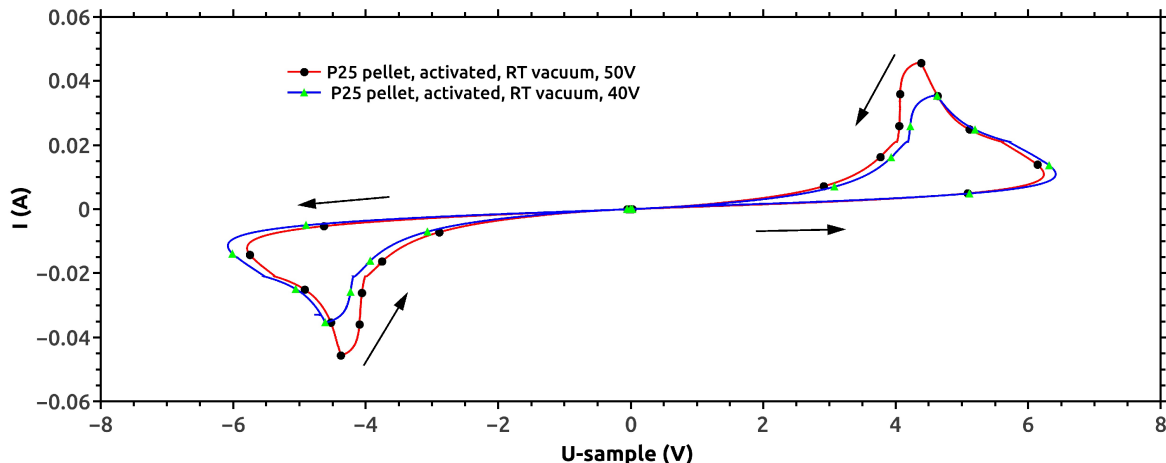


Figure 5.4.2: I-V-characteristics of activated Degussa P25 pellets in vacuum ($p \approx 1 \cdot 10^{-5} \text{ mbar}$) and a reference resistance of $1 \text{ k}\Omega$ for different maximum external applied voltage. The symbols marking 10 V steps of applied source voltage. The black arrows marks the direction of the hysteresis, which is from insulating state to conducting state in each measurement [42].

tion with an external electrical field causes a highly defective structure and a colour change from white to black. The defective structure is characterised by oxygen vacancies in the top-to-top positions inside the original octaherons. EPR measurements at room temperature proves that these lattice defects can act as charge carrier trapping sites and are highly localised. The possibility to pin the charge carrier trapping sites is maximised in the rigid amorphous fraction close to line defects. Therefore, the pinning of such trapping sites is probable in Degussa P25 powders due to the two phase system and the grain agglomeration during vacuum treatment. Furthermore, a new crystalline phase, arminiase, is observed during in-situ measurement since the density distribution in the (004)- and (210)-direction is changed due to lattice defects and form a new periodical structure with para-electric characteristics. The crystallisation temperature is approximately 300°C .

A Degussa P25 pellet is activated by calcination in vacuum with an external electrical field applied up to 300°C followed by the measurement of the I-V-characteristics at room temperature to examine this very working hypothesis. The results are shown in figure 5.4.2. Similar to the anatase thin film samples the resistive switching due to conductive channels caused by the alignment of dipoles is observable. Moreover, this process is completely reversible. This means the conductive configuration is only depending on the absolute voltage of the external electrical field but independently of the direction of the electrical field. The quasi-para-electric configuration based on the arminiase-centres is stable at room temperature in reducing atmosphere and can be aligned in both directions. Since arminiases ionic properties the enhanced charge carrier transfer could be caused by an improved polaron based conductivity [156,157].

Chapter 6

Conclusion

Several titanium dioxide systems were characterised by unique in-situ methods. A commercial titanium dioxide powder, a sol-gel-based titanium dioxide powder and a CVD-based titanium dioxide thin film were analysed in oxygen rich and oxygen poor atmospheres with respect to their surface area, resistivity, crystal structure, chemical composition and lattice defect distribution. While they were all consisting of different initial crystal structures, such as anatase, rutile and amorphous structure, similar anomalies could be observed in their electrical properties and their morphology changes at temperatures below the phase transition temperatures. A correlation of these mild temperature anomalies and the lattice defect distribution was discussed.

Degussa P25 powder, a commercial titanium dioxide powder was used as reference material. The heat treatment of this samples in various atmospheres and at various temperatures revealed an anomalous behaviour of its morphology which highly influences the photocatalytic activity of the material. Despite a significantly lower surface area, the sample treated at 400 °C in vacuum improves its overall photocatalytic activity by nearly 20 % compared to the reference material. On one hand, it could be proven that the external surface area is a minority parameter while improving the photocatalytic activity. On the other hand, the charge carrier transfer through the material, the major parameter, showed a maximum in photocatalytic efficiency for Degussa P25 powders treated between 200 °C and 400 °C in vacuum. That layed the focus of this work at the charge carrier transfer ability of several titanium dioxide systems.

Nitrogen adsorption was used to investigate the surface area of each powder samples. EDX, XPS and EPR-measurements were performed to characterise the chemical composition and defect structure, respectively. Additionally, the charge carrier transfer characteristics and its correlation to structural changes of each titanium dioxide system were analysed by performing in-situ resistivity measurements on a own build experimental setup as well as I-V-characteristics performed by a slightly modified setup.

While the mild temperature anomalies of the resistive behaviour was neutralised in oxygen rich atmosphere, a conductive switching was observable in vacuum for each

titanium dioxide system.

The XPS-analysis showed that the pure amount of defects inside the titanium dioxides was not increased drastically. Although, natural defects are always present and the heat treatment triggers a diffusion process.

The diffusion of lattice defects during calcination in a reducing atmosphere lead to the redistribution of such defects and the formation of charge carrier trapping sites localised at grain boundaries, shearing lines or other interfaces confirmed by EPR-measurements. The alignment of such trapping sites caused anisotropically conductive channels and the conductive switching behaviour between 200 °C and 300 °C.

I-V-characteristics showed that these channels are caused by the alignment of newly formed dipoles. Moreover, in two-crystalline-phase titanium dioxide systems these channels are stable at room temperature and can be opened or closed by an external electrical field with high reversibility. This confirmed that significant dipole moments are formed due to a new defect distribution and changed the titanium dioxide systems from a dielectric configuration to a quasi-para-electric configuration.

Furthermore, during the in-situ synchrotron experiments the presence of unknown reflexes was observed with the beginning of the resistive switching process. The analysis of phase transition behaviour, chemical composition and electrical properties confirmed the formation of a new titanium dioxide based para-electric phase. An auxiliary phase, arminiase, was constructed to make a quantitative analysis possible. The arminiase-centres could be understand as defective titanium-oxide-polyhedra localised in a rigid amorphous interface area which were aligned in an external electrical field forming a periodical highly textured structure.

Lattice defects allows inter-gap-states inside the band structure of the semiconductor and leads to an overlap of the defective states inside the conduction band(n-type doping) and the defective states inside the valence band(p-type doping). The redistribution of lattice defects in vacuum during annealing causes the formation of conductive channels, possibly, due to this band structure overlapping.

A density redistribution caused by the alignment of the dipoles and the formation of anisotropic conductive channels is understand as arminiase-crystallisation-centres. The crystallisation of arminiase itself stabilises these conductive channels during further annealing in vacuum. The ionic nature of the auxiliary phase provides the possibility of a polaronic effect. In this case, the electron-phonon interaction inside a ionic crystal lattice leads to a strongly enhanced conductivity through the bulk material.

As a result, the polaronic active titanium dioxides with a higher density of states inside the band gap are expected to show tremendous changes in their photocatalytic properties. The new density of states will allow to use a wider spectrum of the incident light. Considering these photo-induced charge carriers interacting with natural phonons of the crystalline lattice, the charge carrier transfer will be enhanced and a

significantly higher amount of charge carriers can diffuse to the surface and improve the photocatalytic efficiency.

It is important to mention that a significant higher amount of free charge carriers formed arbitrary inside the titanium dioxide also leads to a higher recombination possibility and decreases the photocatalytic efficiency. Hence, it is not clear yet, how the new titanium dioxide phase will influence the water purification process of the photocatalytic reactor now.

It is expected that it is probable to benefit from the enhanced charge carrier transfer of the titanium dioxides and eliminate the parasitic effects.

For example, the fact that it is possible to create a titanium dioxide system which shows polaronic effects will make this newly invented system feasible for further application, especially in combination with the patented reactor design. The design of functional gradient materials from titanium dioxide thin films with improved polaronic effects to originally used titanium dioxide thin films can provide a more controllable charge carrier trapping and cause localised plasmonic behaviour. This will not only improve the water purification process it will also be an alternative to non-metal plasmonic TiO_2 - MoS_2 -systems currently used for hydrogen generation from photocatalytic driven hydrolysis of water [158].

That means, that during this work it was possible to increase the charge carrier transfer ability of titanium dioxide thin films prepared by chemical vapour deposition by forming a new density distribution inside the titanium dioxide crystalline lattice due to a redistribution and new formation of lattice defects.

The arminiase-phase is an auxiliary-construction and needed further investigation. On one hand, it needs to be evaluated how the arminiase-centres cause the electrical and dielectric anomalies observed in each titanium dioxide system. On the other hand, further investigation is needed to understand the exact preparation conditions for the formation of the defective titanium-oxide-polyhedra and their alignment inside an external potential.

Finally, it is necessary to study how the stabilisation of the permanent dipoles and their alignment at room temperature in normal atmosphere can be provided. This might be of an high interest for the development of new quasi-para-electric materials initially based on TiO_6 -octahedral such as photocatalytic active titanium dioxide or pseudo-piezoelectric calcium titanite.

Appendix A

Resistivity

RESISTIVITY MEASUREMENTS DURING IN-SITU XRD EXPERIMENTS

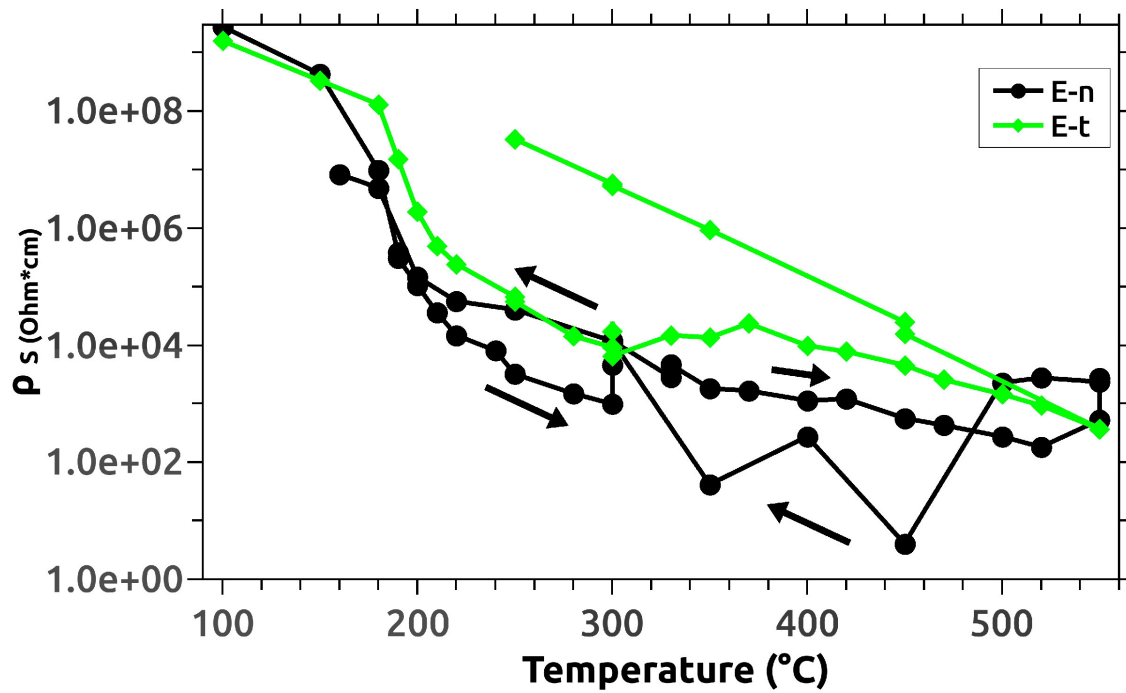


Figure A.1: Resistivity of the measured Degussa P25 pellets during in-situ XRD measurement at the P07 beamline. The reference resistance is $R_R = 1\text{ M}\Omega$ and the applied voltage is $U_{source} \approx 10\text{ V}$.

Appendix B

Structure

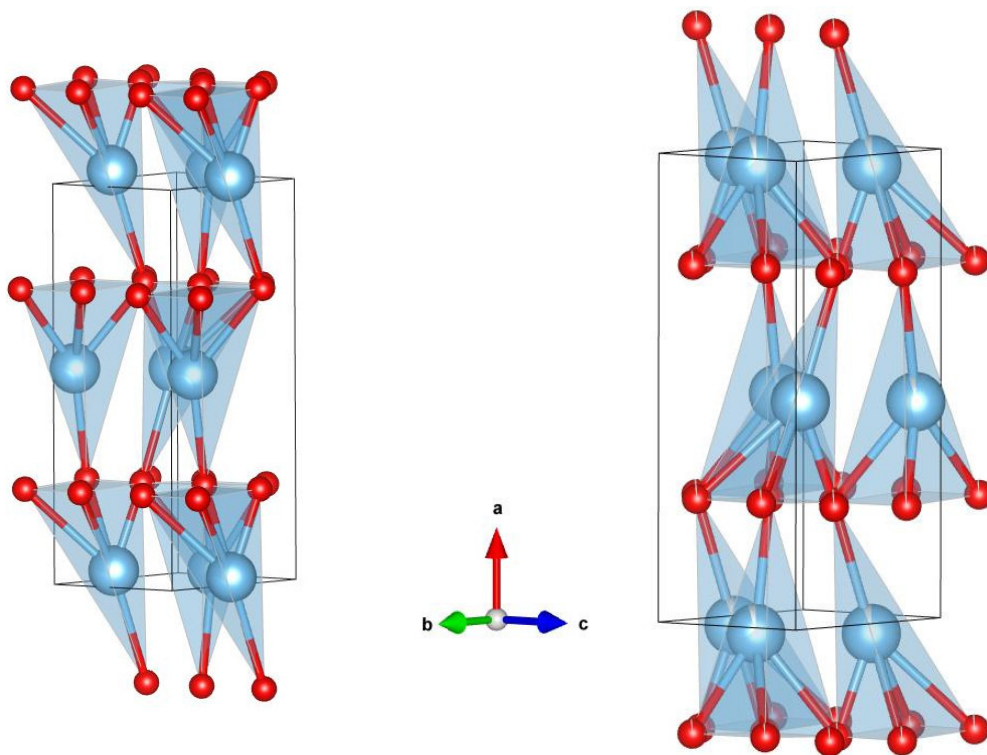


Figure B.1: Arminiasite unit cells with lattice occupancies of the titanium atoms lattice spots of 100%. The occupied lattice spots depend on the orientation of the electrical field. It is assumed, that the electrical field orientation on the left side is in the opposite direction compared to the right side.

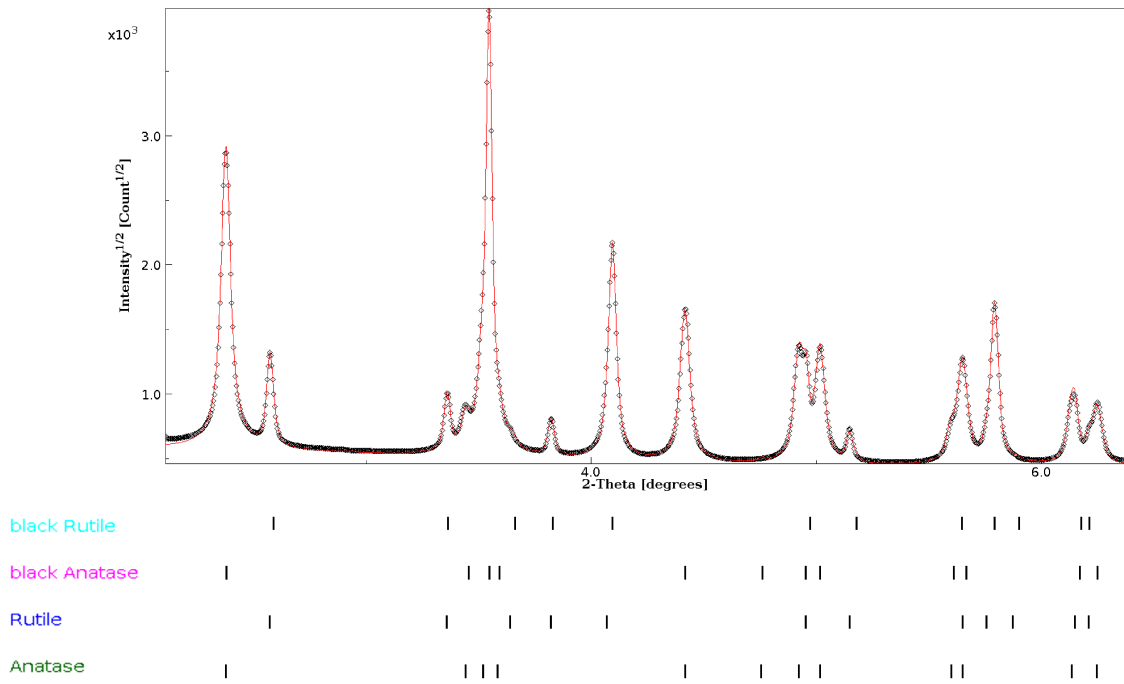


Figure B.2: Rietveld refinement of the black Degussa P25 pellet sample. The experimental data is represented as points and the theoretical calculated curve is represented as red line. It is assumed that defective anatase and defective rutile is included. These two defective phases are representing the density distribution changes inside the original phases and are the basis of the arminiase phase crystallisation.

Appendix C

EPR

COMPLETE EPR-MEASUREMENTS FOR FIELD ASSISTED SAMPLES

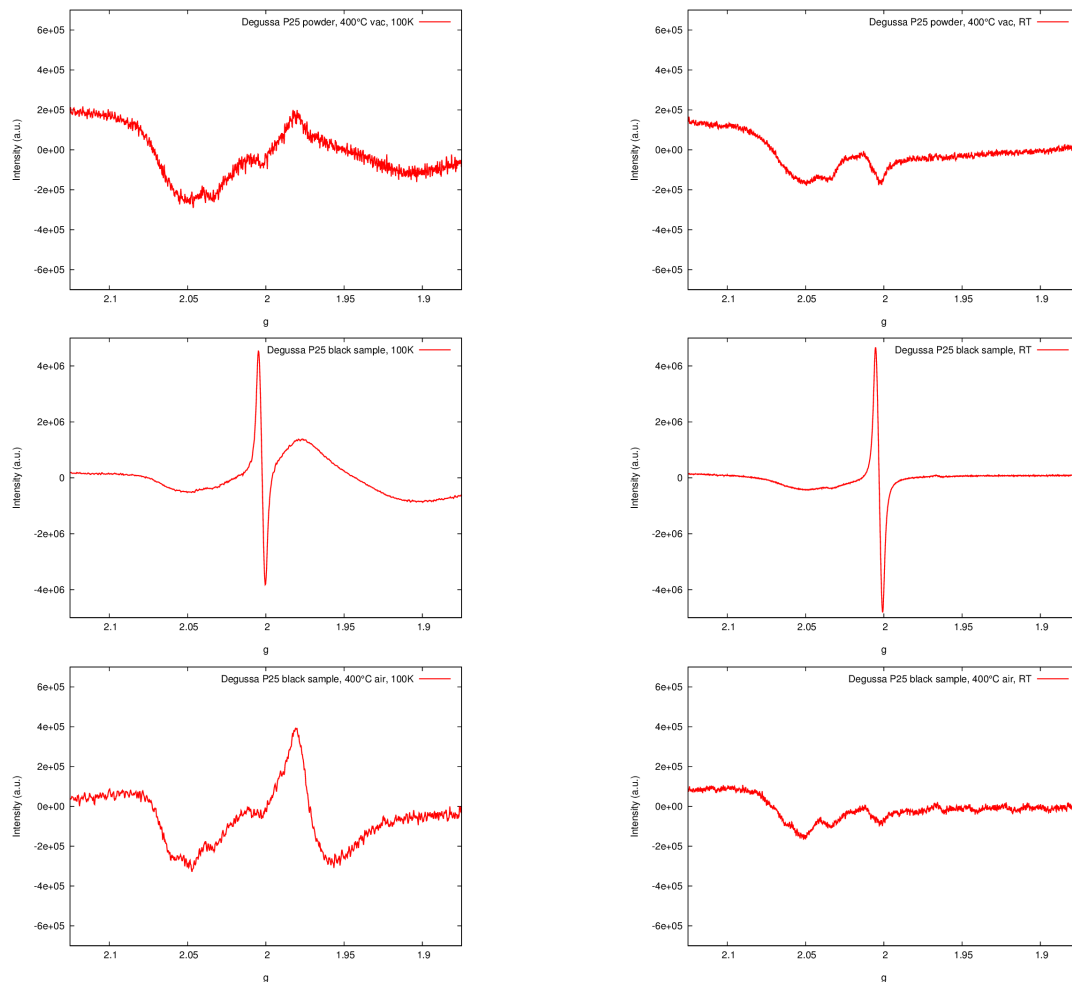


Figure C.1: Complete EPR-measurements of the the field assisted prepared samples and the powder annealed at 400 °C in vacuum. **Left:** Measured at 100 K. **Right:** Measured at room temperature.

Bibliography

- [1] BAILERA, Manuel ; LISBONA, Pilar ; ROMEO, Luis M. ; ESPATOLERO, Sergio: Power to gas projects review: lab, pilot and demo plants for storing renewable energy and CO₂. In: Renewable and Sustainable Energy Reviews 69 (2017), S. 292–312
 - [2] MODI, Anish ; BÜHLER, Fabian ; ANDREASEN, Jesper G. ; HAGLIND, Fredrik: A review of solar energy based heat and power generation systems. In: Renewable and Sustainable Energy Reviews 67 (2017), S. 1047–1064
 - [3] CLACK, Christopher T. ; QVIST, Staffan A. ; APT, Jay ; BAZILIAN, Morgan ; BRANDT, Adam R. ; CALDEIRA, Ken ; DAVIS, Steven J. ; DIAKOV, Victor ; HANDSCHY, Mark A. ; HINES, Paul D. u. a.: Evaluation of a proposal for reliable low-cost grid power with 100% wind, water, and solar. In: Proceedings of the National Academy of Sciences (2017), S. 201610381
 - [4] MOLINARI, Raffaele ; LAVORATO, Cristina ; ARGURIO, Pietro: Recent progress of photocatalytic membrane reactors in water treatment and in synthesis of organic compounds. A review. In: Catalysis Today 281 (2017), S. 144–164
 - [5] GE, Mingzheng ; CAO, Chunyan ; HUANG, Jianying ; LI, Shuhui ; CHEN, Zhong ; ZHANG, Ke-Qin ; AL-DEYAB, SS ; LAI, Yuekun: A review of one-dimensional TiO₂ nanostructured materials for environmental and energy applications. In: Journal of Materials Chemistry A 4 (2016), Nr. 18, S. 6772–6801
 - [6] KANG, Joonhyeon ; KIM, Jinyoung ; LEE, Sangheon ; WI, Sungun ; KIM, Chunjoong ; HYUN, Seungmin ; NAM, Seunghoon ; PARK, Yongjoon ; PARK, Byungwoo: Breathable Carbon-Free Electrode: Black TiO₂ with Hierarchically Ordered Porous Structure for Stable Li–O₂ Battery. In: Advanced Energy Materials (2017)
 - [7] SUNARSO, Jaka ; HASHIM, Siti S. ; ZHU, Na ; ZHOU, Wei: Perovskite oxides applications in high temperature oxygen separation, solid oxide fuel cell and membrane reactor: A review. In: Progress in Energy and Combustion Science 61 (2017), S. 57–77
-

- [8] WANG, Yifei ; LEUNG, Dennis Y. ; XUAN, Jin ; WANG, Huizhi: A review on unitized regenerative fuel cell technologies, part B: Unitized regenerative alkaline fuel cell, solid oxide fuel cell, and microfluidic fuel cell. In: Renewable and Sustainable Energy Reviews 75 (2017), S. 775–795
- [9] BEIRANVAND, A ; TIKKANEN, J ; HUHTINEN, H ; PATURI, P: Electronic and magnetic phase diagram of polycrystalline $Gd_{1-x}Ca_xMnO_3$ manganites. In: Journal of Alloys and Compounds (2017)
- [10] TIKKANEN, J ; HUHTINEN, H ; PATURI, P: Dynamic mesoscale model of the metamagnetic transition in low-bandwidth perovskite manganites. In: Physical Review B 96 (2017), Nr. 1, S. 014405
- [11] YANG, J J. ; PICKETT, Matthew D. ; LI, Xuema ; OHLBERG, Douglas A. ; STEWART, Duncan R. ; WILLIAMS, R S.: Memristive switching mechanism for metal/oxide/metal nanodevices. In: Nature nanotechnology 3 (2008), Nr. 7, S. 429–433
- [12] XU, Qian ; ZHANG, Feihu ; XU, Li ; LEUNG, Puiki ; YANG, Chunzhen ; LI, Huaming: The applications and prospect of fuel cells in medical field: A review. In: Renewable and Sustainable Energy Reviews 67 (2017), S. 574–580
- [13] COLON, Gabriel ; WARD, Brian C. ; WEBSTER, Thomas J.: Increased osteoblast and decreased Staphylococcus epidermidis functions on nanophase ZnO and TiO₂. In: Journal of Biomedical Materials Research Part A 78 (2006), Nr. 3, S. 595–604
- [14] R. SCHNIERER, E. burkel: Formkörper enthaltend piezoelektrisches Calciumtitanoxid, ein Verfahren zu deren Herstellung und Anregung und Verwendung piezoaktiven Calciumtitanoxids als piezoelektrischer Formkörper oder Bestandteil piezoelektrischer Formkörper. 2015
- [15] BINETTI, Enrico ; EL KOURA, Zakaria ; PATEL, Nainesh ; DASHORA, Alpa ; MIOTELLO, Antonio: Rapid hydrogenation of amorphous TiO₂ to produce efficient H-doped anatase for photocatalytic water splitting. In: Applied Catalysis A: General 500 (2015), S. 69–73
- [16] HU, Yun H.: A highly efficient photocatalyst—hydrogenated black TiO₂ for the photocatalytic splitting of water. In: Angewandte Chemie International Edition 51 (2012), Nr. 50, S. 12410–12412
- [17] BESSERGENEV, VG ; MATEUS, MC ; MORGADO, IM ; HANTUSCH, M ; BURKEL, E: Photocatalytic reactor, CVD technology of its preparation and water pu-

- rification from pharmaceutical drugs and agricultural pesticides. In: Chemical Engineering Journal 312 (2017), S. 306–316
- [18] HENDERSON, Michael A.: A surface science perspective on photocatalysis. In: Surface Science Reports 66 (2011), Nr. 6, S. 185–297
- [19] MILLS, Andrew ; LE HUNTE, Stephen: An overview of semiconductor photocatalysis. In: Journal of photochemistry and photobiology A: Chemistry 108 (1997), Nr. 1, S. 1–35
- [20] ZALESKA, Adriana: Doped-TiO₂: a review. In: Recent Patents on Engineering 2 (2008), Nr. 3, S. 157–164
- [21] FINAZZI, Emanuele ; DI VALENTIN, Cristiana ; PACCHIONI, Gianfranco: Nature of Ti interstitials in reduced bulk anatase and rutile TiO₂. In: The Journal of Physical Chemistry C 113 (2009), Nr. 9, S. 3382–3385
- [22] MACDONALD, I R. ; HOWE, Russell F. ; ZHANG, Xinyuan ; ZHOU, Wuzong: In situ EPR studies of electron trapping in a nanocrystalline rutile. In: Journal of Photochemistry and Photobiology A: Chemistry 216 (2010), Nr. 2, S. 238–243
- [23] MACDONALD, I R. ; RHYDDERCH, Shona ; HOLT, Emily ; GRANT, Neil ; STOREY, John M. ; HOWE, Russell F.: EPR studies of electron and hole trapping in titania photocatalysts. In: Catalysis today 182 (2012), Nr. 1, S. 39–45
- [24] PRIEBE, Jacqueline B. ; KARNAHL, Michael ; JUNGE, Henrik ; BELLER, Matthias ; HOLLMANN, Dirk ; BRÜCKNER, Angelika: Water Reduction with Visible Light: Synergy between Optical Transitions and Electron Transfer in Au-TiO₂ Catalysts Visualized by In situ EPR Spectroscopy. In: Angewandte Chemie International Edition 52 (2013), Nr. 43, S. 11420–11424
- [25] PELAEZ, Miguel ; NOLAN, Nicholas T. ; PILLAI, Suresh C. ; SEERY, Michael K. ; FALARAS, Polycarpus ; KONTOS, Athanassios G. ; DUNLOP, Patrick S. ; HAMILTON, Jeremy W. ; BYRNE, J A. ; O'SHEA, Kevin u. a.: A review on the visible light active titanium dioxide photocatalysts for environmental applications. In: Applied Catalysis B: Environmental 125 (2012), S. 331–349
- [26] HANAOR, Dorian A. ; SORRELL, Charles C.: Review of the anatase to rutile phase transformation. In: Journal of Materials science 46 (2011), Nr. 4, S. 855–874
- [27] CHEN, Xiaobo ; SELONI, Annabella: Introduction: titanium dioxide (TiO₂) nanomaterials. 2014

- [28] OLA, Oluwafunmilola ; MAROTO-VALER, M M.: Review of material design and reactor engineering on TiO₂ photocatalysis for CO₂ reduction. In: Journal of Photochemistry and Photobiology C: Photochemistry Reviews 24 (2015), S. 16–42
- [29] HANTUSCH, M ; BESSERGENEV, V ; MATEUS, MC ; KNUPFER, M ; BURKEL, E: Electronic properties of photocatalytic improved Degussa P25 titanium dioxide powder. In: Catalysis Today (2017)
- [30] GUO, Qing ; ZHOU, Chuanyao ; MA, Zhibo ; REN, Zefeng ; FAN, Hongjun ; YANG, Xueming: Elementary photocatalytic chemistry on TiO₂ surfaces. In: Chemical Society Reviews 45 (2016), Nr. 13, S. 3701–3730
- [31] AZNILINDA, Zainuddin ; HERMAN, Sukreen H. ; BAKAR, Raudah A. ; RUSOP, M: Effect of Electrode Types on the Resistive Switching Behavior of Titania Thin Films. In: Applied Mechanics and Materials 393 (2013), S. 74–78
- [32] KASIM, Mohamat ; MARDHIYANA, Shafaq ; SHAARI, Akma ; AZIRA, Nor ; BAKAR, Raudah A. ; HERMAN, Sukreen H.: Switching Behavior of Titania-Zinc Oxide Composites Thin Films. In: Applied Mechanics and Materials 749 (2015), S. 308–312
- [33] NOWOTNY, MK ; SHEPPARD, LR ; BAK, T ; NOWOTNY, J: Defect chemistry of titanium dioxide. Application of defect engineering in processing of TiO₂-based photocatalysts. In: The Journal of Physical Chemistry C 112 (2008), Nr. 14, S. 5275–5300
- [34] NOWOTNY, Janusz ; NORBY, Truls ; BAK, Tadeusz: Reactivity between titanium dioxide and water at elevated temperatures. In: The Journal of Physical Chemistry C 114 (2010), Nr. 42, S. 18215–18221
- [35] BAK, T ; NOWOTNY, J ; REKAS, M ; SORRELL, CC: Defect chemistry and semiconducting properties of titanium dioxide: II. Defect diagrams. In: Journal of Physics and Chemistry of Solids 64 (2003), Nr. 7, S. 1057–1067
- [36] BJØRHEIM, Tor S. ; KUWABARA, Akihide ; NORBY, Truls: Defect Chemistry of Rutile TiO₂ from First Principles Calculations. In: The Journal of Physical Chemistry C 117 (2013), Nr. 11, S. 5919–5930
- [37] CHENG, Zhijun ; LIU, Tingyu ; YANG, Chenxing ; GAN, Haixiu ; CHEN, Jianyu ; ZHANG, Feiwu: Ab initio atomic thermodynamics investigation on oxygen defects in the anatase TiO₂. In: Journal of Alloys and Compounds 546 (2013), S. 246–252

- [38] DI VALENTIN, Cristiana ; PACCHIONI, Gianfranco ; SELLONI, Annabella: Reduced and n-type doped TiO₂: nature of Ti³⁺ species. In: The Journal of Physical Chemistry C 113 (2009), Nr. 48, S. 20543–20552
- [39] ERDAL, Skjalg ; KONGSHAUG, Camilla ; BJØRHEIM, Tor S. ; JALARVO, Niina ; HAUGSRUD, Reidar ; NORBY, Truls: Hydration of rutile TiO₂: thermodynamics and effects on n-and p-Type electronic conduction. In: The Journal of Physical Chemistry C 114 (2010), Nr. 19, S. 9139–9145
- [40] PAN, Xiaoyang ; YANG, Min-Quan ; FU, Xianzhi ; ZHANG, Nan ; XU, Yi-Jun: Defective TiO₂ with oxygen vacancies: synthesis, properties and photocatalytic applications. In: Nanoscale 5 (2013), Nr. 9, S. 3601–3614
- [41] MOMMA, Koichi ; IZUMI, Fujio: VESTA 3 for three-dimensional visualization of crystal, volumetric and morphology data. In: Journal of Applied Crystallography 44 (2011), Nr. 6, S. 1272–1276
- [42] HANTUSCH, M ; BESSERGENEV, V ; SCHELL, N ; KNUPFER, M ; BURKEL, E: Resistive switching and electrical field induced crystal structure changes in titanium dioxides observed in-situ by synchrotron radiation. In: in preparation (2018)
- [43] KRÖGER, FA ; VINK, HJ: Relations between the concentrations of imperfections in crystalline solids. In: Solid state physics 3 (1956), S. 307–435
- [44] CHENG, Hongzhi ; SELLONI, Annabella: Surface and subsurface oxygen vacancies in anatase TiO₂ and differences with rutile. In: Physical Review B 79 (2009), Nr. 9, S. 092101
- [45] SETO, John Y.: The electrical properties of polycrystalline silicon films. In: Journal of Applied Physics 46 (1975), Nr. 12, S. 5247–5254
- [46] LIU, Hong ; MA, HT ; LI, XZ ; LI, WZ ; WU, M ; BAO, XH: The enhancement of TiO₂ photocatalytic activity by hydrogen thermal treatment. In: Chemosphere 50 (2003), Nr. 1, S. 39–46
- [47] C, Liu ; L, Miao ; D, Hu ; R, Huang ; CAJ, Fisher ; S, Tanemura ; H, Gu: Enhanced asymmetrical transport of carriers induced by local structural distortion in chemically tuned titania: A possible mechanism for enhancing thermoelectric properties. In: Physical Review B 88 (2013), Nr. 20, S. 205201
- [48] AGARWALA, S ; HO, GW: Synthesis and tuning of ordering and crystallinity of mesoporous titanium dioxide film. In: Materials Letters 63 (2009), Nr. 18, S. 1624–1627

- [49] YONG, MJQ ; WONG, ASW ; HO, GW: Mesophase ordering and macroscopic morphology structuring of mesoporous TiO₂ film. In: Materials Chemistry and Physics 116 (2009), Nr. 2, S. 563–568
- [50] ROUQUEROL, J ; AVNIR, D ; FAIRBRIDGE, CW ; EVERETT, DH ; HAYNES, JM ; PERNICONE, N ; RAMSAY, JDF ; SING, KSW ; UNGER, KK: Recommendations for the characterization of porous solids (Technical Report). In: Pure and Applied Chemistry 66 (1994), Nr. 8, S. 1739–1758
- [51] BESSERGENEV, VG ; MATEUS, MC ; REGO, AM B. ; HANTUSCH, M ; BURKEL, E: An improvement of photocatalytic activity of TiO₂ Degussa P25 powder. In: Applied Catalysis A: General 500 (2015), S. 40–50
- [52] ROUQUEROL, Jean ; ROUQUEROL, Françoise ; LLEWELLYN, Philip ; MAURIN, Guillaume ; SING, Kenneth S.: Adsorption by powders and porous solids: principles, methodology and applications. (2013)
- [53] BURKE, JE ; TURNBULL, D: Recrystallization and grain growth. In: Progress in metal physics 3 (1952), S. 220IN11245IN13267IN15275–244IN12266IN14274292
- [54] HILLERT, M: On the theory of normal and abnormal grain growth. In: Acta metallurgica 13 (1965), Nr. 3, S. 227–238
- [55] STIR, Manuela E.: Structure and Dynamics of Amorphous and Nanostructured Materials, Universität Rostock, Diss., 2004
- [56] ESTRIN, Y ; GOTTSTEIN, G ; RABKIN, E ; SHVINDLERMAN, LS: On the kinetics of grain growth inhibited by vacancy generation. In: Scripta materialia 43 (2000), Nr. 2, S. 141–147
- [57] WATANABE, D ; CASTLES, J R. ; JOSTSONS, A ; MALIN, A S.: The ordered structure of Ti O. In: Acta Crystallographica (1,1948-23,1967) 23 (1967), S. 307–313
- [58] 'NEWNHAM, R. E. ; HAAN, Y. M.: Refinement of the alpha Al₂O₃, Ti₂O₃, V₂O₃ and Cr₂O₃ structures. In: Zeitschrift für Kristallographie 117 (1962), S. 235–237
- [59] HANTUSCH, Martin: Strukturdynamische Untersuchungen an Titandioxid, Universität Rostock, Diplomarbeit, 2013
- [60] DAOUD, Walid A. ; XIN, John H.: Low temperature sol-gel processed photocatalytic titania coating. In: Journal of Sol-Gel Science and Technology 29 (2004), Nr. 1, S. 25–29

- [61] KLUSON, P ; KACER, P ; CAJTHAML, T ; KALAJI, M: Preparation of titania mesoporous materials using a surfactant-mediated sol-gel method. In: J. Mater. Chem. 11 (2001), Nr. 2, S. 644–651
- [62] KHATIM, O. ; AMAMRA, M. ; CHHOR, K. ; BELL, A.M.T. ; NOVIKOV, D. ; VREL, D. ; KANAIEV, A.: Amorphous anatase phase transition in single immobilized TiO₂ nanoparticles. In: Chemical Physics Letters 558 (2013), Februar, Nr. 0, 53–56. <http://www.sciencedirect.com/science/article/pii/S0009261412014388>. – ISSN 0009–2614
- [63] OHTANI, B ; PRIETO-MAHANEY, OO ; LI, D ; ABE, R: What is Degussa (Evonik) P25? Crystalline composition analysis, reconstruction from isolated pure particles and photocatalytic activity test. In: Journal of Photochemistry and Photobiology A: Chemistry 216 (2010), Nr. 2, S. 179–182
- [64] TILOCCA, Antonio ; SELONI, Annabella: Reaction pathway and free energy barrier for defect-induced water dissociation on the (101) surface of TiO₂-anatase. In: The Journal of chemical physics 119 (2003), Nr. 14, S. 7445–7450
- [65] ZHOU, Chuanyao ; REN, Zefeng ; TAN, Shijing ; MA, Zhibo ; MAO, Xinchun ; DAI, Dongxu ; FAN, Hongjun ; YANG, Xueming ; LARUE, Jerry ; COOPER, Russell u. a.: Site-specific photocatalytic splitting of methanol on TiO₂ (110). In: Chemical Science 1 (2010), Nr. 5, S. 575–580
- [66] SOOD, Gouma: Polymorphic phase transitions in nacrystalline binary metal oxides. In: J. Am. Ceram. Soc. (2012), S. 1–4
- [67] SABYROV, Kairat ; BURROWS, Nathan D. ; PENN, R. L.: Size-Dependent Anatase to Rutile Phase Transformation and Particle Growth. In: Chemistry of Materials 25 (2013), Nr. 8, 1408-1415. <http://dx.doi.org/10.1021/cm302129a>. – DOI 10.1021/cm302129a
- [68] BUHR, Dipl.-Chem. S.: Untersuchung zur Eignung von TiO₂ zur photokatalytischen Reinigung von Kraftfahrzeugabgasen, Universität Hannover, Diss., 2005
- [69] GAYA, Umar I. ; ABDULLAH, Abdul H.: Heterogeneous photocatalytic degradation of organic contaminants over titanium dioxide: a review of fundamentals, progress and problems. In: Journal of Photochemistry and Photobiology C: Photochemistry Reviews 9 (2008), Nr. 1, S. 1–12
- [70] BOWKER, Michael ; SHARPE, Ryan: Pd deposition on TiO₂ (110) and nanoparticle encapsulation. In: Catalysis, Structure & Reactivity 1 (2015), Nr. 3, S. 140–145

- [71] CHEN, Juanrong ; QIU, Fengxian ; XU, Wanzhen ; CAO, Shunsheng ; ZHU, Huijun: Recent progress in enhancing photocatalytic efficiency of TiO₂-based materials. In: Applied Catalysis A: General 495 (2015), S. 131–140
- [72] CHAO, H.E. ; YUN, Y.U. ; XINGFANG, H.U. ; LARBOT, A.: Effect of silver doping on the phase transformation and grain growth of sol-gel titania powder. In: Journal of the European Ceramic Society 23 (2003), Nr. 9, 1457 - 1464. [http://dx.doi.org/http://dx.doi.org/10.1016/S0955-2219\(02\)00356-4](http://dx.doi.org/http://dx.doi.org/10.1016/S0955-2219(02)00356-4). – DOI [http://dx.doi.org/10.1016/S0955-2219\(02\)00356-4](http://dx.doi.org/10.1016/S0955-2219(02)00356-4). – ISSN 0955–2219
- [73] ASAHI, RYOJI ; MORIKAWA, TAKESHI ; OHWAKI, T ; AOKI, K ; TAGA, Y: Visible-light photocatalysis in nitrogen-doped titanium oxides. In: science 293 (2001), Nr. 5528, S. 269–271
- [74] DONG, Junye ; HAN, Jie ; LIU, Yangsi ; NAKAJIMA, Akira ; MATSUSHITA, Sachiko ; WEI, Shanghai ; GAO, Wei: Defective black TiO₂ synthesized via anodization for visible-light photocatalysis. In: ACS applied materials & interfaces 6 (2014), Nr. 3, S. 1385–1388
- [75] DIEBOLD, Ulrike: The surface science of titanium dioxide. In: Surface science reports 48 (2003), Nr. 5, S. 53–229
- [76] DESKINS, N A. ; ROUSSEAU, Roger ; DUPUIS, Michel: Defining the role of excess electrons in the surface chemistry of TiO₂. In: The Journal of Physical Chemistry C 114 (2010), Nr. 13, S. 5891–5897
- [77] NORBY, Truls: Proton conduction in solids: Bulk and interfaces. In: MRS bulletin 34 (2009), Nr. 12, S. 923–928
- [78] DESKINS, N A. ; DUPUIS, Michel: Intrinsic hole migration rates in TiO₂ from density functional theory. In: The Journal of Physical Chemistry C 113 (2008), Nr. 1, S. 346–358
- [79] OHNO, Teruhisa ; TOKIEDA, Kojiro ; HIGASHIDA, Suguru ; MATSUMURA, Michio: Synergism between rutile and anatase TiO₂ particles in photocatalytic oxidation of naphthalene. In: Applied Catalysis A: General 244 (2003), Nr. 2, S. 383–391
- [80] LUTTEROTTI, Luca ; CECCATO, Riccardo ; DAL MASCHIO, Roberto ; PAGANI, Eva: Quantitative analysis of silicate glass in ceramic materials by the Rietveld method. In: Materials Science Forum Bd. 278 Aedermannsdorf, Switzerland: Trans Tech Publications, 1984-, 1998, S. 87–92

- [81] CARVAJAL, JR: An introduction to the program FullProf. In: Laboratoire Leon Brillouin (CEA-CRNS), France Search PubMed (2000)
- [82] LUTTEROTTI, L ; BORTOLOTTI, M ; ISCHIA, G ; LONARDELLI, I ; WENK, HR: Rietveld texture analysis from diffraction images. In: Z. Kristallogr. Suppl 26 (2007), S. 125–130
- [83] DENG, Fei ; LIN, Xiaodong ; HE, Yonghong ; LI, Shu ; ZI, Run ; LAI, Shijun: Quantitative Phase Analysis by the Rietveld Method for Forensic Science. In: Journal of forensic sciences 60 (2015), Nr. 4, S. 1040–1045
- [84] CHAUDHRY, M A. ; JONSCHER, Andrew K.: The dielectric properties of mica paper in variable temperature and humidity. In: Journal of materials science 20 (1985), Nr. 10, S. 3581–3589
- [85] BARRETT, Elliott P. ; JOYNER, Leslie G. ; HALENDA, Paul P.: The determination of pore volume and area distributions in porous substances. I. Computations from nitrogen isotherms. In: Journal of the American Chemical society 73 (1951), Nr. 1, S. 373–380
- [86] SING, Kenneth: The use of nitrogen adsorption for the characterisation of porous materials. In: Colloids and Surfaces A: Physicochemical and Engineering Aspects 187 (2001), S. 3–9
- [87] SING, Kenneth S.: Reporting physisorption data for gas/solid systems with special reference to the determination of surface area and porosity (Recommendations 1984). In: Pure and applied chemistry 57 (1985), Nr. 4, S. 603–619
- [88] BRUNAUER, Stephen ; EMMETT, Paul H. ; TELLER, Edward: Adsorption of gases in multimolecular layers. In: Journal of the American chemical society 60 (1938), Nr. 2, S. 309–319
- [89] LEOFANTI, G ; PADOVAN, M ; TOZZOLA, G ; VENTURELLI, B: Surface area and pore texture of catalysts. In: Catalysis Today 41 (1998), Nr. 1, S. 207–219
- [90] MILLER, Kyle ; NALWA, Kanwar S. ; BERGERUD, Amy ; NEIHART, Nathan M. ; CHAUDHARY, Sumit: Memristive behavior in thin anodic titania. In: Electron Device Letters, IEEE 31 (2010), Nr. 7, S. 737–739
- [91] MOULDER, John F. ; CHASTAIN, Jill ; KING, Roger C.: Handbook of X-ray photoelectron spectroscopy: a reference book of standard spectra for identification and interpretation of XPS data. Physical Electronics Eden Prairie, MN, 1995

- [92] HOFMANN, Siegfried: Practical surface analysis: state of the art and recent developments in AES, XPS, ISS and SIMS. In: Surface and Interface Analysis 9 (1986), Nr. 1, S. 3–20
- [93] RUSS, John C.: Fundamentals of Energy Dispersive X-Ray Analysis: Butterworths Monographs in Materials. Butterworth-Heinemann, 2013
- [94] BESSERGENEV, VG ; MATEUS, MC ; VASCONCELOS, DA ; MARIANO, JFML ; REGO, AM Botelho d. ; LANGE, R ; BURKEL, E: TiO₂:(Fe, S) thin films prepared from complex precursors by CVD, physical chemical properties, and photocatalysis. In: International Journal of Photoenergy DOI: 10.1155/2012/767054 (2012). <http://dx.doi.org/10.1155/2012/767054>. – DOI 10.1155/2012/767054
- [95] LIVRAGHI, Stefano ; CHIESA, Mario ; PAGANINI, Maria C. ; GIAMELLO, Elio: On the nature of reduced states in titanium dioxide as monitored by electron paramagnetic resonance. I: the anatase case. In: The Journal of Physical Chemistry C 115 (2011), Nr. 51, S. 25413–25421
- [96] LIVRAGHI, Stefano ; ROLANDO, Manuela ; MAURELLI, Sara ; CHIESA, Mario ; PAGANINI, Maria C. ; GIAMELLO, Elio: Nature of reduced states in titanium dioxide as monitored by electron paramagnetic resonance. II: Rutile and brookite cases. In: The Journal of Physical Chemistry C 118 (2014), Nr. 38, S. 22141–22148
- [97] BESSERGUENEV, VG ; PEREIRA, RJF ; MATEUS, MC ; KHMELINSKII, IV ; NICULA, RC ; BURKEL, E: TiO₂ thin film synthesis from complex precursors by CVD, its physical and photocatalytic properties. In: International Journal of Photoenergy 5 (2003), Nr. 2, S. 99–105
- [98] MATEUS, M Conceição DA ; SILVA, Abilio M. ; BURROWS, Hugh D.: Fenarimol solar degradation pathways and photoproducts in aqueous solution. In: Chemosphere 48 (2002), Nr. 3, S. 363–373
- [99] SNYDER, Lloyd R. ; KIRKLAND, Joseph J. ; GLAJCH, Joseph L.: Practical HPLC method development. John Wiley & Sons, 2012
- [100] ODRIOZOLA-SERRANO, Isabel ; HERNÁNDEZ-JOVER, Teresa ; MARTÍN-BELLOSO, Olga: Comparative evaluation of UV-HPLC methods and reducing agents to determine vitamin C in fruits. In: Food Chemistry 105 (2007), Nr. 3, S. 1151–1158
- [101] BESSERGENEV, V ; GOMES, Henrique L.: Electrical properties of thin-films wide-band gap semiconductor TiO₂ prepared by CVD. In: physica status solidi (c) 7 (2010), Nr. 3-4, S. 949–952

- [102] BRINKER, CJ ; FRYE, GC ; HURD, AJ ; ASHLEY, CS: Fundamentals of sol-gel dip coating. In: Thin Solid Films 201 (1991), Nr. 1, S. 97–108
- [103] WANG, Zhuyi ; SHI, Liyi ; WU, Fengqing ; YUAN, Shuai ; ZHAO, Yin ; ZHANG, Meihong: The sol-gel template synthesis of porous TiO₂ for a high performance humidity sensor. In: Nanotechnology 22 (2011), S. 1–9. <http://dx.doi.org/10.1088/0957-4484/22/27/275502>. – DOI 10.1088/0957-4484/22/27/275502
- [104] LU, Yunfeng ; GANGULI, Rahul ; DREWIEN, Celeste A. ; ANDERSON, Mark T. ; BRINKER, C J. ; GONG, Weilang ; GUO, Yongxing ; SOYEZ, Hermes ; DUNN, Bruce ; HUANG, Michael H. u. a.: Continuous formation of supported cubic and hexagonal mesoporous films by sol-gel dip-coating. In: Nature 389 (1997), Nr. 6649, S. 364–368
- [105] SCHMIDT, Helmut K.: Das Sol-Gel-Verfahren: Anorganische Synthesemethoden. In: Chemie in unserer Zeit (2001)
- [106] LIU, Xiaoheng ; YANG, Juan ; WANG, Ling ; YANG, Xujie ; LU, Lude ; WANG, Xin: An improvement on sol-gel method for preparing ultrafine and crystallized titania powder. In: Materials Science and Engineering A289 (2000), S. 241–245
- [107] BESSERGENEV, VG ; KHMELINSKII, IV ; PEREIRA, RJF ; KRISUK, VV ; TURGAMBAEVA, AE ; IGUMENOV, IK: Preparation of TiO₂ films by CVD method and its electrical, structural and optical properties. In: Vacuum 64 (2002), Nr. 3, S. 275–279
- [108] BESSERGENEV, Valentin: The use of complex compounds in chemical vapour deposition. In: Journal of Physics: Condensed Matter 16 (2004), Nr. 5, S. S531
- [109] LI, Guangshe ; LI, Liping ; BOERIO-GOATES, Juliana ; WOODFIELD, Brian F.: High purity anatase TiO₂ nanocrystals: near room-temperature synthesis, grain growth kinetics, and surface hydration chemistry. In: Journal of the American Chemical Society 127 (2005), Nr. 24, S. 8659–8666
- [110] TIAN, Jian ; HU, Xiaolin ; YANG, Hongru ; ZHOU, Yanli ; CUI, Hongzhi ; LIU, Hong: High yield production of reduced TiO₂ with enhanced photocatalytic activity. In: Applied Surface Science 360 (2016), S. 738–743
- [111] CASA, XPS: version 2.3. 16. In: Casa Software Ltd.: Teignmouth, UK (2010)
- [112] WOJDYR, Marcin: Fityk: a general-purpose peak fitting program. In: Journal of Applied Crystallography 43 (2010), Nr. 5, S. 1126–1128

- [113] KNOEFEL, Christina ; HORNEBECQ, Virginie ; LLEWELLYN, Philip L.: Microcalorimetric investigation of high-surface-area mesoporous titania samples for CO₂ adsorption. In: Langmuir 24 (2008), Nr. 15, S. 7963–7969
- [114] RAUPP, Gregory B. ; DUMESIC, JA: Adsorption of carbon monoxide, carbon dioxide, hydrogen, and water on titania surfaces with different oxidation states. In: The Journal of Physical Chemistry 89 (1985), Nr. 24, S. 5240–5246
- [115] BAK, Tadeusz ; NOWOTNY, Janusz ; SUCHER, Nikolaus J. ; WACHSMAN, Eric: Effect of crystal imperfections on reactivity and photoreactivity of TiO₂ (rutile) with oxygen, water, and bacteria. In: The Journal of Physical Chemistry C 115 (2011), Nr. 32, S. 15711–15738
- [116] NOWOTNY, MK ; BAK, T ; NOWOTNY, J: Electrical properties and defect chemistry of TiO₂ single crystal. I. Electrical conductivity. In: The Journal of Physical Chemistry B 110 (2006), Nr. 33, S. 16270–16282
- [117] MARIN, Raimon P. ; ISHIKAWA, Satoshi ; BAHRUJI, Hasliza ; SHAW, Greg ; KONDRAT, Simon A. ; MIEDZIAK, Peter J. ; MORGAN, David J. ; TAYLOR, Stuart H. ; BARTLEY, Jonathan K. ; EDWARDS, Jennifer K. u. a.: Supercritical antisolvent precipitation of TiO₂ with tailored anatase/rutile composition for applications in redox catalysis and photocatalysis. In: Applied Catalysis A: General 504 (2015), S. 62–73
- [118] LIU, HaiBei ; SHEN, Fan ; XING, Mingyang ; ZHANG, Jinlong ; ANPO, Masakazu: Synthesis, characterization and photo-activity of vacuum activated V⁴⁺ and Ti³⁺ doped TiO₂. In: Catalysis letters 144 (2014), Nr. 9, S. 1494–1498
- [119] OKU, Masaoki ; WAGATSUMA, Kazuaki ; KOHIKI, Shigemi: Ti 2p and Ti 3p X-ray photoelectron spectra for TiO₂, SrTiO₃ and BaTiO₃. In: Physical Chemistry Chemical Physics 1 (1999), Nr. 23, S. 5327–5331
- [120] LEICHTWEISS, Thomas ; HENNING, Ralph A. ; KOETTGEN, Julius ; SCHMIDT, Rüdiger M ; HOLLÄNDER, Bernd ; MARTIN, Manfred ; WUTTIG, Matthias ; JANEK, Jürgen: Amorphous and highly nonstoichiometric titania (TiO_x) thin films close to metal-like conductivity. In: Journal of Materials Chemistry A 2 (2014), Nr. 18, S. 6631–6640
- [121] SHIBUYA, Keisuke ; DITTMANN, Regina ; MI, Shaobo ; WASER, Rainer: Impact of defect distribution on resistive switching characteristics of Sr₂TiO₄ thin films. In: Advanced materials 22 (2010), Nr. 3, S. 411–414

- [122] SCHWARZBURG, K ; WILLIG, F: Influence of trap filling on photocurrent transients in polycrystalline TiO₂. In: Applied physics letters 58 (1991), Nr. 22, S. 2520–2522
- [123] HENCH, Larry L. ; WEST, Jon K.: The sol-gel process. In: Chemical reviews 90 (1990), Nr. 1, S. 33–72
- [124] BESSERGENEV, Valentin: High-temperature anomalies of dielectric constant in TiO₂ thin films. In: Materials Research Bulletin 44 (2009), Nr. 8, S. 1722–1728
- [125] CHEN, Xiaobo ; LIU, Lei ; HUANG, Fuqiang: Black titanium dioxide (TiO₂) nanomaterials. In: Chemical Society Reviews 44 (2015), Nr. 7, S. 1861–1885
- [126] WANG, Zhou ; YANG, Chongyin ; LIN, Tianquan ; YIN, Hao ; CHEN, Ping ; WAN, Dongyun ; XU, Fangfang ; HUANG, Fuqiang ; LIN, Jianhua ; XIE, Xiaoming u. a.: H-Doped Black Titania with Very High Solar Absorption and Excellent Photocatalysis Enhanced by Localized Surface Plasmon Resonance. In: Advanced Functional Materials 23 (2013), Nr. 43, S. 5444–5450
- [127] HURUM, DC ; AGRIOS, AG ; CRIST, SE ; GRAY, KA ; RAJH, T ; THURNAUER, MC: Probing reaction mechanisms in mixed phase TiO₂ by EPR. In: Journal of Electron Spectroscopy and Related Phenomena 150 (2006), Nr. 2, S. 155–163
- [128] WANG, Zhaohui ; MA, Wanhong ; CHEN, Chuncheng ; JI, Hongwei ; ZHAO, Jincai: Probing paramagnetic species in titania-based heterogeneous photocatalysis by electron spin resonance (ESR) spectroscopy—a mini review. In: Chemical engineering journal 170 (2011), Nr. 2, S. 353–362
- [129] HURUM, Deanna C. ; GRAY, Kimberly A. ; RAJH, Tijana ; THURNAUER, Marion C.: Recombination pathways in the Degussa P25 formulation of TiO₂: surface versus lattice mechanisms. In: The Journal of Physical Chemistry B 109 (2005), Nr. 2, S. 977–980
- [130] HORN, M ; SCHWERDTFEGER, C F. ; MEAGHER, E P.: In: Zeitschrift fuer Kristallographie, Kristallgeometrie, Kristallphysik, Kristallchemie 136 (1972), 273–281 S.
- [131] SEKI, H. ; ISHIZAWA, N. ; MIZUTANI, N. ; KATO, M.: High Temperature Structures of the Rutile-Type Oxides, TiO₂ and SnO₂. In: Journal of the Ceramic Association, Japan 92 (1984), S. 219–223
- [132] WYCKOFF, R. W. G.: Cubic closest packed, ccp, structure. In: Crystal Structures, Second edition. Interscience Publishers, New York, New York 1 (1963), S. 7–83

- [133] NIGGLI, P: Die Kristallstruktur einiger Oxyde I. In: Zeitschrift fuer Kristallographie, Kristallgeometrie, Kristallphysik, Kristallchemie 57 (1922), S. 253–299
- [134] PAULING, J.H. L.; S. L.; Sturdivant: The crystal structure of brookite. In: Zeitschrift fuer Kristallographie, Kristallgeometrie, Kristallphysik, Kristallchemie 68 (1928), S. 239–256
- [135] MO, Shang-Di ; CHING, WY: Electronic and optical properties of three phases of titanium dioxide: Rutile, anatase, and brookite. In: Physical Review B 51 (1995), Nr. 19, S. 13023
- [136] VEQUIZO, Junie Jhon M. ; MATSUNAGA, Hironori ; ISHIKU, Tatsuya ; KAMIMURA, Sunao ; OHNO, Teruhisa ; YAMAKATA, Akira: Trapping-Induced Enhancement of Photocatalytic Activity on Brookite TiO₂ Powders: Comparison with Anatase and Rutile TiO₂ Powders. In: ACS Catalysis 7 (2017), Nr. 4, S. 2644–2651
- [137] SOUSA, Carmen ; ILLAS, Francesc: Ionic-covalent transition in titanium oxides. In: Physical Review B 50 (1994), Nr. 19, S. 13974
- [138] SAHA, Sonali ; SINHA, TP ; MOOKERJEE, Abhijit: Structural and optical properties of paraelectric SrTiO₃. In: Journal of Physics: Condensed Matter 12 (2000), Nr. 14, S. 3325
- [139] HACHEMI, A ; HACHEMI, H ; FERHAT-HAMIDA, A ; LOUAIL, L: Elasticity of SrTiO₃ perovskite under high pressure in cubic, tetragonal and orthorhombic phases. In: Physica Scripta 82 (2010), Nr. 2, S. 025602
- [140] MAHMOOD, Natheer B. ; AL-SHAKARCHI, Emad K. ; ELOUADI, Brahim: Three Techniques Used to Produce BaTiO₃ Fine Powder. In: Journal of Modern Physics 2 (2011), S. 1420–1428
- [141] WANG, Yan ; HE, Yiming ; LAI, Qinghua ; FAN, Maohong: Review of the progress in preparing nano TiO₂: An important environmental engineering material. In: Journal of Environmental Sciences 26 (2014), Nr. 11, S. 2139–2177
- [142] LIAO, Yichuan ; LI, Huayao ; LIU, Yuan ; ZOU, Zhijun ; ZENG, Dawen ; XIE, Changsheng: Characterization of photoelectric properties and composition effect of TiO₂/ZnO/Fe₂O₃ composite by combinatorial methodology. In: Journal of combinatorial chemistry 12 (2010), Nr. 6, S. 883–889

- [143] LI, Zhensheng ; QU, Yang ; ZHANG, Xingdong ; YANG, Bangcheng: Bioactive nano-titania ceramics with biomechanical compatibility prepared by doping with piezoelectric BaTiO₃. In: Acta biomaterialia 5 (2009), Nr. 6, S. 2189–2195
- [144] YILDIZ, K ; KARAKU, N ; TOPLAN, N ; TOPLAN, HÖ: Densification and grain growth of TiO₂-doped ZnO. In: Materials Science-Poland 25 (2007), Nr. 4
- [145] JANISCH, Rebecca ; GOPAL, Priya ; SPALDIN, Nicola A.: Transition metal-doped TiO₂ and ZnO—present status of the field. In: Journal of Physics: Condensed Matter 17 (2005), Nr. 27, S. R657
- [146] BLOM, PWM ; WOLF, RM ; CILLESSEN, JFM ; KRIJN, MPCM: Ferroelectric schottky diode. In: Physical review letters 73 (1994), Nr. 15, S. 2107
- [147] KAMARUZAMAN, NS ; HERMAN, SH ; MAHMUDIN, MA: Memristive behaviour of spin coated titania thin film. In: IOP Conference Series: Materials Science and Engineering Bd. 64 IOP Publishing, 2014, S. 012054
- [148] SUO, Z: Models for breakdown-resistant dielectric and ferroelectric ceramics. In: Journal of the Mechanics and Physics of Solids 41 (1993), Nr. 7, S. 1155–1176
- [149] LOMBARDO, Salvatore ; STATHIS, James H. ; LINDER, Barry P. ; PEY, Kin L. ; PALUMBO, Felix ; TUNG, Chih H.: Dielectric breakdown mechanisms in gate oxides. In: Journal of Applied Physics 98 (2005), Nr. 12, S. 12
- [150] FUKADA, Eiichi: Piezoelectric properties of organic polymers. In: Annals of the New York Academy of Sciences 238 (1974), Nr. 1, S. 7–25
- [151] MAEDA, Hideatsu ; FUKADA, Eiich: Effect of water on piezoelectric, dielectric, and elastic properties of bone. In: Biopolymers 21 (1982), Nr. 10, S. 2055–2068
- [152] CHEN, Sa ; SHANG, Ran ; HU, Ke-Li ; WANG, Zhe-Ming ; GAO, Song: [NH₂NH₃][M(HCOO)₃](M= Mn²⁺, Zn²⁺, Co²⁺ and Mg²⁺): structural phase transitions, prominent dielectric anomalies and negative thermal expansion, and magnetic ordering. In: Inorganic Chemistry Frontiers 1 (2014), Nr. 1, S. 83–98
- [153] MORGAN, Benjamin J. ; WATSON, Graeme W.: A DFT+U description of oxygen vacancies at the TiO₂ rutile (110) surface. In: Surface Science 601 (2007), Nr. 21, S. 5034–5041
- [154] TARAZONA, P: A density functional theory of melting. In: Molecular physics 52 (1984), Nr. 1, S. 81–96
- [155] TARAZONA, Pedro: Free-energy density functional for hard spheres. In: Physical Review A 31 (1985), Nr. 4, S. 2672

- [156] COX, GA ; TREGOLD, RH: On the electrical conductivity of calcium titanate crystals. In: British Journal of Applied Physics 18 (1967), Nr. 1, S. 37
- [157] MANIK, SK ; PRADHAN, SK ; PAL, M: Nanocrystalline CaTiO₃ prepared by soft-chemical route. In: Physica E: Low-dimensional Systems and Nanostructures 25 (2005), Nr. 4, S. 421–424
- [158] GUO, L ; YANG, Z ; MARCUS, K ; LI, Z ; LUO, B ; ZHOU, L ; WANG, X ; DU, Y ; YANG, Y: MoS₂/TiO₂ heterostructures as nonmetal plasmonic photocatalysts for highly efficient hydrogen evolution. In: Energy & Environmental Science (2017)

List of Figures

1.1	Schematic draw (left) and photography(right) of the photocatalytic reactor for water purification [17].	2
2.1.1	Schematic draw of a titanium dioxide 2D-lattice with the different types of defects [29, 33].	6
2.1.2	Perfect titania octahedron(a), octahedron with a top defect(b), octahedron with a plane defect(c), plotted by [41], modified from [42].	7
2.1.3	Schematic representation of the band structure of a semiconductor with lattice defects resulting in a conduction band with charge carrier traps, from [29]. It shows the difference between a low defective n-type semiconductor(left) and a high defective n-type semiconductor(right).	9
2.2.1	Ideal crystallite unit cells of anatase (left) and rutile (right) plotted by [41]. The blue bullets are representing Ti^{4+} atoms and the red bullets are representing O^{2-} atoms. The green vector represents the top-to-top axis of the basic TiO_6 -octaheron. The figure is modified from [42].	12
2.3.1	schematic draw of the charge carrier formation and charge carrier diffusion inside the semiconductor during the photocatalytic process modified from [19], the green paths leads to electron-hole-recombination and avoids any photocatalytic process.	14
3.1.1	Photography of the own build furnace for in-situ XRD experiments at the P07 beamline at the HASYLAB of the DESY,Hamburg.	19
3.1.2	Photography of the heating coil and the sample holder of the own build furnace for in-situ XRD experiments after the alignment and before the measurement of a Degussa P25 pellet with an applied external electrical field.	20
3.1.3	Examples of isotherms of a mesoporous catalysts material with open pores(left) and closed pores(right) from [89].	22
3.1.4	Example of binding energies depending on the Fermi-energy(left) of Uranium and scheme of photoelectron emission process(right) from [91].	24
3.1.5	XPS-setup at the IFW Dresden, including a preparation chamber with an external heating system for quasi-in-situ measurements.	26

3.1.6 Schematic draw of the circuit diagram for the resistivity measurement setup, with reference resistance R_r , sample resistance R_s [29].	28
3.1.7 Schematic sketch of the photocatalytic reactor cell used in this work [97].	30
3.2.1 Flow chart of the sol-gel-synthesis of amorphous titanium dioxide powder.	33
3.2.2 Schematic draw (left) and photography (right) of the used CC-CVD setup.	35
4.1.1 Overall photocatalytic kinetic constant of Degussa P25 powder series annealed in vacuum and air (bottom) and photocatalytic kinetic constant of the anatase phase of Degussa P25 powder series annealed in vacuum and air (top), modified from [51].	38
4.2.1 Examples of typically nitrogen adsorption isotherms of Degussa P25 powder samples annealed in different atmospheres (bottom) and examples of typically nitrogen adsorption isotherms of Degussa P25 pellet samples treated in vacuum with and without an applied electrical field (top), modified from [42].	40
4.2.2 Specific surface area of Degussa P25 powders and pellets treated at various temperatures and various atmospheres, modified from [42, 51]. The errors are numerical errors from BET- and BJH-calculations and are in the range of the size of the symbols.	42
4.2.3 Pore size distribution of selected Degussa P25 powders treated in vacuum and air and Degussa P25 pellets treated in vacuum with an electrical field applied (bottom). Pore size distribution of sol-gel based pellets treated in vacuum with and without an electrical field applied (top), modified from [42, 51].	44
4.3.1 Survey measurements of Degussa P25 pellets and anatase thin films with and without an applied electrical field during heat treatment in vacuum.	46
4.3.2 Calculated results from the XPS-analysis of Degussa P25 pellets quasi-in-situ treated in ultra-high vacuum ($p \approx 1 \cdot 10^{-9} \text{ mbar}$) for 2 h, presenting the Ti^{3+} percentage and the $O_{\text{structural}}/\text{Ti}$ relation, modified from [29].	49
4.3.3 XPS detailed spectra of Ti 2p-peaks (left) of a Degussa P25 pellet during quasi-in-situ heat treatment for two different temperatures and the difference of these Ti 2p-spectras (right). The spectra are normalised in intensity and shifted in the binding energy achieve the difference plot [29].	49
4.4.1 SEM image of the analysed area(left) and EDX spectrum(right) of the black titanium dioxide pellet.	51
4.5.1 Measurement of the resistivity over temperature of Degussa P25 titanium dioxide pellet samples in vacuum and in air. The reference resistance is $R_R = 1 \text{ M}\Omega$. Modified from [29, 42].	52

4.5.2 Measurement of the resistivity over temperature of sol-gel-based-sample in high vacuum. The reference resistance is $R_R = 1 M\Omega$	55
4.5.3 Measurement of the resistivity over temperature of thin film anatase samples in vacuum and air. The reference resistance is $R_R = 1 M\Omega$. Between the first run and the second run of the second sample an I-V-characteristic was performed. The reference resistance is $R_R = 1 k\Omega$ during the 2nd run of the second sample. Modified from [42].	56
4.5.4 Measurement of the resistivity over temperature of a Degussa P25 titanium dioxide pellet in vacuum including linear fits to calculate the barrier energy of the charge carrier traps during the resistive switching process. The reference resistance is $R_R = 1 M\Omega$	58
4.6.1 Photography of the mauled black titania pellet treated at 450°C before(left) and after(right) healing process. This healing process includes a heat treatment in air at 400°C for 2 h.	60
4.6.2 EPR-spectrum of selected Degussa P25 powder or pellet samples measured at 100 K [29].	61
4.6.3 EPR-spectrum of selected Degussa P25 powder or black pellet samples measured at 100 K, the Degussa P25 powder heat treated at 400°C in vacuum is chosen as a reference powder.	62
4.7.1 Sketch of the measured Degussa P25 pellet, with a measurement spot(red)or channel, respectively, outside of the silver electrode and an external electrical field normal to the surface (green).	64
4.7.2 Sketch of the measured Degussa P25 pellet, with a measurement spot(red)or channel, respectively, on the edge of the silver electrode and an external electrical field tangential to the surface (green).	64
4.7.3 Intensity mapping of in-situ X-ray diffraction measurements in vacuum ($p \approx 1 \cdot 10^{-4} mbar$) with different external electrical field orientation and different measurement positions on Degussa P25 pellets. The intensity is standardised to the intensity of the anatase (101)-reflex of each measurement and is plotted in logarithmic scale in the range of $[0.02 \cdot I_{A(101)} : 6.00 \cdot I_{A(101)}]$, modified from [42].	65
4.7.4 Experimental data of the integrated XRD-pattern of a Degussa P25 pellet measured in-situ in vacuum ($p \approx 10^{-4} mbar$) with an external electrical field normal to the surface at 500°C [42]. The peak positions of every possible phase included are given according to [57, 58, 130–134].	66

- 4.7.5 2D map-plot of Degussa P25 pellet samples measured at 500 °C during the heating process in vacuum. The external electrical field is applied normal to the surface and the measurement spot is outside of the electrode(left) or the external electrical field is applied tangential to the surface and the measurement spot is on the edge of the electrode(right). The intensity is in square-root scale [42]. 67
- 4.7.6 Orientation dependency of the X-ray diffraction in-situ measurements in vacuum ($p \approx 10^{-4} \text{ mbar}$) for Degussa P25 pellets at selected temperatures. **Left:** external electrical field normal to the surface and the measurement spot in 1.5 mm distance to the electrode integrated in $\chi = 20^\circ$ (top), $\chi = 110^\circ$ (bottom). **Right:** external electrical field tangential to the surface and the measurement spot on the edge of the electrode integrated in $\chi = 20^\circ$ (top), $\chi = 110^\circ$ (bottom) [42]. 68
- 4.7.7 Graphical representation of the unit cell of the arminiase phase with the lattice plane (411) which defines the characteristic titanium-oxygen-bond (left) and of the crystal shape of the arminiase phase represented by the characteristic lattice planes defined by the reflections which could not be dedicated to real titanium dioxide phases (right) [42]. Plotted by [41]. 70
- 4.7.8 Experimental data(points) and theoretical calculated curve(line) of the integrated XRD-pattern of a Degussa P25 pellet measured in-situ in vacuum ($p \approx 1 \cdot 10^{-4} \text{ mbar}$) with an external electrical field normal to the surface at 500 °C. The refinement includes the arminiase-phase [42]. 71
- 4.7.9 2D experimental data(bottom) and 2D theoretical calculated data (top) of the integrated XRD-spectra of a Degussa P25 pellet measured in-situ in vacuum ($p \approx 1 \cdot 10^{-4} \text{ mbar}$) with an external electrical field normal to the surface at 500 °C. Refinement includes the arminiase-phase. The intensity is in square-root scale. Modified from [42]. 72
- 5.1.1 photocatalytic kinetic constant normed on the specific surface area of the sample, from [51]. 76
- 5.2.1 Resistivity of Degussa P25 pellets and anatase thin films in vacuum($p \approx 1 \cdot 10^{-5} \text{ mbar}$). 78
- 5.2.2 I-V-characteristics of the anatase thin film at anomaly temperatures in vacuum ($p \approx 1 \cdot 10^{-5} \text{ mbar}$) and a reference resistance of 1 k Ω . The red dots marking the limits of applied source voltage $U_{source} = \pm 100 \text{ V}, 0 \text{ V}$. The black arrows marks the direction of the hysteresis, which is from insulating state to conducting state in every measurement. 79

- 5.2.3 Photography of a titanium dioxide thin film sample after the resistivity measurement in vacuum from the front (left) and the rear (right). The electrical field was applied tangential to the surface between two electrodes. The third electrode is a blind electrode which was not connected. 81
- 5.3.1 2D-detector image of titanium dioxide thin film samples prepared by CVD method. The thin films are treated in vacuum ($p \approx 1 \cdot 10^{-6} \text{ mbar}$) up to 550°C . The conductive sample (left) and its insulating satellite sample, (right). 82
- 5.3.2 Integration over the χ -angle of the 2D-images conductive titanium dioxide thin film (left) with the focus on anatase-(004)-reflex and the reflex of the new phase. Integration over the χ -angle of the 2D-images of the insulating titanium dioxide thin film (right) with focus on the A(101)-reflex and the A(004)-reflex. 83
- 5.3.3 2D-detector image (left) of black Degussa P25 pellet and the map plot as Integration over the χ -angle (right) of the 2D-images of the black Degussa P25 pellet with the focus on anatase-(004)-reflex and the rutile-(210)-reflex (left). The position of rutile-(210)-reflex is similar to the position of the reflex of the new phase in the conductive anatase thin film. 83
- 5.3.4 Difference plot between XRD 2D-detector image of a Degussa P25 pellet with an external electrical field applied normal to the surface(E_n) and a Degussa P25 pellet without an external electrical field (E_0) measured in vacuum $p \approx 1 \cdot 10^{-4} \text{ mbar}$ at 220°C during heating. The intensity is in logarithmic scale. The limits of the intensity of the difference I_{diff} in dependency of the maximum intensity of the original measurement I_{max} is: $0.002 \cdot I_{max} < I_{diff} < 0.2 \cdot I_{max}$, modified from [42]. 85
- 5.3.5 Difference plot between XRD 2D-detector image of a Degussa P25 pellet with an external electrical field applied normal to the surface(E_n) and a Degussa P25 pellet without an external electrical field (E_0) measured in vacuum $p \approx 1 \cdot 10^{-4} \text{ mbar}$ at 400°C during heating. The intensity is in logarithmic scale. The limits of the intensity of the difference I_{diff} in dependency of the maximum intensity of the original measurement I_{max} is: $0.02 \cdot I_{max} < I_{diff} < 0.2 \cdot I_{max}$, modified from [42]. 86
- 5.3.6 Difference plot between XRD 2D-detector image of a Degussa P25 pellet with an external electrical field applied normal to the surface(E_n) and a Degussa P25 pellet without an external electrical field (E_0) measured in vacuum $p \approx 1 \cdot 10^{-4} \text{ mbar}$ at 450°C during cooling. The intensity is in logarithmic scale. The limits of the intensity of the difference I_{diff} in dependency of the maximum intensity of the original measurement I_{max} is: $0.02 \cdot I_{max} < I_{diff} < 0.2 \cdot I_{max}$, modified from [42]. 87

- 5.3.7 Difference plot between XRD 2D-detector image of a Degussa P25 pellet with an external electrical field applied normal to the surface(E_n) and a Degussa P25 pellet without an external electrical field (E_0) measured in vacuum $p \approx 1 \cdot 10^{-4} \text{ mbar}$ at 200°C during cooling. The intensity is in logarithmic scale. The limits of the intensity of the difference I_{diff} in dependency of the maximum intensity of the original measurement I_{max} is: $0.02 \cdot I_{max} < I_{diff} < 0.2 \cdot I_{max}$, modified from [42]. 88
- 5.3.8 Difference plot between XRD 2D-detector image of a Degussa P25 pellet with an external electrical field applied normal to the surface(E_n) at 400°C and at 300°C during heating. The intensity is in logarithmic scale. The limits of the intensity of the difference I_{diff} in dependency of the maximum intensity of the original measurement I_{max} is: $0.02 \cdot I_{max} < I_{diff} < 0.2 \cdot I_{max}$, modified from [42]. 89
- 5.4.1 EPR spectra of Degussa P25 powder and black titania powders before and after calcination in air at room temperature with focus on the hole trapping sites close to interfaces. 91
- 5.4.2 I-V-characteristics of activated Degussa P25 pellets in vacuum($p \approx 1 \cdot 10^{-5} \text{ mbar}$) and a reference resistance of $1 \text{ k}\Omega$ for different maximum external applied voltage. The symbols marking 10 V steps of applied source voltage. The black arrows marks the direction of the hysteresis, which is from insulating state to conducting state in each measurement [42]. 92
- A.1 Resistivity of the measured Degussa P25 pellets during in-situ XRD measurement at the P07 beamline. The reference resistance is $R_R = 1 \text{ M}\Omega$ and the applied voltage is $U_{source} \approx 10 \text{ V}$ 97
- B.1 Arminiase unit cells with lattice occupancies of the titanium atoms lattice spots of 100% . The occupied lattice spots depend on the orientation of the electrical field. It is assumed, that the electrical field orientation on the left side is in the opposite direction compared to the right side. 99
- B.2 Rietveld refinement of the black Degussa P25 pellet sample. The experimental data is represented as points and the theoretical calculated curve is represented as red line. It is assumed that defective anatase and defective rutile is included. These two defective phases are representing the density distribution changes inside the original phases and are the basis of the arminiase phase crystallisation. 100

C.1 Complete EPR-measurements of the the field assisted prepared samples and the powder annealed at 400 °C in vacuum. **Left:** Measured at 100 K. **Right:** Measured at room temperature. 101

List of Tables

2.1.1 Lattice oxygen vacancies formation energies calculated by DFT-method from [44].	8
4.2.1 Calculated results of specific surface area and pore volume analysis of different titanium dioxide systems. The errors are numerical errors from BET- and BJH-calculations [42, 51].	45
4.3.1 Results of the XPS analysis for selected powders and for quasi-in-situ experiments of different titanium dioxide systems, based on Degussa P25 or anatase thin film (A-tf). The samples are either treated in air, in high vacuum (HV, $p \approx 1 \cdot 10^{-5} \text{ mbar}$) or in ultra high vacuum (UHV, $p \approx 1 \cdot 10^{-9} \text{ mbar}$).	50
4.4.1 Results from the EDX measurements of the black titanium dioxide pellet calcinated in vacuum with an applied external field normal to the surface at 450°C . The errors are absolute errors.	51
4.5.1 Calculated energy barrier of charge carrier traps for various titanium dioxide systems under different measurement conditions. The energy barrier calculation is based on the slope of the in-situ resistivity measurements [29, 42].	59
4.7.1 XRD results of selected titanium dioxide samples from XRD measurements calculated by Rietveld refinement [42, 51].	73

Acknowledgement

Normally, this section is used to name the people that made this thesis possible starting with my supervisors and my colleagues and ending with the workers from the mechanical work shop. And this is absolutely right.

Since, this work was born somewhere between Rostock, Bischofswerda, Faro, Dresden and Hamburg it has to be a huge list of people which should be acknowledged. Therefore, I choose a slightly different way.

This written thesis is only a minor part of my work on transition-metal-oxides which was a centre of my daily life the last couple of years and includes a lot of learning, working, teaching and growing as a professional and a private person. I want to say thank you to each one who was somehow part of it:

I acknowledge my three families. The one where I was born into, because they were, they are and they ever will be my home.

The one which I chose to be part of because they support me in the darkest and in the brightest hour, independently, whether they stay near to me or stay 100, 400 or even 10000 kilometres away. I can always count on them even when I feel pride, shame or sad and even if we argue about god, the world and science at 3 am in the morning.

And the one which share week by week and year by year the fields of honour with me while dreaming from this one journey through Europe.

I want to mention also the other side. All these people whose meeting with me ended in mutual disappointment, frustration and pain because they significantly influenced this thesis.

I acknowledge my professional environment. My supervisors and colleagues were a huge help during the last years and they didn't had the choice to not bearing my positive and negative peculiarities.

And I mention each person who shared time with me weeks, days or only a couple of hours. You gave me the possibility to see a world outside of the university and gave me the chance to step back and get a better view on my work despite I mostly don't know your name.

Finally, I acknowledge each one who were part of my way but will never see its ending because we lost.

Although, this written thesis is only a small sample size each one who is mentioned had left some traces in it and I say thank you; because the completion of this thesis marks an end of the chapter which started back in summer 2002 when I left my home.

TU NE QUAESIERIS, SCIRE NEFAS, QUEM MIHI, QUEM TIBI FINEM DI
DEDERINT, LEUCONOE, NEC BABYLONIOS TEMPTARIS NUMEROS. UT
MELIUS, QUIDQUID ERIT, PATI. SEU PLURIS HIEMES SEU TRIBUIT
IUPPITER ULTIMAM, QUAE NUNC OPPOSITIS DEBILITAT PUMICIBUS
MARE TYRRHENUM: SAPIAS, VINA LIQUES, ET SPATIO BREVI SPEM
LONGAM RESECES. DUM LOQUIMUR, FUGERIT INVIDA AETAS: CARPE
DIEM QUAM MINIMUM CREDULA POSTERO.

HORAZ, CARMEN I,XI

CURRICULUM VITAE

Personal information

Name: Martin Hantusch

Born: 14th April 1990, Grossroehrsdorf, Germany

Education

2013–present PhD Student Rostock University Rostock, Germany Thesis title: "Temperature anomalies in transition-metal-oxides and their correlations with photocatalytic activity"

2011–2013 Master of Science/Diplom Rostock University Rostock, Germany Major: Physics, Specialised in Nanotechnology and New Materials Thesis title: Chemical synthesis and thermal analysis of Titanium dioxide, grade: very good

2008–2011 Bachelor of Science Rostock University Rostock, Germany Major: Physics

2002–2008 High-school/Gymnasium Saechsisches Landesgymnasium St.Afra Meissen, Germany

Vocational Experience

2013–2016 Researcher WORK GROUP "NEW MATERIALS" Rostock University, Germany Design and characterisation of advanced multifunctional nanostructured materials, specialised on transition-metal-oxide nanoparticles and thin film coatings for water treatment applications

Miscellaneous

2015–2016 Associated PhD Student WELISA Rostock University, Germany Design and analysis of bioactive implant material.

2014–2016 Guest researcher WORK GROUP "MATERIAL SCIENCE" Algarve University, Faro, Portugal Project tasks: "Relation between electronic structure of metal oxides and their photocatalytic properties", specialised on thin film preparation by chemical vapour deposition, several weeks per semester over three years.

2008 INTERNSHIP SCIENCE CENTER ROSSENDORF Dresden, Germany

2007 INTERNSHIP QIMONDA AG Dresden, Germany

2006 Voluntary activity LIFE GUARD DLRG Zingst, Germany

List of Publications

- 2015 - "An improvement of photocatalytic activity of TiO₂ Degussa P25 powder"; Bessergenev, Mateus, Botelho Do Rego, Hantusch, Burkel; Applied Catalysis A: General, vol. 500 (2015)
- 2017 - "Photocatalytic reactor, CVD technology of its preparation and water purification from pharmaceutical drugs and agricultural pesticides"; Bessergenev, Mateus, Morgado, Hantusch, Burkel; Chemical Engineering Journal, vol. 312 (2017)
- 2017 - "Electronic properties of photocatalytic improved Degussa P25 titanium dioxide powder"; Hantusch, Bessergenev, Mateus, Knupfer, Burkel; Catalysis Today (2017)
- 2018 - "Structural, Electric and Photocatalytic Properties of TiO₂ Nanoparticles Doped by Co"; Bessergenev, Mariano, Mateus, Lurenco, Hantusch, Burkel, Botelho Do Rego, Kopcansky, Timko; Materials Research Bulletin; *to be submitted*
- 2018 - "Structural and Magnetic of TiO₂ Nanoparticles Doped by Co"; Mariano, Bessergenev, Mateus, Lurenco, Hantusch, Burkel, Botelho Do Rego, Kopcansky, Timko; Journal of Magnetism and Magnetic Materials; *to be submitted*
- 2018 - "Resistive switching and electrical field induced crystal structure changes in titanium dioxides observed in-situ by synchrotron radiation"; Hantusch, Bessergenev, Schell, Knupfer, Burkel; *in preparation*
- 2018 - "Pseudo piezoelectricity of calcium titanate for bone implant prepared by sol-gel synthesis and field assisted sintering technique"; Riaz, Hantusch; witte, Bodnar, Springer, Burkel; *in preparation*

Conferences

- 2017 - "Electronic properties of photocatalytic improved Degussa P25 titanium dioxide powder"; Oral presentation; 9th International Conference on Environmental Catalysis; Newcastle, Australia

Patents

- 2016 - "Photocatalytic reactor for water treatment and CVD technology of its preparation"; Bessergenev, Mateus, Burkel, Hantusch; Pedido Provisorio de Patente - INPI; Lissabon

Declaration of Authorship

I hereby certify that this thesis has been composed by me and is based on my own work, unless stated otherwise. No other person's work has been used without due acknowledgement in this thesis. All references and verbatim extracts have been quoted, and all sources of information, including graphs and data sets, have been specifically acknowledged.

Rostock, December 15, 2017